Plasma Diagnostics
Applying K-Line Emission Profiles
of Si and Ar

Dissertation
to obtain the academic degree
doctor rerum naturalium (Dr. rer. nat.)
at Faculty of Mathematics and Natural Sciences
University of Rostock

presented by
Yi-Ling Chen, born 11th Sept. 1984 in Taiwan
from Rostock

Rostock, 25 June 2014

Die Gutachten:
1. Gutachterin:
PD Dr. Heidi Reinholz,
Institut für Physik, Universität Rostock
2. Gutachter:
Prof. Dr. Manfred Schlanges,
Institut für Physik, Universität Greifswald

Datum der Einreichung: Rostock, 25 Juni 2014
Datum der Verteidigung: Rostock, 12 November 2014

Contents

Contents

1. Motivation

1.1. K_α Plasma Diagnostics

In 1895, Wilhelm Conrad Röntgen was first discovering the X-rays in the Institute of Physics of the University of Würzburg [1]. In 1915 Nobel Prize winners were William Lawrence Bragg and William Henry Bragg. They were working on crystal structures using X-rays [2]. X-ray is an electromagnetic radiation and most of X-rays have a wavelength in the range between 1 pm to 10 nm. K_α emitting energy in the X-rays energy of photons range is between 100 eV to 1 MeV corresponding to the wavelength range between 1 pm to 10 nm. Modifications of emission K-line profiles due to a warm dense plasma environment is a good tool for plasma diagnostics. The free electron density of warm dense matter is located from 10^{20} cm^{-3} to 10^{24} cm^{-3} in the plasma diagnostic process. Roughly plasmas are divided into low density plasma and high density plasma. The low density plasma has density up to 10^{17} ions/cm^3 and the high density plasma has a density above from 10^{19} ions/cm^3 [3]. For example: Tokamaks [4] and magnetic confinement devices (i.e. International Thermonuclear Experimental Reactor (ITER [5])) are low density plasmas. Plasma in Tokamak is confined to a toroidal device in the magnetic field [4]. Recently years the fusion reaction researchers are focusing on the nucleus of deuterium and tritium (D-T) fusion reaction in some plasma fusion research [4, 5]. The higher density plasmas have the direct effect of the plasma environment on the ions. Two examples are : spectral function of quasiparticle line shifts [6] and K-line emission spectrum line profiles [7]. The hot plasmas in the microscopic atomic region should consider more detail of the influence of the plasma environment for the ionic potential, electron-electron interaction, electron-ion interaction and emission spectra of the plasma [3]. X-rays spectra is used for diagnostics of plasmas at silicon solid state density and we use the same method calculation argon solid state density in the present works. Plasma parameters strongly affect the structure of the emitted K_α emission lines shown in Ti K_α line [8]. Through the two different excitation of emitters (a) high energy of intense laser [9, 10, 11, 12, 13] or (b) heavy ion beam [14, 15, 16] can be excited an electron from ground state E_0 to excited state E_i with one hole in the 1s shell (K_α initial state). Then one photon emission from initial state E_i to final state E_f with one hole in the 2p shell (K_α final state) including different emitter configurations are considered in the K_α emission spectral line, see Fig. 1.1. We focus on K_α warm dense matter Si and Ar irradiated emission spectral line. K_α photons are calculated from inner shell ionization and excitation (4s, 3d, 3p, 3s) emission fluorescence. K_α emission on high Z solids irradiated by intense laser pulses. The emission of photons from Bremsstrahlung is calculated by acceleration of the hot electron with elastic collision or inelastic collision
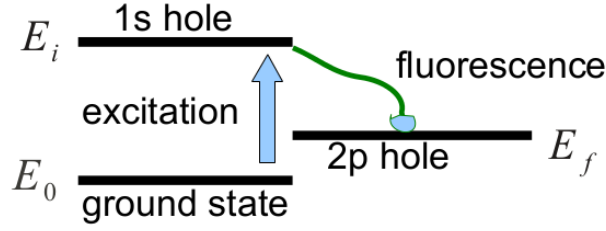
Figure 1.1.: K_α fluorescence spectra emission process. Si the configuration of the ground state is given by : $1s^2 2s^2 2p^6 3s^2 3p^2$. Emission of Si^+ configuration of initial state is given by: $1s^1 2s^2 2p^6 3s^2 3p^2$ and configuration of final state is given by: $1s^2 2s^2 2p^5 3s^2 3p^2$.

processes [17].

In section 1.2 we will introduce some plasma parameters for describing the many-particle systems depending on the temperature and free electron density in the plasma diagnostics environment. In section 1.3 we will calculate the hydrogen plasma describing the degree of ionization of plasma and we will look for the Mott effect in pressure ionization. In section 1.4 we will describe the experiments of high energy laser Si K_α experiment in subsection 1.4.1 . Ca^{6+} ion beam is penetrated into SiO_2 aerogel. The K_α fluorescence spectra are investigated in subsection 1.4.2. And in subsection 1.4.3 we will describe the Argon high energy X-rays in the Ar droplets K_α experiment spectra.

1.2. Plasma Parameters and Plasma Effect

Plasma is one of the four fundamental states of matter (solid , liquid, gas and plasma) and the most of plasmas are in the Universe. Solid particles are close together. Solid particles can not move freely. Liquid particles are incompressible fluid conforming to a constant volume. Gas particles are compressible fluid. Gas particles can move freely. Plasma particles include electrons, ions and atoms. Plasma has a high enough temperature that the greater part of atoms is ionized. For plasma diagnostics, the range of temperature is mostly between 10 eV to several hundred eV. A plasma consists of ions at atomic number Z, density of bounds electrons n_b bonding in the core and density of free electrons n_e moving freely in the plasma. The solid atom density of isolated silicon is $5.0 \cdot 10^{22}$ cm^{-3} and the solid atom density of isolated argon is $2.63 \cdot 10^{22}$ cm^{-3}. Through the parameter of the degree of ionization α can be described some characters of plasma more detailed. The ionization of charge states is described the number of electrons missing from each atom. The average degree of ionization of a plasma is defined by [18]

$$\alpha = \frac{n_e}{n_e^{total}}.$$
(1.1)
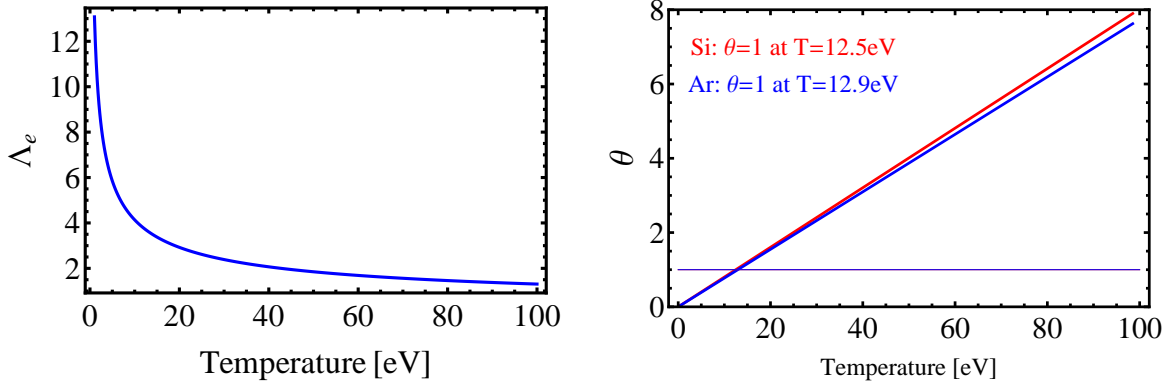
(a) The electron thermal wavelength $\Lambda_e \sim T^{-1/2}$. At low temperature has a large electron thermal wavelength than high temperature.

(b) Si and Ar degenerate parameter. Si degenerate parameter $=1$ at $T = 12.5$ eV and Ar degenerate parameter at $T = 12.9$ eV. Si solid electron density is given by $n_e = 2.0 \cdot 10^{23}$ cm^{-3}. Ar solid electron density is given by $n_e = 2.1 \cdot 10^{23}$ cm^{-3}.

Figure 1.2.: Electron thermal wavelength depends on temperature. Non-degenerate plasma is in $\theta > 1$ at higher temperature and degeneracy plasma is $\theta < 1$ at lower temperature.

On the right side of Eq. (1.1) denominator n_e^{total} is the density of total electrons and numerator n_e is the density of free electrons. The electron of bonding electrons n_b on nuclear is equal to the total electron density n_e^{total} minus the density of free electrons n_e in the neutrality plasma system.

The other important plasma parameter is electron thermal wavelength Λ_e. The spatial extension of the probability depends on the electron thermal wavelength Λ_e. Electron thermal wavelength is defined by

$$\Lambda_e = \left(\frac{2\pi\hbar^2}{m_e k_B T} \right)^{1/2}. \tag{1.2}$$

In dense plasmas, the electron thermal wavelength Λ_e has the same order as the mean distance of electrons d_e. And d_e is proportional to density of free electrons $d_e \sim \frac{1}{(n_e)^{1/3}}$. There are non-degenerate plasmas and degenerate plasmas in quantum statistics. In case $n_e \Lambda_e^3 \ll 1$, we have non-degenerate plasmas. In case $n_e \Lambda_e^3 \gg 1$, it is a strongly degenerate plasma [18]. In Fig. 1.2a is shown the wavelength of free electrons is quickly decaying with increasing temperature from $T = 0$ eV to $T = 15$ eV satisfied the degenerate plasmas. When the temperature is higher than 15 eV the wavelength of free electrons tends to smoothly decay and there are more free electrons satisfied the non-degenerate plasmas, see Fig. 1.2a.

In strongly degenerate Fermi system at zero temperature the chemical potential equal to Fermi energy is defined by

$$\mu_e^0 = \frac{\hbar^2}{2m_e} \left(3\pi^2 n_e \right)^{2/3} = E_{\text{Fermi}}. \tag{1.3}$$
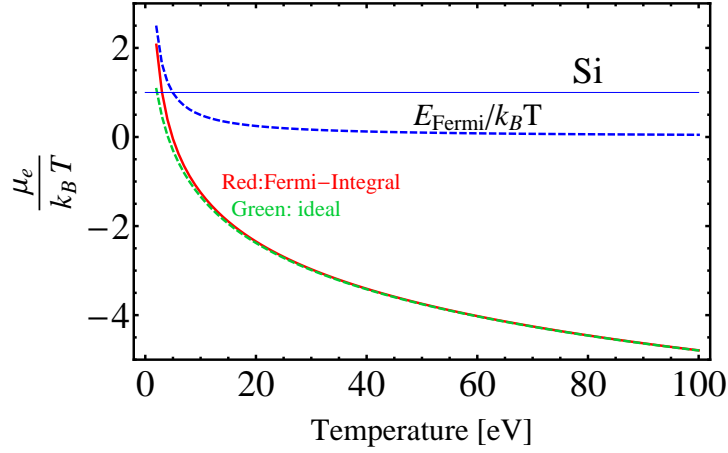
Figure 1.3.: Si comparison the chemical potential of free electrons in degenerate ideal Fermi gas (Red line) and non-degenerate ideal gas (Green line). The solid blue line shows the thermal energy equals the Fermi energy at the degenerate parameter of plasma equal to 1. The temperature higher than 20 eV have the same behavior between Fermi Integral and ideal gas.

In Eq. (1.3) has electron mass m_e with free electron density n_e.

The degenerate parameter of plasma θ is defined by

$$\theta = \frac{k_B T}{E_{\text{Fermi}}}. \tag{1.4}$$

In Eq. (1.4) the thermal energy is $k_B T$ and the Fermi energy is $\Lambda_e \left(3\pi^2 n_e\right)^{2/3}$. If $\theta < 1$ should use the Fermi distribution and if $\theta > 1$ one can use the Boltzmann distribution. In Fig. 1.2b shows the degenerate parameter θ in Si when temperature is higher than 12.5 eV and for Ar when temperature is higher than 12.9 eV one can use the Boltzmann distribution. When Si temperature lower than 12.5 eV and for Ar when temperature lower than 12.9 eV one can use the Fermi distribution.

Now let us consider a dimensionless chemical potential $\frac{\mu}{k_B T}$ to compare with degenerate Fermi system and non-degenerate ideal system. In Fig. 1.3 is shown the dimensionless chemical potential with different temperature on the degenerate Fermi system and non-degenerate ideal system. The temperature under 10 eV should be considered degenerate plasma and over the 20 eV both have the same behavior in dimensionless chemical potential, see Fig. 1.3.

The electron coupling parameter of plasma Γ_e is defined by

$$\Gamma_e = \frac{e^2}{4\pi\epsilon_0 r_e k_B T}. \tag{1.5}$$

In Eq. (1.5) r_e is the Wigner-Seitz radius and $\frac{e^2}{4\pi\epsilon_0 r_e}$ is Coulomb potential. The weakly coupled plasma is located at $\Gamma_e \leq 0.1$ and strongly coupled plasma is located at $\Gamma_e \gg 0.1$.

The plasma frequency of electrons ω_{pl} is defined by

$$\omega_{pl} = \sqrt{\frac{n_e e^2}{\epsilon_0 m_e}}. \tag{1.6}$$

In Eq. (1.6) ϵ_0 is vacuum permittivity, n_e is free electron density, m_e is the mass of the electron.

The ϵ^{RPA} is the dielectric function of random phase approximation [6] in plasma. The statically screened Coulomb potential is given by

$$V_{ab}^S(\mathbf{q}) = \frac{V_{ab}(\mathbf{q})}{\epsilon(\mathbf{q}, 0)}. \tag{1.7}$$

In Eq. (1.7) $V_{ab}(\mathbf{q})$ is the Coulomb potential and $\epsilon(\mathbf{q}, 0)$ is the static dielectric function defined by

$$\epsilon(\mathbf{q}, 0) = 1 + \frac{\hbar^2 \kappa^2}{\mathbf{q}^2}. \tag{1.8}$$

Reflectivity R_ω with the dielectric function of ϵ is given by

$$R_\omega = \left| \frac{\sqrt{\epsilon} - 1}{\sqrt{\epsilon} + 1} \right|^2. \tag{1.9}$$

In the case of the plasma frequency smaller than the X-rays frequency $\omega_{pl} < \omega$ and the reflectivity $R_\omega < 1$ one has radiation propagation. In the case of the plasma frequency bigger than the X-rays frequency $\omega_{pl} > \omega$ and the reflectivity $R_\omega = 1$ has no radiation propagation. The power absorptivity [19] is given by

$$A_\omega = 1 - R_\omega - T_\omega. \tag{1.10}$$

In Eq. (1.10) shown A_ω is power absorptivity, R_ω is power reflectivity and T_ω is power transmissivity, respectively. When $R_\omega \approx 1$ is corresponding to the $T_\omega \approx 0$ and $A_\omega \approx 0$. The free electron density and temperature are two important factors in the plasma diagnostics. The Si plasma and Ar plasma were located on the range of free electron density n_e from 10^{22} cm^{-3} to 10^{24} cm^{-3}. We consider the temperature k_BT from 10 eV to 160 eV in the plasma. The plasma is generated in a high temperature of X-rays (100 eV - 1 MeV). So the most of the atoms are ionized and all molecular bonds are broken.
The classical plasma effect of long wavelength radiation [6] reduces to

$$\lim_{k \to 0} \epsilon^{RPA} = 1 - \frac{\omega_{pl}^2}{\omega^2}. \tag{1.11}$$

1.3. Hydrogen Plasma

An ideal neutral hydrogen Plasma is considered in thermodynamic equilibrium. The hydrogen plasma is partially ionized describing by the degree of ionization α in Eq. (1.1).

1. Motivation

In non-degenerate case, for the chemical potential of atoms μ_j in state $|j\rangle$, ($j = n, l, m$; principal quantum number n and the angular momentum quantum number l) is equal to the chemical potential of free electrons μ_e addition to the chemical potential of the protons μ_p. Then the chemical potential of atoms μ_j is given by

$$\mu_j = \mu_e + \mu_p. \tag{1.12}$$

In non-degenerate case, for the chemical potential of atoms μ_j depends on the density n_j. Bound state energies $E_j(n_e, T)$ is defined by

$$E_j(n_e, T) = E_j^0 + \Delta_j(n_e, T). \tag{1.13}$$

In Eq. (1.13) $\Delta_j(n_e, T)$ is the self-energy shift. The thermal wavelength of the atoms Λ_H is given by

$$\Lambda_H = \left(\frac{2\pi\hbar^2}{Mk_BT} \right)^{1/2}. \tag{1.14}$$

In Eq. (1.14),the mass of atoms is M, reduced Planck constant is $\hbar$ and the Boltzmann constant is k_B. The expression of the chemical potential of atoms μ_j in state $|j\rangle$ is given by

$$\mu_j = k_BT \ln \left(\frac{n_j \Lambda_H^3 e^{\beta E_j}}{(2s_e + 1)(2s_{p+1})} \right). \tag{1.15}$$

The chemical potential of the free electrons is given by

$$\mu_e = k_BT \ln \left(\frac{n_e \Lambda_e^3}{2s_e + 1} \right) + \Delta_e. \tag{1.16}$$

In Eq. (1.16) $\Delta_e = \mu_e^{int} = \frac{\kappa e^2}{2}$ is described interaction chemical potential of electrons and the chemical of the free protons is given by

$$\mu_p = k_BT \ln \left(\frac{n_p \Lambda_p^3}{2s_p + 1} \right) + \Delta_p. \tag{1.17}$$

In Eq. (1.17) $\Delta_p = \mu_p^{int} = \frac{\kappa e_p^2}{2}$ is described interaction chemical potential of protons. We arrange μ_j, μ_e, μ_p to Eq. (1.12) getting

$$\frac{n_H}{n_e n_p} = \Lambda_e^3 \sigma_H(n_e, T) e^{\beta(\Delta_e + \Delta_p)} = K_H(n_e, T). \tag{1.18}$$

In Eq. (1.18) is called the Saha equation. K_H is the mass action constant and $\sigma_H(n_e, T)$ is partition function given by

$$\sigma_H(n_e, T) = \sum_j e^{-\beta E_j(n_e, T)}. \tag{1.19}$$

In case of an ideal hydrogen plasma, we consider the ground state E_1^0, and ignore other excited states. The partition function can be written

$$\sigma_H^0(n_e, T) = e^{-\beta E_1^0}. \tag{1.20}$$

When the self-energy shift is equal to 0, $\Delta_i = 0$ and there is no interaction of chemical potentials, $\Delta_e = \Delta_p = 0$. The Saha equation can be rewritten

$$\frac{n_H}{n_e^2} = \Lambda_e^3 \sigma_H(n_e, T) = K_H^{id}(n_e, T). \tag{1.21}$$

In Fig. 1.4 shows the degree of ionization α with n_e^{tot} on the different temperature (15000 K, 30000 K, 50000 K). In an ideal hydrogen plasma, the degree of ionization α is decreased to 0 at the high total electron density density n_e^{tot}.

In case of a non-ideal hydrogen plasma, we consider the ground state E_1^0 and ignore other excited states. The partition function is described by

$$\sigma_H^0(n_e, T) = e^{-\beta E_1^0 + 2\Delta_2}. \tag{1.22}$$

In Eq. (1.22) has $\Delta_e = \Delta_p$. The self-energy shift is equal to 0, $\Delta_j = 0$. The density of electrons n_e is equal to the density of protons n_p. So the Saha equation is given by

$$\frac{n_H}{n_e^2} = \Lambda_e^3 \sigma_H(n_e, T) e^{2\Delta_e \beta} = K_H(n_e, T). \tag{1.23}$$

If the degree of ionization α is transited approach to the value $\alpha = 1$. This means a fully ionized plasma at the higher total electron density n_e^{tot}, this effect called Mott effect and the transition of density called Mott density. The $K_H(n_e, T)$ can exhibited jumping at Mott densities from different total electron density n_e^{tot}. But in the real situation, there are partially ionized plasmas at high densities. So Planck and Larkin modify the Saha equation are satisfied the real situation. Now, we introduce the effective ionization energy

$$I_j^{eff}(n_e, T) = |E_j^0| - \Delta_j + \Delta_e + \Delta_p. \tag{1.24}$$

The Saha equation is simplified to [18]

$$K_H^{eff}(n_e, T) = \Lambda_e^3 \sum_j \left(e^{\beta I_j^{eff}(n_e, T)} \right). \tag{1.25}$$

In math the problem of Mott effect comes from the first two terms of a power series expansion of $e^{\beta I_j^{eff}}$, Planck and Larkin consider subtraction of the first two terms in the power series to deal with this problem. So the mass constant on Planck-Larkin is given by

$$K_H^{PL}(n_e, T) = \Lambda_e^3 \sum_j \left(e^{\beta I_j^{eff}(n_e, T)} - 1 - \beta I_j^{eff}(n_e, T) \right). \tag{1.26}$$

When total electron density n_e^{tot} higher than Mott density, we set the degree of ionization $\alpha = 1$ to modify. In Fig. 1.5 is a non-ideal hydrogen plasma considering α with n_e^{tot} at temperature 15000 K, 30000 K, 50000 K When effective ionization energy $I_{nl}^{eff} = 0$ the bound state vanishes calling Mott effect (Mott 1961). Mott density describes the pressure of ionization in a plasma. Using Planck-Larkin equation has continued at the Mott density solved the Mott effect problem at T=15000 K.

Figure 1.4.: The degree of ionization α as a function of the total electron density n_e^{tot} for different temperatures at the ground state energy in an ideal hydrogen plasma.
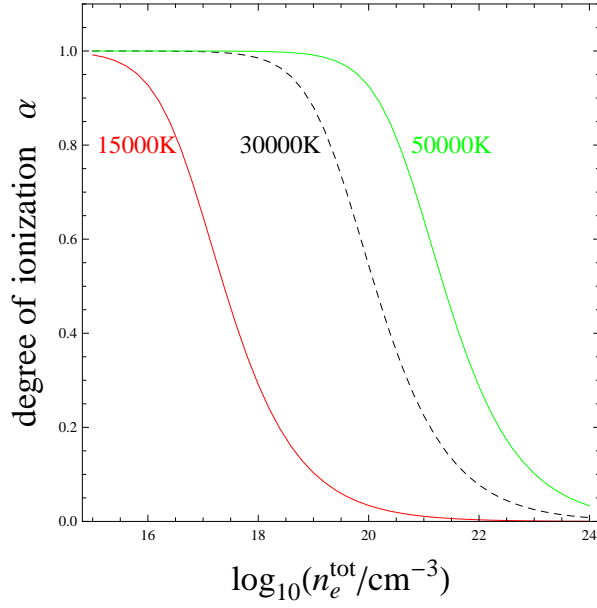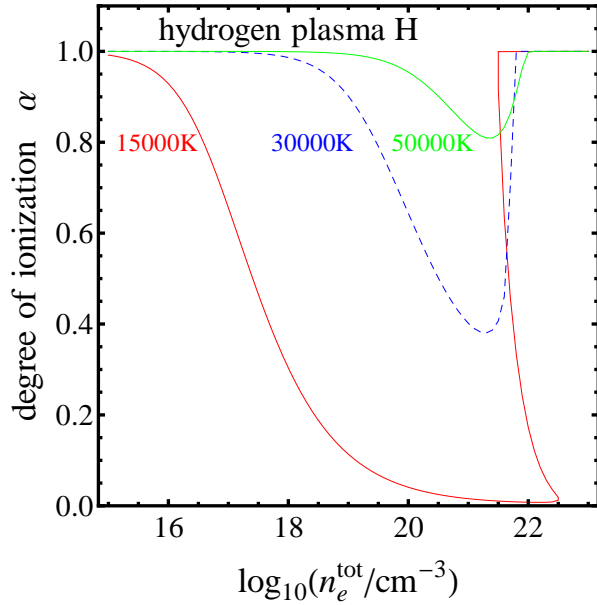

Figure 1.5.: The degree of ionization α as a function of the total electron density n_e^{tot} for different temperatures with the same interaction potential $\Delta_e = \Delta_p$ at the ground state energy from Planck-Larkin equation in a non-ideal hydrogen plasma.

1.4. Experiments

1.4.1. Si and SiO$_2$ K_α Fluorescence Spectra

In 2004, Zhenlin Liu *et al.* [13], have measured on a pure Si K_α X-rays fluorescence spectra and Si compounds K_α X-rays fluorescence spectra in the low temperature under 1 eV using a high resolution double-crystal vacuum X-rays fluorescence spectrometer in Japan. The Si K_α emission line was the resulting of electrons in the valence band shifts the inner shell electrons in higher binding energy. Before this work, Graeffe *et al.*, have also measured K_α spectra from Si and SiO$_2$ on a double-crystal spectrometer [12]. In this working recording the peak position of Si $K_{\alpha 1}$ emission energy with fine structure $P_{1/2}$ was 1739.98 eV with the peak position of Si $K_{\alpha 2}$ (also fine structure $P_{3/2}$) was 1734.98 eV, and the positive chemical shift of SiO$_2$ for the Si K_α line relative to pure Si was 0.62 eV. SiO$_2$ have some oxide compounds influenced the chemical shift in the experiment spectral line shift from pure silicon spectral line. The blue shift of X-rays fluorescence lines is interpreted by the charges of the X-rays emission atom. Our work focus on the pure silicon K_α emission fluorescence line in the plasma environment with the high temperature 30 eV. The semi- empirical NIST data were showing the distance of 0.591 eV between the fine structure of Si components [20]. In generally a plasma of medium temperature and high density (warm dense matter) is created from bulk Si and the greater part of atoms are ionized. The high energy of K_α x-rays is necessary to penetrate and investigate the Si sample. K_α shifts due to chemical binding depending on chemical surrounding, see Fig. 1.6. The chemical compounds are strongly influencing the K_α emission profile.

In chapter 3 we want to pay attention to compare this experiment Si K_α X-ray fluorescence spectra with our theoretical Si K_α X-rays fluorescence spectra shown the plasma screening reduced to negative shift (red shift).

1.4.2. Si $K_\alpha L^x M^y$ X-rays Satellites Recording SiO$_2$ Aerogel

In 2010, O. Rosmej *et al.* [15, 16], have measured the heavy ion beam Ca projectiles was penetrated into the low-density SiO$_2$ aerogel having non equilibrium distribution knockout of inner electrons. Si K_α X-rays emission spectra of the low-density SiO$_2$ aerogel induced by Ca projectiles for penetration depth x and different energies E.

The stopping medium which low density SiO$_2$ aerogel has described a level of the L-shell ionization. The experiment result has shown with different depth x and different energies E for $x_1 = 0.5$ mm ($E_1 = 11.4$ - 10.6 MeV/u) having more higher spectrum intensity than $x_2 = 5$ mm ($E_2 = 8.5$ - 7.6 MeV/u) and $x_3 = 10$ mm ($E_3 = 5.2$ - 4.0 MeV/u), see Fig. 1.7. The Ca heavy ion beam was penetrated goto deep depths x losing more energy E. The Si $K_\alpha L^x M^y$ X-rays spectra emitted satellites recording in Si target more detailed, see[15, 16]. The Lorentzian width is 0.48 eV and Gaussian width is 1 eV (instrumental profile). The Si $K_\alpha L^x M^y$ initial configuration schematic representation, see Fig. 1.8. In contrast to pure Si, the chemical environment in Si compounds affects the emitters resulting in a chemical shift for the K_α lines. The K-shell radiation of
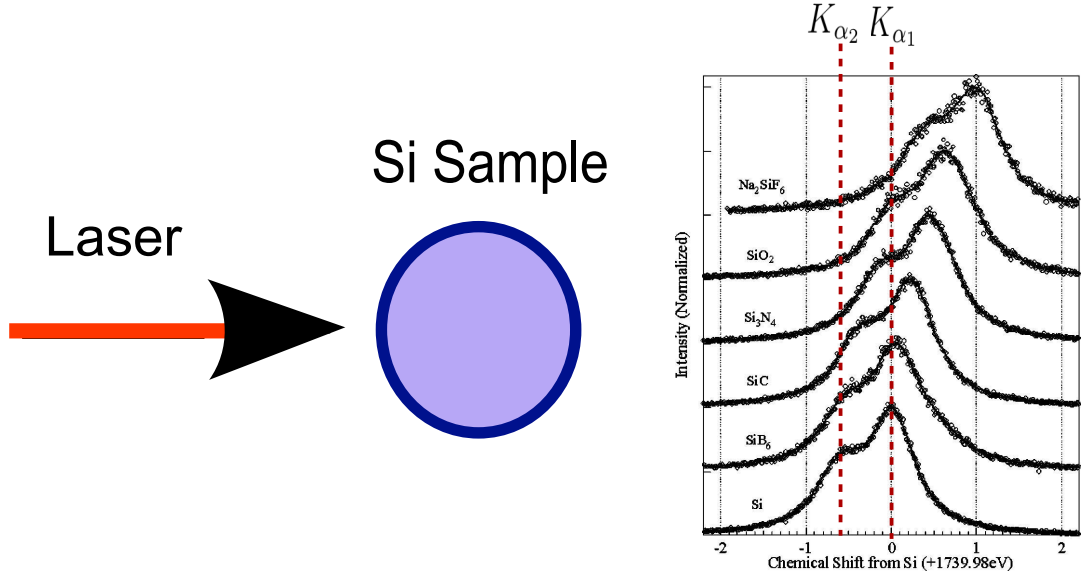
Figure 1.6.: Shifts due to chemical binding depending on chemical surrounding, measured by high-resolution Si K_α fluorescence spectra spectra of Si compounds. Si K_{α_1} is 1739.98 eV and K_{α_2} is 1734.98 eV [13].

stopping media SiO_2 is a useful plasma diagnostics. The Si inner shell vacancies of L-shell and M-shell have the ionization of the outer shell electrons accompany on the different $K_\alpha L^N M^0$ or $K_\alpha L^N M^4$ satellite lines, where N is a number of the vacancies on L shell , M^0 is ($3s^2 3p^2$ on M shell) and M^4 is full ionization on M shell. In our calculation we ignore the dynamical collision processes between heavy ions and atoms but focus on the $K_\alpha L^N$ satellite lines. All the different $K_\alpha L^N$ satellite lines reflected the different dynamical collision processes in the SiO_2 aerogel target. The satellite energy shifts increase with the number of the L-shell vacancies including some possible excited states. The intensity ratio of all different $K_\alpha L^N$ satellite lines is determined according to their statistical weight (LS coupling) [21, 22] and the abundance of corresponding emitters with respect to the plasma parameters. Si inner shell vacancies (L-shell) are accompanied by ionization of the outer shell electrons (M-shell) resulting in different $K_\alpha L^N M^0$ or $K_\alpha L^N M^4$ satellite lines, where N is a number of the vacancies in the L-shell and M^0 means on M-shell configuration of $3s^2 3p^2$ and M^4 is the fully ionized M-shell on M-shell configuration of 0, respectively. To explain these complexes inner shell effects all possible excited and ionized charge states should be considered.

1.4.3. Argon X-ray Spectrum

In 2012, P. Neumayer *et al.* [9], have measured the PHELIX Laser power 2.5 J through in an argon droplet of 20 μm diameter recording in X-rays spectra emitted lines at the GSI Helmholtz Center, see Fig. 1.9 and they were using the theoretical code FLYCHK fitting the series of K_α emission spectral lines [9] . This argon experiment is a high
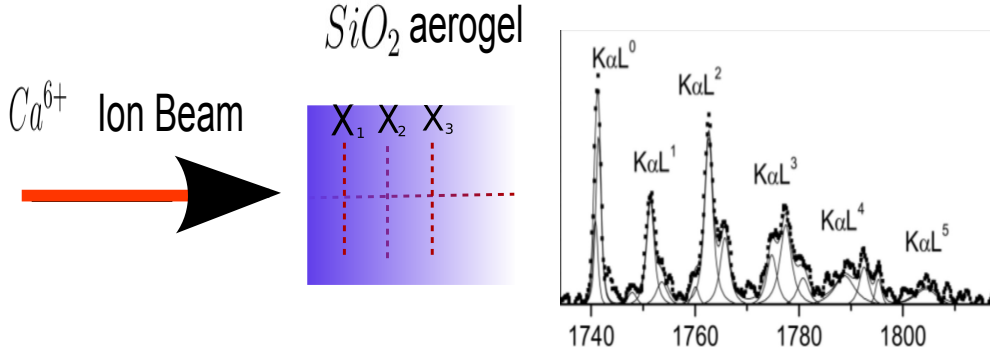
Figure 1.7.: 11.4 MeV/u Ca^{6+} ion beam projectiles penetrating into different depths of low-density SiO_2 aerogel target. K_α satellite emission transitions $2p \rightarrow 1s$ with N holes in the L shell. $K_\alpha L^N$ lines of Si atoms are influenced by the environment of oxygen atoms [15, 16].
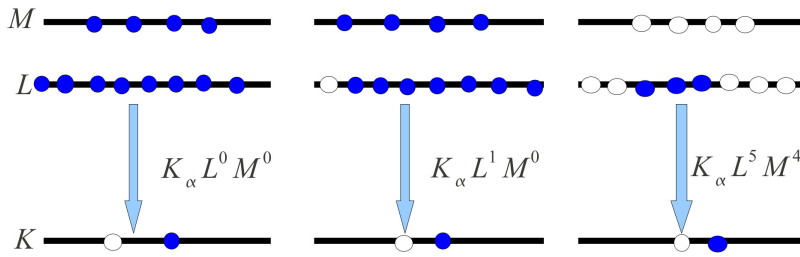

Figure 1.8.: Schematic representation for different Si emission initial configurations on $K_\alpha L^0 M^0$, $K_\alpha L^1 M^0$ and $K_\alpha L^5 M^4$ of K_α satellites initial configurations. The configuration of $K_\alpha L^0 M^0$ is $1s^1 2s^2 2p^6 3s^2 2p^2$. The configuration of $K_\alpha L^1 M^0$ is $1s^1 2s^2 2p^5 3s^2 3p^2$. The configuration of $K_\alpha L^5 M^4$ is $1s^1 2s^2 2p^1$. [15].

energy laser producing the plasma effect in the series of K_α emission spectral line model is suitable to experiment. In the Ar spectra experiment for the charge states 1+ to 9+ is about 20 eV to 30 eV apart and the charge states 10+ ... 14+ is about 20 eV to 30 eV apart with the total spectrometer covered the range of the Ar K-shell emission lines from 2940 eV to 3120 eV [9]. With lower laser energy 0.01 J one can not see the charge states 10+ ... 14+ the satellites effect but with a high laser energy 2.4 J has the stronger satellites effect of the charge states 10+ ... 14+ in experimental result [9].

In our theoretical model the bulk Ar can be roughly described with an isolated ionic emitter and accompany to increasing temperature getting greater part of atoms are ionized in the plasma environment. Plasmas was produced by high power laser can have high electron temperatures and electron densities. From the charge states 1+ to 9+ in the M shell, the effect of M-shell electrons have a similar chemical environment in the K_α spectral line. From the charge states 10+ to 14+ in the L shell with different holes accompany with $K_\alpha L^N$ (N holes in L shell) satellite lines. The lowest binding

energies could be included self-energy shift Δ and plasma composition is from ionization equilibrium with the Saha equation in the thermodynamic equilibrium. In our spectral function is Lorentz profile convoluted Gaussian instrument function depending on plasma parameters with different temperature. We Compare our theoretical spectra line with the spectral line calculation by FLYCHK [25]. Knowing exactly the charge distribution of argon is essential in studying X-rays KL lines. In this aspect, the blue shift measurement in X-rays fluorescence spectra was a good promising method.

In describing the different initial states and final states we will describe the LS coupling for Si and Ar in the Quantum Fermi system in chapter 2. In section 2.2 we will use Roothaan-Hartree-Fock (RHF) wave functions calculating the screening effect within an ion-sphere model with Bunge wave function. The Roothaan-Hartree-Fock with atomic orbitals expressed the Slater-type functions. The advantages of RHF to be more accurate could readily be incorporate into some codes for atomic calculations. In section 2.3 we will describe Roothaan Hartree Fock (RHF) with Gaussian 03. The different excitation and ionization probabilities of the electronic L-shell and M-shell lead to a charge state distribution.
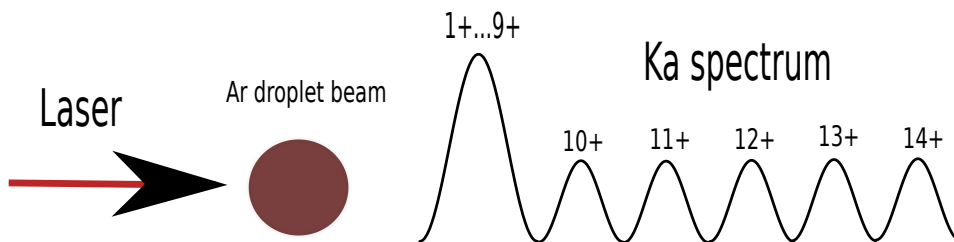

Figure 1.9.: Ar intense-laser pulses irradiated individual argon droplets. K_α spectral region from 2940 eV to 3100 eV. KL-transitions of argon at different charge state. $Ar^{1+\dots9+}$, Ar^{10+}, Ar^{11+}, Ar^{12+}, Ar^{13+} and Ar^{14+} [9].

2. Line Shift due to Excitation and Ionization

Boltzmann (1844 - 1906) was described of macroscopic systems into the microscopic statistical ensembles [26]. Statistical mechanics deals with a large number of particles in the microscopic physics. Classical statistics describe N particles in the phase space including three dimensional spatial coordinates $\mathbf{r}_1, \cdots, \mathbf{r}_{3N}$ and three dimension momentum coordinates $\mathbf{p}_1, \cdots, \mathbf{p}_{3N}$. The classical statistics particles motion of the overall system are through a phase space trajectory curve in the phase space [26]. In statistical quantum mechanics, the probability of finding a plasma particle at the spatial space $\mathbf{r}$ and the momentum space $\mathbf{p}$ with wave function ψ is defined by

$$dP(\mathbf{rp}) = |\psi_{\mathbf{p}}(\mathbf{r})|^2 \, d\mathbf{r}. \tag{2.1}$$

In order to consider the many-particle system we need an approximation of many-particles wave function instead of numerical many-particle Schrödinger wave functions. Roothaan Hartree Fock wave function method is a useful approximation many-particle wave function (1951) [30, 28, 29]. We use Roothaan Hartree Fock approximation wave functions solving many-particle system in quantum systems. *The ab initio* Gaussian 03 (G03) chemical code [34, 32, 33] is a good approximation of Hartree-Fock energy. Using G03 describes the energy eigenstates of ionization energy and excited energies of excited states in the specified ionic configurations in our cases. We calculate with Hund's rules (1927 devised by Friedrich Hund) for lowest energy of a configuration [21, 22]. The electrons could describe with spin statistics theorem applying Fermi-Dirac statistics. In section 2.1 we will introduce the Many body systems with Hartree Fock approximation. In section 2.2 we will introduce the Roothaan Hartree Fock (RHF) with the Bunge wave function. In section 2.3 the Roothaan Hartree Fock (RHF) with *ab initio* Gaussian 03.

2.1. Many Body Systems and Hartree Fock Approximation

In the quantum system has introduced some different quantum numbers to describe the specified charge states of silicon and argon. The principal quantum number n: describes the different electron shell or energy levels, on K-shell $n = 1$, on L-shell $n = 2$, and on M-shell $n = 3$. The angular momentum quantum number l is defined from 0 to $n - 1$. The l describes the sub-shell or different quantum orbits, on the s-orbital $l = 0$, on p-orbital $l = 1$, on d-orbital $l = 2$, and on f-orbital $l = 3$. The total electronic orbital angular momentum quantum number l can be described with the corresponding letter.

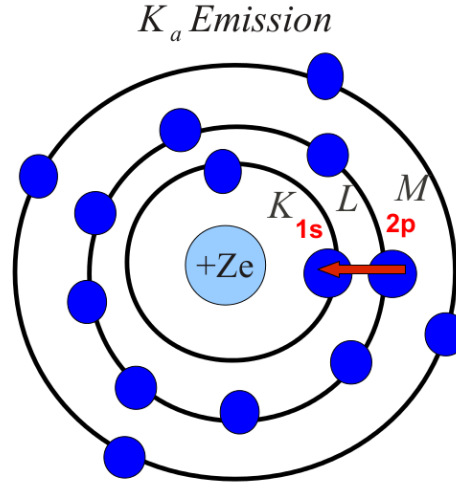| 0	1	2	3	4	5
s	p	d	f	g	h

Figure 2.1.: Si of electron of orbital. There is one electron transition from 2p to 1s shell in the K_α fluorescence emission spectral line. K shell has 1s and K shell has 2s and 2p. M shell has 3s, 3p, 3d and 4s. The transition from 2s to 1s is forbidden by selection rule.

The magnetic quantum number m_s is defined from $-l, -l+1, ...0, ..., l-1, l$. The spin number describes spin up 1/2 or spin down $-1/2$ [22, 23, 24]. In Fig. 2.1 shows the scheme of K_α emission configuration Si$^+$ with 13 electrons in the different atom orbits. The Si$^+$ configuration of initial state is $1s^1 2s^2 2p^6 3s^2 2p^2$ and configuration of final state is $1s^2 2s^2 2p^5 3s^2 2p^2$. The K_α emission configuration of initial state Si$^+$ on 3p excited state is $1s^1 2s^2 2p^6 3s^2 2p^1 3p^1$ and the configuration of final state Si$^+$ on 3p excited state is $1s^2 2s^2 2p^5 3s^2 2p^1 3p^1$. The K_α emission configuration of initial state Si$^+$ on 3d excited state is $1s^1 2s^2 2p^6 3s^2 2p^1 3d^1$ and the configuration of final state Si$^+$ on 3d excited state is $1s^2 2s^2 2p^5 3s^2 2p^1 3d^1$. The K_α emission configuration of initial state Si$^+$ on 4s excited state is $1s^1 2s^2 2p^6 3s^2 2p^1 4s^1$ and the configuration of final state Si$^+$ on 4s excited state is $1s^2 2s^2 2p^5 3s^2 2p^1 4s^1$. The Si K_α non-perturbative emission energies seeing in section 2.3.1.

The atom number Z of Ar is 18. There are 2 electrons in K-shell, 8 electrons in L-shell, and 8 electrons in the M-shell in the Ar ground state. The Ar K_α non-perturbative emission energies seeing in section 2.3.2.

Each electron is assigned to a one-electron wave function. Each electron includes the spatial coordinate and spin coordinate assigned to a one-electron wave function. At many-electron system has an approximation method to get the lowest energy of the

ground state and excited states with a trial wave function introduced by the variation approximation method.

$$E[\Psi] \equiv \frac{\langle \Psi | \hat{H} | \Psi \rangle}{\langle \Psi | \Psi \rangle} \geq E_0. \tag{2.2}$$

In Eq. (2.2) Ψ is a trial wave function and Eq. (2.2) is called Rayleigh method [23, 24]. The Hamiltonian is defined by

$$\hat{H} = \hat{T} + \hat{V}. \tag{2.3}$$

In Eq. (2.3) shows kinetic energy $\hat{T}$ with potential energy $\hat{V}$. We use a complete set $|n\rangle$ of commutator observables

$$\langle \Psi | \hat{H} | \Psi \rangle = \sum_n \langle \Psi | n \rangle \langle n | \hat{H} | \Psi \rangle = \sum_n \langle \Psi | n \rangle E_n \langle n | \Psi \rangle. \tag{2.4}$$

The normalized factor is $\langle \Psi | \Psi \rangle =1$. The energy level of the hydrogen atom is given by [22],

$$E_n = - \left(\frac{m_e e^4}{32\pi^2 \epsilon_0^2 \hbar^2} \right) \frac{1}{n^2}, \quad n = 1, 2, \cdots . \tag{2.5}$$

In Eq. (2.5) m_e is the electron mass, e is the elementary charge, $\hbar$ is the reduced Planck constant, ϵ_0 is the vacuum permittivity. And Eq. (2.5) describes the energy levels of the atom $E_n \propto -\frac{1}{n^2}$. That is if $n \to \infty$ then E_n going to zero. The ionization energy was defined by an electron removal from energy state E_n to energy state E_∞ getting the energy difference $-(E_\infty - E_n)$. Now we pay attention to an approximation of the many-particle system of Hartree-Fock approximation model [29, 22]. Hartree-Fock is a self-consistent field (SCF) method to find resolutions for non-relativistic Schrödinger equation in the stationary states. An antisymmetric operator of fermion $\hat{A}^-$ can be described by sum all of the permutation operators $\hat{P}$ in the N fermion system:

$$\hat{A}^- = \frac{1}{\sqrt{N!}} \sum_P (-1)^P \hat{P}. \tag{2.6}$$

The non-relativistic Hamiltonian H of N electrons is given by

$$\hat{H} = \hat{H}(1, 2, 3, ..., N). \tag{2.7}$$

In Eq. (2.7) parentheses describe the degree of freedom on spatial orbital and spin orbital from one electron to Nth electron. At one electron orthonormal particle wave function is also called a molecular spin orbit (MSO).

$$\varphi_i(k) = \varphi_i(\hat{r_k})\chi_i(m_{sk}). \tag{2.8}$$

In Eq. (2.8) k denotes the particle of number k, index i is an eigenstate of particles, r_k is spatial part and m_{sk} is spin part. The wave function of many particle products all of one particle orthonormal particle wave function involving minimizing Rayleigh ration for the lowest Energy.

$$\Psi = \varphi_1(1)\varphi_2(2)...\varphi_N(N). \tag{2.9}$$

2. Line Shift due to Excitation and Ionization

The total electron wave functions Ψ can describe with Slater determinant

$$\Psi = \frac{1}{\sqrt{N!}} \begin{vmatrix} \varphi_1(1) & \varphi_1(2) & \cdots & \varphi_1(N) \\ \varphi_2(1) & \varphi_2(2) & \cdots & \varphi_2(N) \\ \vdots & \vdots & \ddots & \vdots \\ \varphi_N(1) & \varphi_N(2) & \cdots & \varphi_N(N) \end{vmatrix}.$$

The Slater determinant describes all of the permutations at all possible $\varphi_i(k)$ sets, even ones with a plus sign, the odd ones with a minus sign and the normalization condition $\langle \Psi | \Psi \rangle = 1$. In closing electron shells, the occupied electrons must satisfy the Pauli principle. The Pauli principle means no two identical fermions to occupy in a same quantum state. There is no possible two row elements or two column elements in a same quantum state in the Slater determinant. In open electron shells, the Slater determinant is a linear combination with different statistical factor on the components. The variational theory requires minimization of energy at the wave function. The Hamiltonian Eq. (2.3) consists of single particle and two particles Coulomb interaction contribution rewritten.

$$\hat{H} = \hat{H}^{(1)} + \hat{H}^{(2)} = \sum_{i=1}^{N} \hat{H}_i + \sum_{\substack{i,j=1, \\ i>j}}^{N} \hat{H}_{ij} \tag{2.10}$$

$$= \sum_{i=1}^{N} \left(-\frac{\hbar^2}{2m}\nabla_i^2 - \frac{Ze^2}{4\pi\epsilon_0 \hat{r}_i} \right) + \sum_{\substack{i,j=1, \\ i>j}}^{N} \frac{e^2}{4\pi\epsilon_0 \hat{r}_{ij}}. \tag{2.11}$$

In Eq. (2.10) the first term is a single particle Hamiltonian including of kinetic energy and nuclear Coulomb potential. The second term is Coulomb repulsive interaction of two electrons. Now we discuss more detailed Coulomb interaction splitting to the direct interaction and exchange interaction by [27]

$$E[\varphi] = \langle \Psi | H | \Psi \rangle = \sum_{i=1}^{N} 2I_i + \sum_{i,j}^{N} [2J_{ij} - K_{ij}] \tag{2.12}$$

$$I_i = \int dr_1 \varphi_i^*(r_1) H_1 \varphi_i(r_1), \tag{2.13}$$

$$J_{i,j} = \int dr_1 dr_2 \varphi_i^*(r_1) \varphi_j^*(r_2) H_{12} \varphi_i(r_1) \varphi_j(r_2) \tag{2.14}$$

$$K_{i,j} = \int dr_1 dr_2 \varphi_i^*(r_1) \varphi_j^*(r_2) H_{12} \varphi_i(r_2) \varphi_j(r_1). \tag{2.15}$$

In Eq. (2.14) $J_{i,j}$ is the direct term of the Coulomb potential and in Eq. (2.15) $K_{i,j}$ is an exchange term in the Coulomb interaction.

We introduce Russell-Saunders coupling scheme to describe the state of atom in many electrons. Russell-Saunders coupling scheme includes the total spin $\hat{S}$, the total orbital

angular momentum $\hat{L}$, and the total angular momentum $\hat{J}$.

$$\hat{S} = \hat{s}_1 + \hat{s}_2, \hat{s}_1 + \hat{s}_2 - 1, ..., |\hat{s}_1 - \hat{s}_2|$$
$$\hat{L} = \hat{l}_1 + \hat{l}_2, \hat{l}_1 + \hat{l}_2 - 1, ..., |\hat{l}_1 - \hat{l}_2|$$
$$\hat{J} = \hat{j}_1 + \hat{j}_2, \hat{j}_1 + \hat{j}_2 - 1, ..., |\hat{j}_1 - \hat{j}_2|.$$

$$\hat{J} = \sum_i \hat{j}_i = \hat{L} + \hat{S} = \sum_i \hat{l}_i + \sum_i \hat{s}_i. \tag{2.16}$$

In Eq. (2.16) the core electrons of a closed shell can neglect because J is zero. In 1927, Friedrich Hund had devised Hund's rules [21, 22] in the lowest energy of a configuration. There are three rules in Hund's rules. The first rule is the electrons in a closed shell and there is a maximum multiplicity $2S + 1$ (called g-factors). The second rule describes the two electrons locate in the different shell, S and L considering maximal for a given multiplicity in the lowest energy. The third rule is the level with the lowest J at half-filled or less at outer sub-shell in the lowest energy. The third rule considers the energy shifts due to spin-orbit coupling. The spin-orbit coupling effects on spectra. The silicon and argon g-factors in the ground and excited state (2p,3s,3p,3d,4s) are shown in Tab. 2.1.

Charge	gd	ex(4s)	(3d)	(3p)	(3s)	(2p)	Charge	gd	ex(4s)	(3d)	(3p)	(3s)	(2p)
Si	5	5	9				Si^+	4	2	6			
Si^{2+}	1	3	7	5			Si^{3+}	2	2	6	4		
Si^{4+}	1		9	7	5		Si^{5+}	4		10	8	6	
Si^{6+}	5		9	7	5		Si^{7+}	4		10	8	6	
Si^{8+}	5		9	7	5		Si^{9+}	4		6	4	2	
Si^{10+}	1		7		3	5	Si^{11+}	2		6		2	4
Si^{12+}	1		7		3	5							
Charge	**gd**	**ex(4s)**	**(3d)**	**(3p)**	**(3s)**	**(2p)**	**Charge**	**gd**	**ex(4s)**	**(3d)**	**(3p)**	**(3s)**	**(2p)**
Ar	1	5	9				Ar^+	4	6	10			
Ar^{2+}	5	5	9				Ar^{3+}	4	6	10			
Ar^{4+}	5	5	9				Ar^{5+}	4	2	6			
Ar^{6+}	1	3	7				Ar^{7+}	2	2	6	7		
Ar^{8+}	1		9	8	5		Ar^{9+}	4		10	7	6	
Ar^{10+}	5		9	8	5		Ar^{11+}	4		10	7	6	
Ar^{12+}	5		9	4	5		Ar^{13+}	4		6	5	2	

Table 2.1.: Silicon and argon statistical factors (dg: ground state, ex: excited states) with different charge states.

We use LS coupling for Si and Ar statistical factor calculation, for example: $l = 1$, $s = \frac{1}{2}$, $j = \frac{3}{2}$ or $l = 1$, $s = \frac{1}{2}$, $j = \frac{1}{2}$. Fine structure describes the splitting of the spectral lines of atoms and influences the K_α emission line at splitting off $P_{3/2}$ or $P_{1/2}$. In the next section we will pay attention to Roothaan Hartree Fock (RHF) with the Bunge wave function.

2.2. Roothaan Hartree Fock with Bunge Wave Function

Si atom including 14 electrons are bounded to the nucleus in a many body system. Ar atom including 18 electrons are bounded to the nucleus in a many body system. We use the self-consistent Roothaan-Hartree-Fock approximation method to solve the many body systems. The unperturbed Hamiltonian H^0 includes each single particle Hamiltonian, the Coulomb interaction potential and the exchange potential in Hartree-Fock approximation, see Eq. (2.10), Eq. (2.14) and Eq. (2.15). RHF wave functions calculate ground state and excited states of neutral with ionized atoms from He through Xe (Z = 2 - 54) [28, 29]. The nucleus is considered keeping in a fixed position and the motion of electrons on the orbits are neglected. Roothaan Hartree Fock is an approximation to the conventional Hartree Fock wave functions with radial atomic orbitals R_{nl}

$$\mathbf{R_{nl}} = \sum_j \mathbf{S_{jl}} \mathbf{C_{jln}}. \tag{2.17}$$

In Eq. (2.17) $\mathbf{C_{jln}}$ collects the orbital expansion coefficients, see App. 2.2, the radial atomic orbitals are expanded as a finite superposition of primitive radial functions $\mathbf{S_{jl}}$

$$\mathbf{S_{jl}} = N_{jl}\mathbf{r}^{(n_j l - 1)} e^{(-Z_{jl}\mathbf{r})}. \tag{2.18}$$

In Eq. (2.18) n_{jl} is the effective principal quantum number, l is the azimuthal quantum number and Z_{jl} is orbital exponent coefficients, see Tab. 2.2. The normalization factor

$$N_{jl} = \frac{(2Z_{jl})^{n_{jl}+1/2}}{[(2n_{jl})!]^{1/2}}. \tag{2.19}$$

The Bunge wave function combines the radial term and sphere angle term

$$\varphi_{nlm}(\mathbf{r}, \theta, \phi) = \mathbf{R_{nl}}(\mathbf{r}) \cdot \mathbf{Y_{lm}}(\theta, \phi) \tag{2.20}$$

$$= \sum_j \mathbf{S_{jl}} \mathbf{C_{jln}} \cdot \mathbf{Y_{lm}}(\theta, \phi) \tag{2.21}$$

$$= \sum_j N_{jl}\mathbf{r}^{(n_j l - 1)} e^{(-Z_{jl}\mathbf{r})} \mathbf{C_{jln}} \cdot \mathbf{Y_{lm}}(\theta, \phi). \tag{2.22}$$

The Roothaan Hartree Fock equations [28, 29] are self-consistent-field equations getting minimizing energy,

$$\mathbf{F_{closed}} \cdot \mathbf{C} = \mathbf{E} \cdot \mathbf{S} \cdot \mathbf{C} \tag{2.23}$$
$$\mathbf{F_{open}} \cdot \mathbf{C} = \mathbf{E} \cdot \mathbf{S} \cdot \mathbf{C} \tag{2.24}$$

In Eq. (2.23), $\mathbf{F_{closed}}$ is the closed shell Fock matrices, $\mathbf{F_{open}}$ is the open shell Fock matrices, $\mathbf{S}$ is overlap matrix, $\mathbf{C}$ is the orbital expansion coefficients $\mathbf{C_{jln}}$ and $\mathbf{E}$ is vector holds the different orbital energies. The Argon parameters, see Tab. 2.3 and 2.4.

The probability of radial wave function is defined by

$$r^2 |R_{nl}(r)|^2 = r^2 \int d\theta d\phi \sin(\theta) |\varphi_{nlm}(r, \theta, \phi)|^2. \tag{2.25}$$

n_{jl}	Z_{jl}	$C1s$	$C2s$	$C3s$	n_{jl}	Z_{jl}	$C2p$	$C3p$
1S	19.5017	0.377006	0.064222	0.023528	2P	15.7304	0.015661	-0.001966
1S	11.7539	0.454461	-0.472631	-0.136207	2P	7.2926	0.196557	-0.057175
2S	16.9664	0.200676	0.055383	0.019663	2P	4.6514	0.510448	-0.068127
2S	6.3693	0.00149	0.233799	0.074362	2P	3.3983	0.303956	-0.114298
2S	4.5748	0.001201	0.781919	0.122580	3P	12.0786	0.025586	-0.001976
2S	3.3712	-0.000454	0.96627	0.206180	3P	2.0349	0.003153	0.263703
3S	36.5764	-0.000507	0.000257	0.000048	3P	1.3221	0.000167	0.522698
3S	2.4996	0.000103	-0.001832	-0.319063	3P	0.9143	0.000156	0.314467
3S	1.6627	-0.000053	0.000879	-0.562578				
3S	1.1812	0.000013	-0.000033	-0.280471				

Table 2.2.: Silicon:n_{jl},Z_{jl},C_{jln} [28, 29].

n_{jl}	Z_{jl}	$C1s$	$C2s$	$C3s$	n_{jl}	Z_{jl}	$C2p$	$C3p$
1S	25.5708	0.316405	0.079148	0.035512	2P	26.6358	0.002436	0.00185
1S	15.6262	0.542760	-0.507823	-0.181267	2P	12.7337	-0.114774	-0.042064
2S	22.3994	0.167691	0.059900	0.026500	2P	7.3041	-0.503175	-0.095603
2S	10.5300	0.000408	-0.026389	0.006280	2P	5.3353	-0.427033	-0.194233
2S	7.0534	0.002431	0.832638	0.111836	3P	20.7765	0.009669	0.005891
2S	5.4120	-0.000861	0.295522	0.385604	3P	3.3171	-0.004825	0.366141
3S	46.7052	-0.000422	0.000217	0.000070	3P	2.0947	0.000231	0.526490
3S	3.7982	0.000066	0.002203	-0.376901	3P	1.3780	-0.000098	0.249866
3S	2.5495	-0.000061	0.001423	-0.593561				
3S	1.7965	0.000009	0.000186	-0.229971				

Table 2.3.: Argon:n_{jl},Z_{jl},C_{jln} [28, 29]

In Eq. (2.25) the area of probability is $\int_0^\infty r^2 |R_{nl}(r)|^2 = 1$ The probability of Si radius wave function with the different orbits, see Fig. 2.2. We see the 1s wave function location in radial distance from the nucleus of 0 a_B to 0.4 a_B, 2s and 2p wave functions are located from 0 a_B to 1.0 a_B, 3p and 3s wave functions are very small contribution inside of $a_B = 1$. The probability of Ar radius wave function with the different orbits, see Fig. 2.3. We see the 1s wave function location in radial distance from the nucleus of 0 a_B to 0.4 a_B, 2s and 2p wave functions are located from 0 a_B to 1.0 a_B, 3p and 3s wave functions are very small contribution inside of $a_B = 1$.

The Si ground state energy of RHF was -288.8543622 Hartree and Si ground state energy of Exact HF was -288.8543624 Hartree (1 Hatree= 1 a.u. = 27.2113961 eV). The

E	1s	2s	3s	2p	3p
	-118.610349	-12.322152	-1.277352	-9.571464	-0.591016

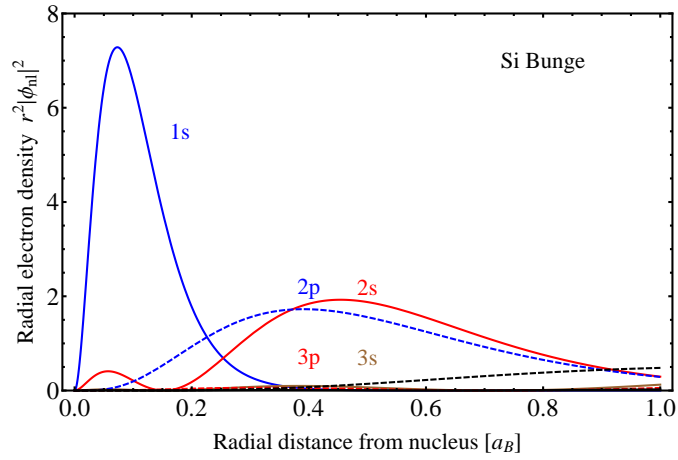Table 2.4.: Orbital energy of Argon [28, 29]

Figure 2.2.: Si radial probability distributions $r^2 \left| R_{nl}(r) \right|^2$ of the Bunge wave functions. Including 1s, 2s, 2p, 3s, 3p, 3d and 4s orbitals. 3d and 4s have a very small contribution.

Figure 2.3.: Ar radial probability distributions $r^2 \left| R_{nl}(r) \right|^2$ of the Bunge wave functions. Including 1s, 2s, 2p, 3s, 3p, 3d and 4s orbitals. 3d and 4s have a very small contribution.
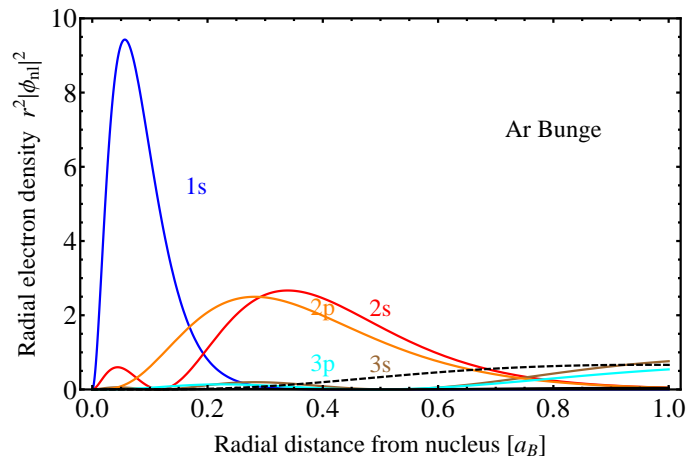
Ar ground state energy of RHF was -526.8175122 Hartree and Si ground state energy of Exact HF was -526.8175126 Hartree shows the RHF energy is less than 1 MeV in error [29]. Energy $= 1\mathrm{H}(1 + \frac{m_e}{m_{\mathrm{nuclear}}})^{-1}$ with m_e electron mass and m_{nuclear} nuclear mass. We get Roothaan-Hartree-Fock ground state atomic wave functions from [28, 29, 30].

In section 3.3.2 we will use Bunge wave function on the perturbation Hamiltonian K_α initial wave function Ψ_{1s} and final wave function Ψ_{2p} calculating perturbative screening plasma potential.

2.3. Roothaan Hartree Fock with Gaussian 03

Another well presentation RHF is the linear combinations of *ab initio* Gaussian 03 basis functions. The *ab initio* G03 program is used for molecular electronic structure to give the lowest spin unrestricted Hartree-Fock (UHF) energy for the ground state of the atom. We calculate self-consistent RHF description of isolated ionic emitter H^0. The Hartree Fock energy is defined by

$$\mathbf{F_r}\varphi_i(\mathbf{r}) = \epsilon_i\varphi_i(\mathbf{r}), i = 1, ..., N. \tag{2.26}$$

And the Fock term $\mathbf{F_r}$ is given by

$$\mathbf{F_r} = -\frac{\hbar^2}{2m}\nabla_{\mathbf{r}}^2 - \frac{Ze^2}{4\pi\epsilon_0\mathbf{r}} + \sum_j 2J_j(\mathbf{r}) - K_j(\mathbf{r}). \tag{2.27}$$

In Eq. (2.27) shows the direct interaction potential $J_j(\mathbf{r})$ and the exchange interaction potential $K_j(\mathbf{r})$. The RHF wave function is given by

$$\varphi_{nlm}(r) = \sum_j \mathbf{C_{nlm,j}X_j}(\mathbf{r}). \tag{2.28}$$

In Eq. (2.28) shows the $\mathbf{X_j}(\mathbf{r}) = \sum_g \mathbf{K_{j,g}G_g}(\mathbf{r})$ combination Gauss parameter $\mathbf{G_g}(\mathbf{r}, l_x, l_y, l_z)$. In APP. Tab. A.2, A.3, A.4 show $\mathbf{K_{j,g}}$ and $\mathbf{G_g}(\mathbf{r})$ in the silicon case. Recently *ab initio* Gaussian 03 codes was calculated integral over Cartesian Gaussian for Gaussian orbits instead of spherical harmonic Gaussian. The conversion relationship between normalized Cartesian and pure spherical harmonic Gaussian in [31]. Cartesian Gaussian orbits were presented

$$\mathbf{G}(\mathbf{r}, \mathbf{l_x}, \mathbf{l_y}, \mathbf{l_z}, \alpha) = N(l_x, l_y, l_z, \alpha)x^{l_x}y^{l_y}z^{l_z}e^{-\alpha\mathbf{r}^2}. \tag{2.29}$$

In Eg. (2.29) shows the angular momentum $l = l_x + l_y + l_z$ and the normalization factor $N(l_x, l_y, l_z, \alpha) = \left[\frac{(2l_x!)(2l_y!)(2l_z!)\pi^{3/2}}{l_x!l_y!l_z!(\alpha^{l+3/2})(2^{2l})}\right]^{-1/2}$ [31]. We use 3-21G* (19 basis functions) [32] calculating argon specific charge states of unperturbed ground state and specified unperturbed excited states (3p, 3d, 4s) in chemical *ab initio* code G03. The 3-21G* self-consistent molecular-orbital could applying from H atom to Xe atom. The name of 3-21G* means a linear combination of three Gaussian primitives and valence functions split into two and one Gaussian parts for the inner-shell basis function with * notation

has a polarization functions on Na-Ar only more detailed, see [32]. We use Aug-cc-pVTZ (50 basis functions)[34] calculating Ar specified charge states of unperturbed ground state and specified unperturbed excited states (3p, 3d, 4s). The AUG-cc-pVTZ is used in correlated molecular calculations for Na-Ar atoms having the valence polarization function included in (5s, 4p, 2d, 1s) basis sets more detailed is shown in [34].

2.3.1. Silicon using 3-21G* Basis

At 3-21G* basis, there are 19 basis functions (bf), 33 primitive Gaussian (pg), 19 Cartesian basis functions, 8 alpha electrons and 6 beta electrons. For example, at Si ground state the Energy is -287.392361589 eV on 3-21G* basis. In App. A.3, there are alpha occupied eigenvalues (a.o.), 11 alpha virtual eigenvalues (a.v.) and 6 beta occupied eigenvalues (b.o.), 13 beta virtual eigenvalues (b.v.) in 3-21G* basis.

The first order of ionization energy of Si defined by removed an electron from the Si atom in the gaseous state defined by

$$Si \rightarrow Si^+ + e^- \tag{2.30}$$

the second order of ionization energy of Si is defined by

$$Si^+ \rightarrow Si^{2+} + e^- \tag{2.31}$$

and continuing in this manner for the higher order values. The first order binding energy of Si combines the ion and 14 electrons in the atomic bound system. The second order binding energy of Si combines the ion and 13 electrons in the atomic bound system. The second order binding energy of Si can get from

$$\text{The first order binding energy} - \text{The first order ionisation energy.} \tag{2.32}$$

In Eq. (2.32) as the removed electrons can no longer screen the core the remaining electrons are bound the stronger and more energy is needed to remove the next electron. In Fig. 2.4a are only energies of the ground state of the corresponding ion, however energies of excited ions show a similar behavior. At $N = 10$ is due to the fact that for larger N there are still electrons in the M-shell which are much less bound than L-shell electrons. The results for different ionization stages are shown in Fig. 2.4b. From Si^+ to Si^{4+} the ionization of the outermost electron occurs in the M-shell, then from Si^{5+} to Si^{9+} in the L-shell. Again there is a massive rise in the energies when more and more inner electrons are removed. In order to calculate $K_\alpha L^N$ line emissions, we use again the Gaussian 03 code. The program is used to determine the energies of the ion in initial and final configuration, respectively. The emission energy is then the difference of those two values. We compare our result of the first emission energy $(K_\alpha L^0 M^0)$ with different experimental and theoretical values in Tab. 2.5. The range of the given Si K_α values is 1740 ± 1 eV. Our results agree to vary well with those findings. The K_α emission energies of different charge states of Si. Ionization from Si^+ to Si^{4+} occurs in the M-shell, from Si^{5+} to Si^{9+} in the L-shell, see Fig. 2.5.

(a) Binding energy of $Si^{(14-N)+}$ ions obtained by G03. There are 4 electrons in the M shell having similar binding energy.

(b) The ionization energy of $Si^{(14-N)+}$ ions obtained by G03.
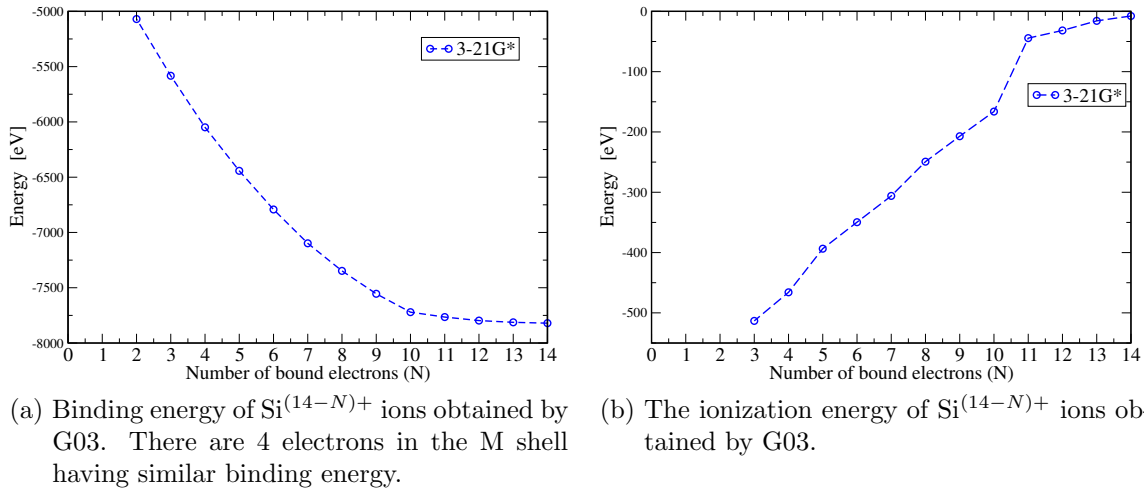
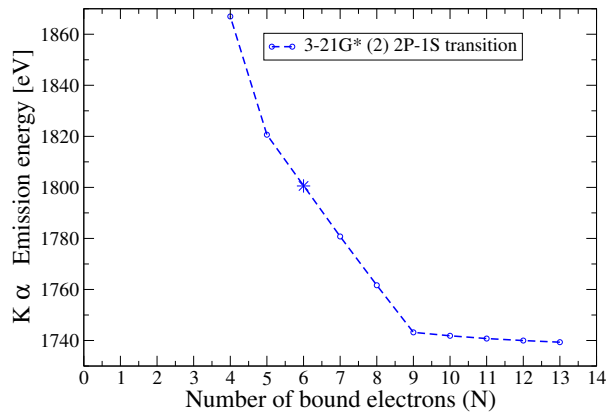Figure 2.4.: Energy values for different charge states of the ground state Si getting by G03 3-21G* basis set.

Figure 2.5.: K_α emission energies of different charge states of Si. Ionization from Si^+ to Si^{4+} occurs in the M-shell with K_α emission energy around 1740 eV, from Si^{5+} to Si^{9+} in the L-shell with larger K_α emission energy.

2. Line Shift due to Excitation and Ionization

K_{α_1} [eV]	K_{α_2} [eV]
1741.2 [35]	1741.2 [35]
1741.2 [35]	1739.7 [35]
1739.985 [35]	1739.394 [35]
1740 [12]	1739.4 [12]
1739.98 [13]	1739.48 [13]
1739.98 [20]	1739.47 [20]
1739.89 (this work)	1739.299 (this work)

Table 2.5.: Different experimental and theoretical values for K_{α_1} and K_{α_2}. The K_α initial configuration is $1s^1 2s^2 2p^6 3s^2 3p^2$ and the K_α final configuration is $1s^2 2s^2 2p^5 3s^2 3p^2$. Last stated values are our results.

Si $K_\alpha L^N M^0$ (0< N< 5) satellite lines correspond to radiative decays of atomic states with no hole in the M-shell, N holes in the L-shell and one hole in the K-shell. Si $K_\alpha L^N M^4$ (0< N< 5) satellite lines correspond to radiative decays of atomic states with 4 holes in the M-shell (i.e. the M-shell is fully ionized), N holes in the L-shell and one hole in the K-shell. In Fig. 2.6 shows the SiO_2 experiment results shown in section 1.4.2 [16] describes the Multi-Configuration Dirac Fock approximation to calculate the M^4 and M^0. We see the M^4 behavior far away from experiment than M^0 because the screening effect from M shell (4 electrons occupied in M shell) and M^0 is a little away from experiment because the experiment SiO_2 having Si components describing $K_\alpha L^N M^0$ (0< N< 5) satellite line.
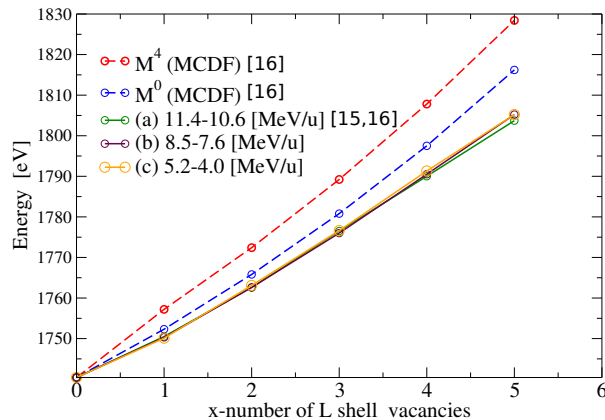

Figure 2.6.: K_α emission energies of different charge states of Si. Experimental values [15, 16] compared with theoretical values [16] obtained from multi-configuration Dirac-Fock approximation (MCDF).

The Tab. 2.6 compares theoretical and experimental results of [35] with our calculations of $K_\alpha L^N$ (N=0-6). Shown are the satellite energy shifts with respect to $K_\alpha L^0$. In Fig. 2.7 shows the M^4 using the Aug-cc-pVTZ basis set and 3-21G* basis set including some different configuration excited emission energies. We see the $K_\alpha L^0 M^4 = 1746.59$

eV in Aug-cc-pVTZ basis set and $K_\alpha L^0 M^4 = 1743.205$ eV in 3-21G* basis set. The distance of each segment is roughly 16 eV of the $K_\alpha L^0 M^4$ satellites emission lines. Moreover, we plotted the both theoretical results for M^4 in Fig. 2.8a as well as for M^0 in Fig. 2.8b. We achieved a good agreement with the results of Rzadkiewicz *et al.*, which apply MCDF calculations to determine the different emission energies. Further, our results are in the order of the experimentally measured satellite energies of emissions due to heavy ion collisions with the silicon target. Of course, there occur a lot of dynamical processes during the collisions resulting in different emitter configurations within a changing plasma environment at different target depth. In order to resemble the measurements we will neglect the dynamical collisions, but a warm dense plasma environment to the emission satellites calculated so far. Silicon consider the different configurations of the emitting Si ion $(1s^1 2s^2 2p^\alpha, \alpha = 6, 5, 4)$ that corresponds to $K_\alpha L^N, N = 0, 1, 2$. In order to observe $K_\alpha L^N$ lines, we use Gaussian 03 codes to calculate the atomic states. The shift to higher emission energies is known as blue line shift due to ionization [27]. Synthetic spectra have been evaluated and compared with experimental data. As the $K_\alpha L^N$ spectra are emitted from a silicon plasma, we are able to infer plasma parameters by studying the line profiles.

satellite	M^4 [35]	M^4 this work	M^0 [35]	M^0 this work	experiment [35]
$K_\alpha L^0$		1743.21		1739.89	
$K_\alpha L^1$	16.8	18.45	11.9	12.25	9.7±1.0
$K_\alpha L^2$	32.0	32.32	25.4	24.24	22.7±0.9
$K_\alpha L^3$	48.8	48.95	40.4	37.2	36.2±1.0
$K_\alpha L^4$	67.4	69.61	57.1	58.8	50.9±1.2
$K_\alpha L^5$	88.0	89.15	75.8	75.7	64.8±1.6

Table 2.6.: Satellite energy shifts with respect to $K_\alpha L^0$.

2.3.2. Argon using Aug-cc- pVTZ Basis

The basis set should be suitable chosen for the ground state of energy and excited states of energies. At Aug-cc- pVTZ basis set, there are 50 basis functions (bf), 119 primitive Gaussian (pg), 59 Cartesian basis functions. 8 alpha electrons 6 beta electrons. α-orbitals: occupied 8 eigenvalues (a.o.) and virtual 42 eigenvalues (a.v.), β-orbitals: occupied 6 eigenvalues (b.o.) and virtual 44 eigenvalues (b.v.). For showing the G03 is a suitable method we compare our ionization energy with different theoretical values in Fig. 2.9 showing R. D. Cowan (1981) data from [36] and LANL data from [37] very well. In Fig. 2.9 shows the ionization energy of the M shell having similar distance to the next stage for K_α calculate the electrons in the M shell occupied an outside shell more easy ionization, see Tab. 2.7.

In Fig. 2.10a shows the different states of binding energies, for the charge states 0 to 8+ have similar binding energies between -14000 eV to -14500 eV in the M shell. At the L shell beginning from 9+ to 14+ have sharply increasing binding energy between
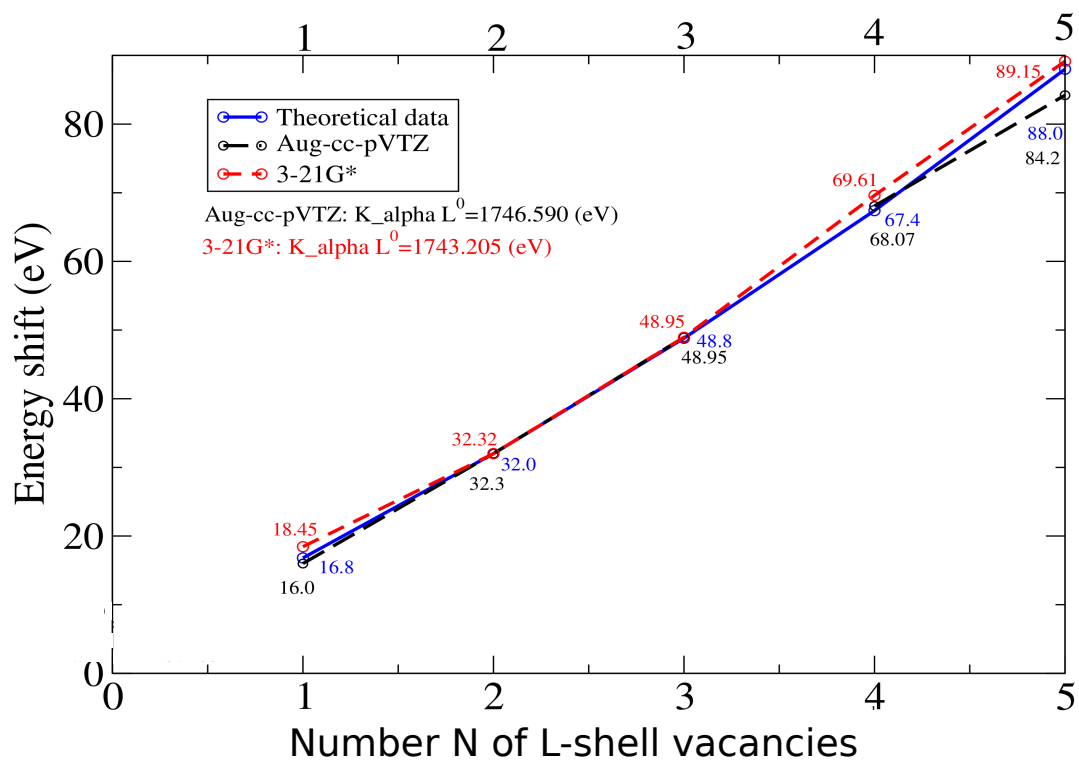
Figure 2.7.: K_α emission energies of different charge states of Si. Comparing the Aug-cc-pVTZ and 3-21G* basis set with theoretical data. Excited configurations are possible considering. Theoretical data with $K_\alpha L^0$ are from [35].
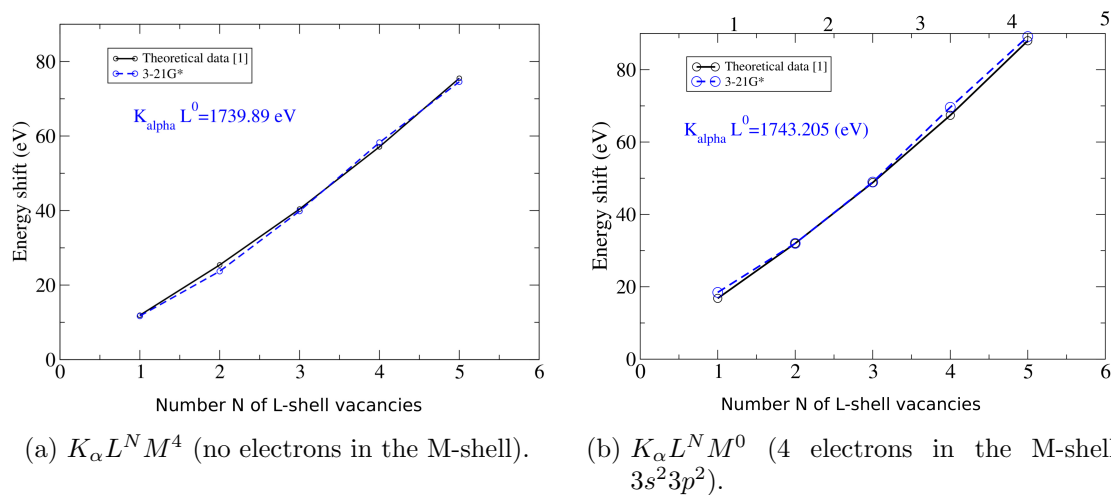

(a) $K_\alpha L^N M^4$ (no electrons in the M-shell).

(b) $K_\alpha L^N M^0$ (4 electrons in the M-shell $3s^2 3p^2$).

Figure 2.8.: Comparison of $K_\alpha L^N$ satellite energy shifts with respect to $K_\alpha L^0$. Theoretical data taken from [35] are shown in Fig. 2.6.

Ar^+	Ar^{2+}	Ar^{3+}	Ar^{4+}	Ar^{5+}	Ar^{6+}	Ar^{7+}
-14.57 [1]	-26.37 [1]	-39.39[1]	-58.49 [1]	-73.93 [1]	-90.30 [1]	-121.88[1]
-15.76 [2]	-27.63 [2]	-40.74[2]	-59.81 [2]	-75.02 [2]	-91.01 [2]	-124.32 [2]
-15.56 [3]	-27.44 [3]	-40.47[3]	-59.05 [3]	-74.71 [3]	-91.26 [3]	-123.22 [3]
Ar^{8+}	Ar^{9+}	Ar^{10+}	Ar^{11+}	Ar^{12+}	Ar^{13+}	Ar^{14+}
-142.42 [1]	-422.56 [1]	-480.40 [1]	-540.25 [1]	-622.20 [1]	-685.36 [1]	-749.41 [1]
-143.46 [2]	-422.45 [2]	-478.69 [2]	-538.96 [2]	-618.26[2]	-686.11[2]	-755.75[2]
-143.70 [3]	-422.15[3]	-479.65 [3]	-540.12[3]	-619.27[3]	-686.28[3]	-757.33 [3]

Table 2.7.: Ionization energy [eV] with different ground state using Aug-cc-pVTZ.
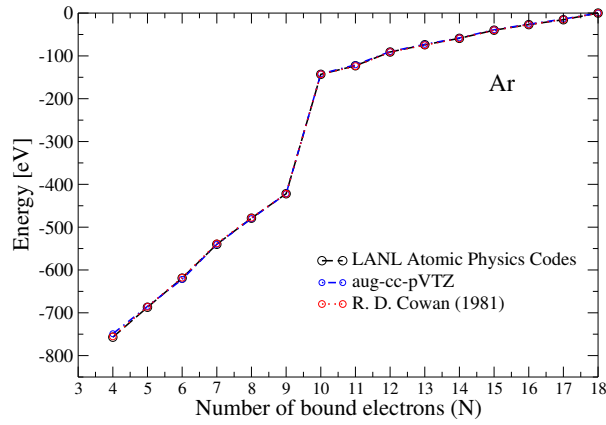[1]this work [2]R. D. Cowan(1981) [36]. [3]LANL Atomic Physics Codes [37].

Figure 2.9.: Ionization energy for the different ground state of comparing with $Ar^{(18-N)}$ ions different theoretical values.

(a) Binding energy of $Ar^{(18-N)+}$ ions obtained by G03. There are 8 electrons in the M shell having similar binding energy.

(b) Ionization energy calculating excited states of 3d (black curve) excited states of 4s and 3s (green curve), excited states of 3p (red curve) and ground states of $Ar^{(18-N)+}$ ions (blue curve) by G03.
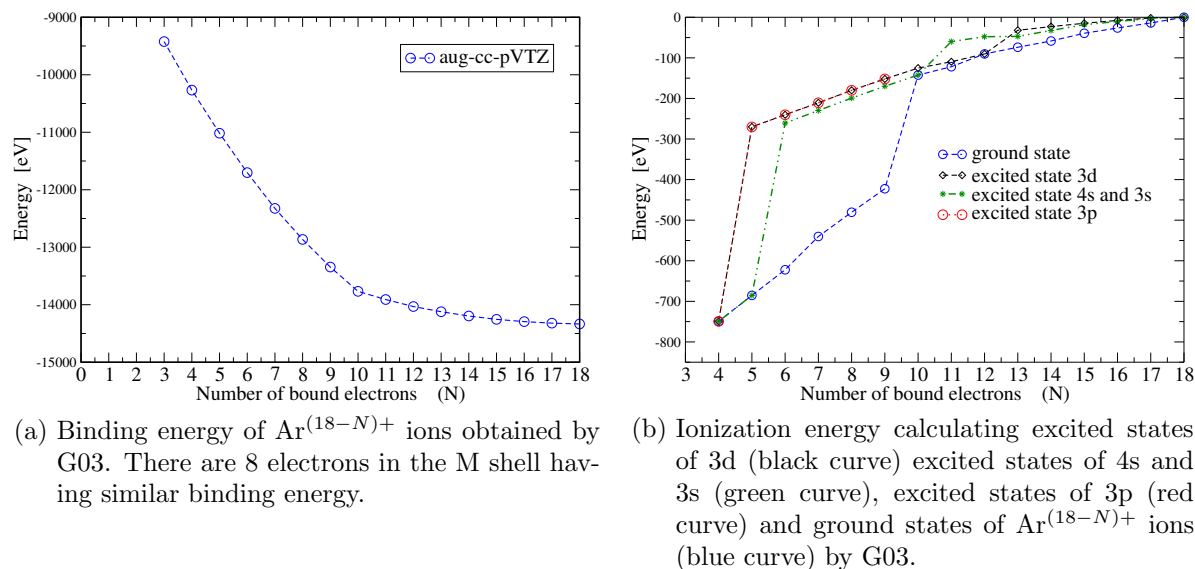
Figure 2.10.: Energy values for different charge states of the ground state Ar.

-13500 eV to -10000 eV and have similar binding energies separated distance between two different charges. In Fig. 2.10b shows the different ground states of the ionization energies and the different excited states of excited energies. And in Fig. 2.10b the blue line shows the ground state energies have a sharp gap between the last charge state of M shell to beginning L shell. The excited energies of 3d excited state and 3p excited state have the very similar excited energies. From excited energies of 3p, 3d and 4s describe the electron on M shell excited not existed the gap between charge state 8+ to 9+ strongly depending the M shell state ionization energies. Because we take the outer electron from an outer shell excited to 3p, 3d or 4s state for getting the different state excited state energies, this outer electron in the M shell has closed ionization energies like in the M shell

The cold K_α emission energy is 2957 eV getting by NIST. [9]. Ar K_α radiation emission energies see Fig. 2.11. The fluorescence spectra $K_{\alpha 1}$ and $K_{\alpha 2}$ are comparing in Tab. 2.9 the ground state of different charge states, see Tab. 2.8. Different K_α satellite emissions originate from different configurations of the emitting Ar ions.

Ar^+	Ar^{2+}	Ar^{3+}	Ar^{4+}	Ar^{5+}	Ar^{6+}	Ar^{7+}
2957.12	2957.10	2958.09	2959.07	2961.01	2962.07	2965.65
Ar^{8+}	Ar^{9+}	Ar^{10+}	Ar^{11+}	Ar^{12+}	Ar^{13+}	Ar^{14+}
2966.70	2969.03	2993.08	3017.96	3023.01	3054.59	3086.60

Table 2.8.: Emission energy [eV] with different ground state using aug-cc-pVTZ.

In order to calculate $K_\alpha L^N$ line emissions, we use again the Gaussian 03 code. The program is used to determine the energies of the ion in initial and final configuration, respectively. The emission energy is then the difference of those two values. From Ar^+ to Ar^{8+} the ionization of the outermost electron occurs in the M-shell, then from Ar^{9+}

	K_{α_1} [eV]	K_{α_2} [eV]
P. Palmeri *et al.*[52] Theo.	2958.70	2956.60
P. Palmeri *et al.*[52] Theo.	2957.90	2955.90
P. Palmeri *et al.*[52] Theo.	2957.68	2955.56
NIST[20] Exp.	2957.68	2955.56

Table 2.9.: Different experimental and theoretical values for K_{α_1} and K_{α_2} [eV].
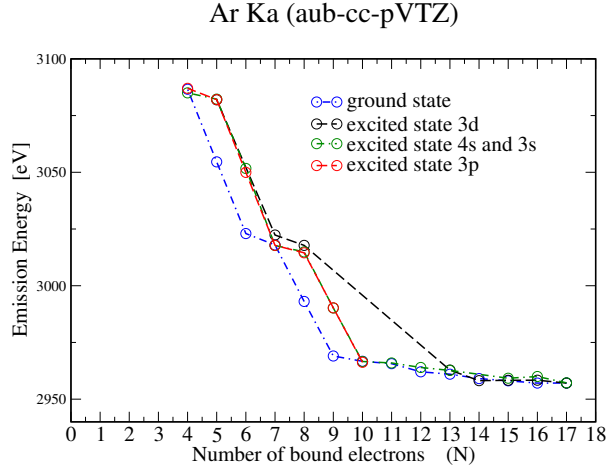
Figure 2.11.: Ar K_α emission energies calculating excited states of 3d (black curve) excited states of 4s and 3s (green curve), excited states of 3p (red curve) and ground states of $Ar^{(18-N)+}$ ions (blue curve) by G03.

to Ar^{14+} in the L-shell. The shift of Ar emission line (blue line shift) is due to ionization [27]. The Ar^+ to Ar^{9+} have similar emission energies. In Fig 2.11 shows the charge state from 1+ to 8+ in M shell have closely emission between 2950 eV to 2970 eV and the charge state from 9+ to 14+ have a larger energy distance in L shell. We consider also 3p, 4s and 3d excited state energies in our model. These excited states have the different configurations the the outside shell. In chapter 3 we need more detailed using different configurations in the screening potential with perturbation Hamiltonian.

3. Line Shift due to Plasma Environment

3.1. Green Function Approach to Dense Plasmas

A systematic many body approach would give the observed line spectra, see [8]. In this chapter we will introduce the thermodynamic Green function with some diagram methods using the operators of second quantization for describing the many-particle systems such as the Coulomb system. The Green function is an efficient method for the description of interacting many body systems. For instance, a rigorous approach to Debye screening is possible holding in dilute classical Coulomb systems [38].

The state of a plasma is determined by the complete set of observables $c_1 \cdots c_N$ in the N particle system. Here $c_1 \cdots c_N$ are the complete single particle observables that from a complete basis in the Hilbert space

$$|c_1 \cdots c_N\rangle. \tag{3.1}$$

In Eq. (3.1), c_1 includes, for instance, position parameter $\mathbf{r_1}$, the z component of spin s_1^z or the momentum parameter $\mathbf{p_1}$ on the c_1 plasma particle. In the following, the single particle c_1 would be an electron or an ion in the plasma. The N particles are indistinguishable particles in the quantum system. The spin statistics postulate [18] introduce a space of states of Fermi antisymmetric particles $|c_1 \cdots c_N\rangle^-$ and a space of the states of Bose symmetric particles $|c_1 \cdots c_N\rangle^+$ describing each identical particles. The quantum states can be given by Eq. (3.1)

$$|c_1 \cdots c_N\rangle^\pm = \frac{1}{\sqrt{N!}} a^\dagger(c_1) \cdots a^\dagger(c_N)|0\rangle. \tag{3.2}$$

In Eq. (3.2), $|0\rangle$ is the vacuum state (no particles), $a^\dagger(c)$ is a creation operator and $a(c)$ is an annihilation operator . The N particles completeness relation in the Fock space is

$$\sum_N \int dc_1 \cdots dc_N |c_1 \cdots c_N\rangle^\pm \langle c_N \cdots c_1| = 1. \tag{3.3}$$

The creation and annihilation operators satisfy the commutation rules of commutators

3. Line Shift due to Plasma Environment

for Boson particles and anti-commutators for Fermi particles,

$$\left[a(c), a(c')\right]_{\mp} = 0 \tag{3.4}$$

$$\left[a^{\dagger}(c), a^{\dagger}(c')\right]_{\mp} = 0 \tag{3.5}$$

$$\left[a(c), a^{\dagger}(c')\right]_{\mp} = \delta(c - c'). \tag{3.6}$$

In these commutation rules Eq. (3.4), the brackets $[...]_-$ denotes commutator and $[...]_+$ denotes anti-commutator.

We consider electro-neutral plasmas

$$e \sum_{m=0}^{Z} m n_m - e n_e = 0. \tag{3.7}$$

Eq. (3.7) n_m is the particle density of the m-fold charged ions, the charge is me. An unperturbed plasma has no external field. We use the second quantization to describe the quantum system. A single-particle Hamiltonian is shown in Eq. (2.3). In the beginning we set interaction potential $V = 0$ and kinetic energy equals $E_k = \frac{\hbar^2 k^2}{2m}$ considering a single particle contribution. The single-particle Hamiltonian is [6]:

$$\mathrm{H}^{(1)} = \sum_{k} E_k c_k^+ c_k. \tag{3.8}$$

In Eq. (3.8) describes the annihilation operator c_k, creation operator c_k^+ and the occupation number are described as $n_k = c_k^+ c_k$. In many electron system, we use fermionic operator a with a^+. The Fermionic particle number is

$$N = \sum_{k} \langle a_k^+ a_k \rangle = \sum_{k} f_k \tag{3.9}$$

with ideal Fermi distribution

$$f_k = \frac{1}{e^{\beta(E_k - \mu)} + 1}. \tag{3.10}$$

The anti-commutators are

$$\{a_k, a_{k'}^+\}_+ = a_k a_{k'}^+ + a_{k'}^+ a_k = \delta_{kk'} \tag{3.11}$$

$$\{a_k^+, a_{k'}^+\}_+ = \{a_k, a_{k'}\}_+ = 0. \tag{3.12}$$

In an ideal Bose gas system the Bosonic particle number N_B is

$$N_B = \sum_{k} \langle b_k^+ b_k \rangle = \sum_{k} g_k. \tag{3.13}$$

The commutators are

$$\left[b_k, b_{k'}^+\right]_- = b_k b_{k'}^+ - b_{k'}^+ b_k = \delta_{kk'} \tag{3.14}$$

$$\left[b_k^+, b_{k'}^+\right]_- = [b_k, b_{k'}]_- = 0. \tag{3.15}$$

The ideal Bose distribution is given by

$$g_k = \frac{1}{e^{\beta(E_k - \mu)} - 1}. \tag{3.16}$$

The single Fermi particle average has four different forms;

$$\langle a_i^+ a_j^+ \rangle = 0 \tag{3.17}$$

$$\langle a_i a_j \rangle = 0 \tag{3.18}$$

$$\langle a_i^+ a_j \rangle = \delta_{ij} \frac{1}{e^{\beta(E_i - \mu)} + 1} = \delta_{ij} f_i \tag{3.19}$$

$$\langle a_i a_j^+ \rangle = \delta_{ij} \frac{1}{e^{-\beta(E_i - \mu)} + 1} = \delta_{ij}(1 - f_i). \tag{3.20}$$

In dense plasma system, the total Hamiltonian consists of a diagonal single particle operator $H^{(1)}$, two particle operator $H^{(2)}$, $\cdots$ with more particles contribution.

$$H = H^{(1)} + H^{(2)} + \cdots \tag{3.21}$$

$$= \sum_k E_k c_k^+ c_k + \frac{1}{2} \sum_{k_1 k_2, k_1' k_2'} V_{k_1 k_2, k_1' k_2'} c_{k_1}^+ c_{k_2}^+ c_{k_2'} c_{k_1'} + \cdots . \tag{3.22}$$

The mean value observable A in the state $|\psi\rangle$ at a system in the quantum statistics can be described with density operator ρ. For pure ensemble, the density operator is given by

$$\rho = |\psi\rangle\langle\psi| \tag{3.23}$$

and the mean value of observation

$$\langle A \rangle = \langle \psi | A | \psi \rangle = \mathrm{Tr}(\rho A). \tag{3.24}$$

At mixed ensemble the density operator is

$$\rho = \sum_i p_i |\psi_i\rangle\langle\psi_i| \tag{3.25}$$

with $\sum_i p_i = 1$ (sum all of the probability) and the mean value of an observable is

$$\langle A \rangle = \sum_i p_i \langle \psi_i | A | \psi_i \rangle = \mathrm{Tr}(\rho A). \tag{3.26}$$

The total energy of the ions consists of kinetic energy and potential energy: $E = E_k + E_n$ [3]. Considering the grand canonical ensemble at energy and particle exchange interaction system. The grand canonical partition function is given by

$$\sigma_G(T, V, \mu) = \mathrm{Tr}\, e^{-(H - \mu N)/k_B T}. \tag{3.27}$$

We could use the pressure and partition function relation in the thermodynamic system

$$p(\mu, T) = \frac{k_B T}{V} \ln \sigma_G(T, V, \mu). \tag{3.28}$$

3. Line Shift due to Plasma Environment

The Eq. (3.28) describes the pressure. The density is

$$n(\mu, T) = \frac{\partial}{\partial \mu} p(\mu, T).$$ (3.29)

The density matrix of the grand canonical ensemble is

$$\rho_G = \frac{e^{-(H-\mu N)/(k_B T)}}{\sigma_G}$$ (3.30)

$$= \frac{e^{-\beta(H-\mu N)}}{\mathrm{Tr} e^{-\beta(H-\mu N)}}.$$ (3.31)

The entropy of the grand canonical ensemble is a function of temperature

$$S_G = -k_B \langle \log \rho_G \rangle.$$ (3.32)

[26]. In the more general many particles case, the entropy can be decomposed

$$S = S^{(0)} + S^{(1)} + S^{(2)} + ...$$ (3.33)

$$= \ln Z + \sum_k s_k^{(1)} c_k^+ c_k + \sum_{k_1 k_2, k_1' k_2'} s_{k_1 k_2, k_1' k_2'}^{(2)} c_{k_1}^+ c_{k_2}^+ c_{k_2'} c_{k_1'} + ...$$ (3.34)

A charged particle interact with a large number of surrounding charged particles due to screening in the plasma environment. For considering real quantum gases with an interaction potential V, the method reduces to ideal quantum gases with a perturbation theory. In time-dependent perturbation theory introduces the Dyson series with a time-ordering operator $T[\cdots]$ and $\tau \geq \tau_1 \geq \tau_2 \geq \cdots$.

$$e^{A+B} = e^A + \int_0^1 d\tau e^{(1-\tau)A} B e^{\tau A} + \int_0^1 d\tau \int_0^\tau d\tau_1 e^{(1-\tau)A} B e^{(\tau-\tau_1)A} B e^{\tau_1 A} + \cdots.$$ (3.35)

In two particles fermion system, there are total entropy operator $S = S^{(0)} + S^{(1)} + S^{(2)}$, The one particle contribution is

$$S^{(1)} = \beta \sum_1 (E_1 - \mu) a_1^+ a_1.$$ (3.36)

The two particles Coulomb potential is given by

$$S^{(2)} = \frac{1}{2} \beta \sum_{12, 1'2'} V(12, 1'2') a_1^+ a_2^+ a_{2'} a_{1'}.$$ (3.37)

Using interaction picture perturbation theory is

$$A(\tau) = U_I(0, \tau) A_I(\tau) U_I(\tau, 0)$$ (3.38)

with time evolution operator

$$U_I(\tau, \tau') = e^{S^{(1)}\tau} e^{-S(\tau-\tau')} e^{S^{(1)}\tau'}.$$ (3.39)

The evolution operators are

$$U_I(0, \tau) = e^{S^{(1)}0} e^{S\tau} e^{-S^{(1)}\tau} \tag{3.40}$$

$$U_I(\tau, 0) = e^{S^{(1)}\tau} e^{-S\tau} e^{-S^{(1)}0}. \tag{3.41}$$

Then

$$A_I(\tau) = e^{(S^{(0)}+S^{(1)})\tau} A(0) e^{-(S^{(0)}+S^{(1)})\tau} = e^{S^{(1)}\tau} A(0) e^{-S^{(1)}\tau}. \tag{3.42}$$

The complete evolution is

$$A(\tau) = e^{S\tau} A(0) e^{-S\tau}. \tag{3.43}$$

Eq. (3.39) can be rewritten with the time ordering T

$$U_I(\tau, \tau') = \sum_{n=0}^{\infty} (-1)^n \frac{1}{n!} \int_{\tau'}^{\tau} d\tau_1 \cdots \int_{\tau'}^{\tau} d\tau_n T \left[S^{(2)}(\tau_1) \cdots S^{(2)}(\tau_n) \right]. \tag{3.44}$$

The thermodynamic Green function is defined as

$$G_1(1\tau, 1'\tau') = -\text{Tr}\{\rho T \left[a_1(\tau) a_1^+(\tau') \right]\} \tag{3.45}$$

using Eq. (3.33) with $\rho = \frac{e^{-(S^{(1)}+S^{(2)})}}{Tr\{e^{-(S^{(1)}+S^{(2)})}\}}$.

The free single-particle Green function is given by

$$G_1^0(11', iz_\nu) = \frac{\delta_{11'}}{iz_\nu - (E_1 - \mu)}. \tag{3.46}$$

In Eq. (3.46), the $\delta_{11'}$ (meaning $\delta_{p_1 s_1 c_1 iz_{\nu 1}, p_{1'} s_{1'} c_{1'} iz_{\nu 1'}}$) with p_1 is the momenta of the

$$G_1^0(11', iz_\nu)$$

Figure 3.1.: Single particle Green function.

incoming particle, $p_{1'}$ is outgoing particle, s_1 and c_1 their respective spin and species. The term $\delta(\omega - E_1(p))$ has $E_1(\mathbf{p})$ the single-particle energies.

$$z_\nu = \frac{\pi \nu}{\beta}, \nu = \pm 1, \pm 3, \pm 5 \cdots \text{for Fermions}, \nu = 0, \pm 2, \pm 4 \cdots \text{for Bosons}, \tag{3.47}$$

with the Matsubara frequencies z_ν. We define $\epsilon_{\mathbf{k}} = E_1 - \mu$ and Eq. (3.46) is described more simple form $G_1^0(\mathbf{k}, iz_\mu) = \frac{1}{iz_\nu - \epsilon_{\mathbf{k}}}$. The Feynman free single-particle Green function see Fig. 3.1.

The free two-particle Green function can describe two-particle bound states for the Feynman diagram of two particles, see Fig. 3.2 [39].
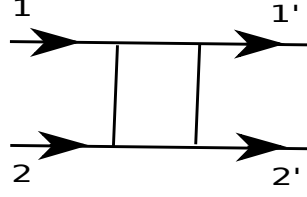
Figure 3.2.: Two particle Green function.

In Eq. (3.37) the Coulomb interaction potential reads in Fourier space

$$V(\mathbf{q}) = \frac{1}{\Omega} \int d^3 r e^{i\mathbf{q}\mathbf{r}} V(\mathbf{r}). \tag{3.48}$$

In Eq. (3.48) Ω is volume. Coulomb potential is represented as a Feynman diagram by a broken line, see Fig. 3.3. The charge is the vertex that connects the interaction line with the free propagator.
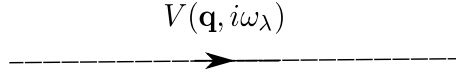
$$V(\mathbf{q}, i\omega_\lambda)$$

Figure 3.3.: Coulomb potential Green function.

In lowest (first) order with respect to the Coulomb interaction we obtain the Hartree Fock approximation see in Fig. 3.4a Hartree diagram. The Hartree contribution [6] could be written

$$\text{Hartree} = \frac{1}{\beta} \left(\frac{1}{2\pi} \right)^3 (2s+1) \sum_{z_\mu} \int d^3\mathbf{k}' G_1^0(\mathbf{k}, iz_\nu) \cdot G_1^0(\mathbf{k}', iz_\mu) \cdot G_1^0(\mathbf{k}, iz_\nu) \cdot V(\mathbf{0}, \mathbf{0})$$

$$\tag{3.49}$$

$$= \frac{1}{iz_\nu - \epsilon_k} \cdot (2s+1) \int \frac{d^3\mathbf{k}'}{(2\pi)^3} f(\epsilon_{k'}) \cdot V(\mathbf{0}) \cdot \frac{1}{iz_\nu - \epsilon_k}. \tag{3.50}$$

In Fig. (3.4b) is Fock diagram. The Fock contribution [6] could be written

$$\text{Fock} = -\frac{1}{\beta} \left(\frac{1}{2\pi} \right)^3 \sum_{z_\mu} \int d^3\mathbf{k}' G_1^0(\mathbf{k}, iz_\nu) \cdot G_1^0(\mathbf{k}', iz_\mu) \cdot G_1^0(\mathbf{k}, iz_\nu) \cdot V(\mathbf{k} - \mathbf{k}', i\omega_\lambda)$$

$$\tag{3.51}$$

$$= -\frac{1}{iz_\nu - \epsilon_k} \int \frac{d^3\mathbf{k}'}{(2\pi)^3} f(\epsilon_{k'}) \cdot V(\mathbf{k} - \mathbf{k}') \cdot \frac{1}{iz_\nu - \epsilon_k}. \tag{3.52}$$

The Hartree Fock self energy is shown in Fig. 3.5

$$\Sigma_1^{\text{HF}}(\mathbf{k}) = \int \frac{d^3\mathbf{k}'}{(2\pi)^3} \left((2s+1)V(\mathbf{0}) - V(\mathbf{k} - \mathbf{k}') \right) f(\epsilon_k'). \tag{3.53}$$

The Hartree-Fock approximation describes the motion of particles ignoring collisions in the mean field. The Hartree-Fock approximation is the first order contribution to the Montroll-Ward approximation given in the section 3.4.
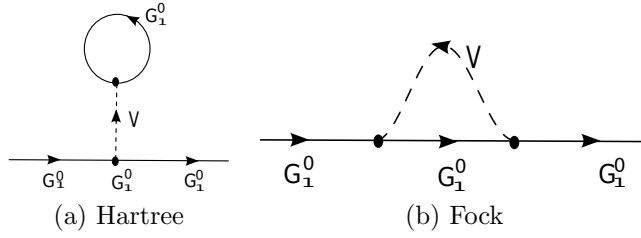
(a) Hartree   (b) Fock

Figure 3.4.: Feynman diagrams corresponding to Hartree Fock approximation.
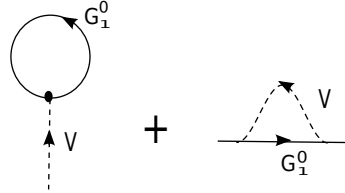

Figure 3.5.: Hartree Fock self energy expressed by Feynman diagrams.

3.2. Dynamical Screening and Quasiparticle Concept

The hydrogen plasma is described by Eq. (1.16) and Eq. (1.17). Now we consider many-particle effect in Si and Ar. The chemical potential can be also written

$$\begin{aligned} \mu_c &= \mu_c^{id} + \mu_c^{int} \\ &= k_B T \ln \left(\frac{n_c \Lambda_c^3}{g_c} \right) + \Delta_c. \end{aligned} \tag{3.54}$$

μ_c^{id} is the ideal degenerate chemical potential and Δ_c considers the interaction with the other plasma particles. In lowest order it is given by the Hartree-Fock self-energy with screened interaction. The rigid shift approximation (Zimmermann 1988) is described the interaction screening potential Δ_c equal to the quasi particle shift $\Delta(\mathbf{p}, \mu)$. We combine the free particle part and the bound particle part. The free particle part is given by the Fermi distribution Eq. (3.10). The quasiparticle distribution could be described by

$$f_c(\mathbf{p}) = \frac{1}{e^{\beta(\mathbf{p}^2/2m + \Delta(\mathbf{p},\mu) - \mu)} \pm 1}. \tag{3.55}$$

In Eq. (3.55), $\Delta(\mathbf{p}, \mu)$ is quasi-particle shift. The number density in thermodynamic equilibrium is defined by

$$n(\mu, T) = (2s + 1) \int \frac{d\mathbf{p}}{(2\pi)^3} \frac{1}{e^{\beta(\mathbf{p}^2/2m + \Delta(\mathbf{p},\mu) - \mu)} \pm 1}. \tag{3.56}$$

The pressure of the plasma is obtained by

$$p(\mu, T) = \int_{-\infty}^{\mu} n(\mu', T) d\mu'. \tag{3.57}$$

Using Eq. (3.55) into Eq. (3.57) we get the equation of state for the pressure in free quasiparticle approximation

$$p(\mu, T) = k_{\mathrm{B}} T \int \frac{d\mathbf{p}}{(2\pi)^3} \ln\left(1 \pm e^{-\beta(p^2/2m + \Delta(\mathbf{p},\mu) - \mu)}\right). \tag{3.58}$$

Now we consider the single particle partition function. In general, the particles (ions) have internal states of motions. The internal partition function associated with internal states is σ_c^{int} (statistical weight). The internal partition function is described with different configurations on excited states, bound state and their degeneration factors.

$$\mu_c = k_B T \ln\left(\frac{n_c \Lambda_c^3}{\sigma_c^{int}}\right). \tag{3.59}$$

Assuming $\Delta = \Delta(\mathbf{p}, \mu)$ with the quasi-particle shifts $\Delta(\mathbf{p}, \mu)$, the single particle energy is $E(\mathbf{p}) = \frac{p^2}{2m} + \Delta$. In the rigid shift approximation, the chemical potential equals to the ideal chemical potential μ^{id} with the interaction part of chemical potential μ^{int}. The shift Δ means the interaction part μ^{int} of the chemical potential [18]. For charged plasma particles of species c, the quasi-particle shift has the value $\Delta_c = -\frac{\kappa_c e_c^2}{2}$. The full propagator including self energy is described by $G_1(1, iz_\nu) = \frac{1}{iz_\nu - \epsilon_1 - \Sigma_1(1, iz_\nu)}$, see Fig. 3.6. $\epsilon_\mathbf{k} = \frac{\hbar^2 \mathbf{k}^2}{2m} - \mu$. The self energy is one test particle located at $\mathbf{r} = \mathbf{v_0} t$ and interacting with of all particles of the surrounding plasma. The self energy is also the potential energy of test particle and contains the screening effect in the plasma, as lowest (Montroll-Ward) approximation.
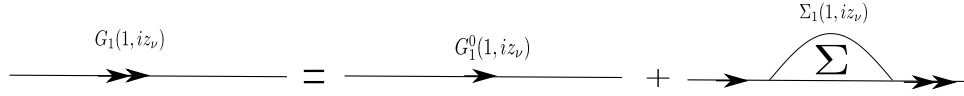

Figure 3.6.: Full propagator including self energy Feyman picture.

3.3. Ion-Sphere-Model

We consider here only Si in different ionization states m. A plasma consists of ions, electrons and photons. The electrons are divided to bound electrons, bound to a single ion, and free electrons moving freely in the plasma. We consider homogeneous plasmas. The ions of charge number $m = 0, 1, \cdots, Z$ (charge em) have the particle number density n_m. We denote m the charge of the ion, neutral $m = 0$ and $m = Z$ fully ionized. [3].

$$n_c = \sum_{m=0}^{Z} n_m. \tag{3.60}$$

The requirement of charge neutrality in the plasma, the electron density n_e is defined according to

$$n_e = \sum_{m=0}^{Z} m n_m. \tag{3.61}$$

The average charge state is denoted by $\bar{Z}$ and $\bar{Z} = \frac{n_e}{n_c}$. $\bar{Z}$ depends on the temperature and the density. Ion sphere with ion sphere radius R_c (also called Wigner-Seitz Radius), for every ion has the same average volume V_c defined

$$V_c = \frac{1}{n_c} = \frac{4\pi}{3}R_c^3. \tag{3.62}$$

We give some special relations with Fermi-Dirac distribution [3](Eliezer,1986;Landau and Lifshitz,1959)

$$f_p(p)dp = \frac{1}{\pi^2\hbar^3}\frac{p^2dp}{1 + \exp[(p^2/2m - \mu_e)/k_BT_e]} \tag{3.63}$$

and energy distributions

$$f_E(E)dE = \frac{\sqrt{2}}{\pi^2}\frac{(mc^2)^{3/2}}{(\hbar c)^3}\frac{E^{1/2}dE}{1 + \exp[(E - \mu)/k_BT_e]}. \tag{3.64}$$

We can introduce the Fermi integrals,

$$F_\nu(x) = \frac{1}{\Gamma(\nu + 1)}\int_0^\infty \frac{t^\nu}{e^{t-\nu} + 1}dt. \tag{3.65}$$

Some properties in Fermi integrals, $\Gamma(\nu + 1) = \nu\Gamma(\nu)$, $\Gamma(1/2) = \sqrt{\pi}$ and

$$\frac{d}{dx}F_\nu(x) = F_{\nu-1}(x). \tag{3.66}$$

with $x = e^{\mu_e/k_BT}$. If $x \ll 1$, $x = e^{\mu_e/k_BT}$ we find the lowest approximation $F_\nu(x) = x$. In particular, we get

$$\frac{n_e\lambda_e^3}{2} = \frac{2}{\sqrt{\pi}}\int_0^\infty \frac{\sqrt{t}}{e^{t-\mu_e/(k_BT_e)} + 1}dt. \tag{3.67}$$

The electron temperature T_e, chemical potential of electrons μ_e and total electron density is,

$$n_e = 2\frac{(mc^2T_e)^{3/2}}{\sqrt{2}\pi^2(\hbar c)^3}F_{1/2}(\frac{\mu_e}{T_e}). \tag{3.68}$$

In the low temperature limit $T_e \to 0$, the momentum distribution reduces to

$$f_p(p)dp = \begin{cases} 0, & \text{wenn } p^2/2m > \mu \\ p^2dp/(\pi^2\hbar^3), & \text{wenn } p^2/2m < \mu \end{cases} \tag{3.69}$$

the energy distribution reduces to

$$f_E(E)dE = \begin{cases} 0, & \text{wenn } E > \mu \\ (\sqrt{2}/\pi^2)[(mc^2)^{3/2}/(\hbar c)^3]E^{1/2}dE, & \text{wenn } E < \mu \end{cases} \tag{3.70}$$

and the lower temperature limit of the chemical potential becomes

$$\mu = \frac{(\hbar c)^2}{2mc^2}(3\pi^2 n_e)^{2/3}. \tag{3.71}$$

In the limit $\mu \to -\infty$ is the Fermi-Dirac distribution or the Boltzmann-Maxwell distribution.

The time scale on the atomic scale in hot plasmas is connected to the plasma frequency (Spitzer, 1962), ($m_e \ll m_i$ fully ionized ions with charge eZ)

$$\omega = \left[\frac{4\pi e^2 n_e}{m_e}\left(1 + Z\frac{m_e}{m_i}\right)\right]^{1/2} \approx \left(\frac{4\pi e^2 n_e}{m_e}\right)^{1/2}. \tag{3.72}$$

3.3.1. The Debye-Hückel Theory

The Debye-Hückel theory [3] describes the screening of the nuclear electrostatic potential by the bound electrons and the free electrons. The screened potential of a m-fold charged ion (charge em) with a screening factor $S(r)$ from the Coulomb potential is defined by

$$V_m(r) = \frac{me}{r}S(r) \tag{3.73}$$

The screening factor $S(r)$ means the modification of the Coulomb potential. In the limit cases, $S(r \to 0) = 1$ and $S(r \to \infty) = 0$, we use the Boltzmann statistical distribution Eq. (3.55) for the ion density

$$n_m(\mathbf{r}) = n_m \exp\left(-\frac{emV(\mathbf{r})}{k_B T}\right) \tag{3.74}$$

and the electron density,

$$n_e(\mathbf{r}) = n_e \exp\left(\frac{eV(\mathbf{r})}{k_B T}\right). \tag{3.75}$$

The Poisson equation for zero charge density around an external electrical charge $Z_0 e$ introduced into the plasma is given by

$$\nabla^2 V(\mathbf{r}) = 0. \tag{3.76}$$

Consider a structureless pointlike ion with nuclear charge $m_0 e$ at $r = 0$ in the plasma with finite charge density. The Poisson equation that describes the electric potential around the ion is,

$$\nabla^2 V(\mathbf{r}) = -4\pi e\left(\sum_{m_0}^{N} mn_m(\mathbf{r}) - n_e(\mathbf{r})\right). \tag{3.77}$$

In the parentheses including the first term from the ion density and the second term from the electron density. When satisfying the condition $\frac{eV(\mathbf{r})}{k_B T} \ll 1$, the Eq. (3.75) can be expanded with respect to $\frac{eV}{k_B T}$ in a Taylor series, to get an approximate from keeping first order term only,

$$\nabla^2 V(\mathbf{r}) = 4\pi e \left[\sum_{m=0}^{Z} m n_m \left(1 - \frac{emV(\mathbf{r})}{k_B T} \right) - n_e \left(1 + \frac{eV(\mathbf{r})}{k_B T} \right) \right]$$

$$= V(\mathbf{r}) \frac{4\pi e^2}{k_B T} \left[\sum_{m=0}^{Z} m^2 n_m + n_e \right]. \tag{3.78}$$

We define the Debye screening length by D ($\kappa = \frac{1}{D}$)

$$D = \sqrt{\frac{k_B T}{4\pi e^2} \frac{1}{\left[\sum_{m=0}^{Z} m^2 n_m + n_e \right]}}. \tag{3.79}$$

The Poisson equation can be reduced to

$$\nabla^2 V(\mathbf{r}) = \frac{V(\mathbf{r})}{D^2}. \tag{3.80}$$

We calculate the homogeneous isotropic steady state and we find plasma independent of time of average electron density and average ion density, do not have a preferential direction and only depend on the radius r. Assume an ion is located at $r = 0$ using spherical symmetry isotropic and replacing $V(\mathbf{r})$ by screening factor $S(r) = rV(\mathbf{r})/(Ze)$. The Poisson operator is.

$$\nabla^2 V(\mathbf{r}) = \frac{1}{r^2} \frac{\partial}{\partial r} \left(r^2 \frac{\partial V}{\partial r} \right)$$

$$\frac{d^2 S}{dr^2} = \frac{1}{D^2} S(r) \tag{3.81}$$

with boundary conditions at $r = 0$ with $S(r = 0) = 1$ and $r \to \infty$ solving the $S(r)$ is,

$$S(r) = e^{-r/D}. \tag{3.82}$$

Thus the Debye-Hückel potential results:

$$V(r) = \frac{Z_0 e}{4\pi \epsilon_0 r} e^{-r/D}. \tag{3.83}$$

The Debye sphere is defined as the sphere around the central ion with radius is D. D depends on the ion density (ensemble over charge state n_m at the average partial density) and electron density. Eq. (3.83) can be written as potential of an electron (SI units)

$$U(r) = -\frac{Z_{\text{eff}} e^2}{4\pi \epsilon_0 r} e^{-\kappa r}, \tag{3.84}$$

$$\kappa = \sqrt{\frac{n_e e^2}{\epsilon_0 k_B T}} \tag{3.85}$$

with $D = \frac{1}{\kappa}$. Then we get

$$\Delta E^{(1)} = \left\langle \phi \Big| - \frac{Z_{\text{eff}} e^2 \frac{1}{2}\kappa^2}{4\pi\epsilon_0 r} \Big| \phi \right\rangle. \tag{3.86}$$

Using the self consistent RHF wave functions calculate the K_α emission energy using the shift of final state (ϕ_{2p}) described by

$$\begin{aligned}
\Delta E_{2p} &= \langle \phi_{2p} | - \frac{Z_{\text{eff}} e^2 \frac{1}{2}\kappa^2}{4\pi\epsilon_0 r} | \phi_{2p} \rangle \\
&= -\frac{Z_{\text{eff}} e^2 \kappa^2}{8\pi\epsilon_0} \int_0^\infty dr\, r^3 |R_{2p}(r)|^2.
\end{aligned} \tag{3.87}$$

The energy shift of the initial state (ϕ_{1s}) is given by

$$\begin{aligned}
\Delta E_{1s} &= \langle \phi_{1s} | - \frac{Z_{\text{eff}} e^2 \frac{1}{2}\kappa^2}{4\pi\epsilon_0 r} | \phi_{1s} \rangle \\
&= -\frac{Z_{\text{eff}} e^2 \kappa^2}{8\pi\epsilon_0} \int_0^\infty dr\, r^3 |R_{1s}(r)|^2.
\end{aligned} \tag{3.88}$$

The K_α emission shift energy can be written as

$$\Delta E_{2p->1s}(k_B T, n_e) = -\frac{Z_{\text{eff}} e^2 \kappa^2}{8\pi\epsilon_0} \left(\int_0^\infty dr\, r^3 |R_{2p}(r)|^2 - \int_0^\infty dr\, r^3 |R_{1s}(r)|^2 \right) \tag{3.89}$$

with screening potential effect.

3.3.2. Thomas-Fermi Model

The Thomas-Fermi mode (TF)[3] has been developed mainly for zero temperature in statistical description. The TF model describes in our approach the ionic potential in hot plasmas at the high-Z material. The ion sphere is confined to a nucleus of charge Z located at $r = 0$, and Z electrons include bound electrons and free electrons. The total potential is zero on and beyond the boundaries of the ion sphere of Thomas-Fermi model. The Poisson equation is,

$$\begin{aligned}
\nabla^2 V(\mathbf{r}) &= -4\pi e\left[Z\delta(\mathbf{r}) - n_e(\mathbf{r}) \right] \\
&= 4\pi e n_{\text{free}}(r) + 4\pi n_{\text{bound}} - 4\pi Z e\delta(r).
\end{aligned} \tag{3.90}$$

We solve the nuclear part $\nabla^2 V_n(\mathbf{r}) = -4\pi e Z\delta(\mathbf{r})$ and we use the Dirac delta function

$$\nabla^2 \left(\frac{1}{r} \right) = -4\pi\delta(\mathbf{r}). \tag{3.91}$$

Directly we get the nuclear potential

$$V_n(\mathbf{r}) = \frac{Ze}{r}. \tag{3.92}$$

We solve the electron part $\nabla^2 V_e(\mathbf{r}) = 4\pi e n_e(\mathbf{r})$. We use Helmholtz's Theorem $\nabla^2 V(\mathbf{r}) = -k(\mathbf{r})$ with $V(\mathbf{r}) = \frac{1}{4\pi} \int \frac{k(\mathbf{r})}{|\mathbf{r}-\mathbf{r}'|} d^3 r'$. The electron potential is given by

$$V_e(\mathbf{r}) = -\int_V \frac{e n_e(\mathbf{r})}{|\mathbf{r} - \mathbf{r}'|} d^3 r'. \tag{3.93}$$

Assuming spherical symmetry around the nucleus reduces the $n_e(\mathbf{r}) = n_e(r)$ isotropic. The denominator is expanded to Legendre Polynomials (Abramowitz and Stegun, 1965)

$$\frac{1}{|\mathbf{r} - \mathbf{r}'|} = \sum_{k=0}^{\infty} \frac{r_<^k}{r_>^{k+1}} P_k(\cos\theta). \tag{3.94}$$

The $r_<$ is the smaller of r and r'. The $r_>$ is the larger of r and r'. The electron contribution is written by

$$V_e(r) = -e \sum_{k=0}^{\infty} \int_0^\infty \int_0^\pi \int_0^{2\pi} d\phi \sin\theta d\theta r'^2 dr' n_e(r') \frac{r_<^k}{r_>^{k+1}} P_k(\cos\theta). \tag{3.95}$$

We use the orthogonality conditions of the Legendre polynomials with $P_0(x)=1$,

$$\begin{aligned}
\int_0^\pi d\theta \sin\theta P_k(\cos\theta) &= \int_{-1}^1 dx P_k(x) P_0(x) \\
&= \frac{2}{2k+1} \delta_{k,0} \\
&= 2\delta_{k,0}.
\end{aligned} \tag{3.96}$$

The electron potential is reduced to

$$\begin{aligned}
V_e(r) &= -2\pi e \sum_{k=0}^{\infty} 2\delta_{k,0} \int_0^\infty r'^2 dr' n_e(r') \frac{r_<^k}{r_>^{k+1}} \\
&= -4\pi e \int_0^\infty n_e(r') \frac{r'^2 dr'}{r_>} \\
&= -4\pi e \left(\frac{1}{r} \int_0^r n_e(r') r'^2 dr' + \int_r^R n_e(r') r' dr' \right).
\end{aligned} \tag{3.97}$$

Using boundary condition of ion sphere at $r = R$ on ion sphere. We assume the charge neutrality requirement

$$Z = \int_0^R n_e(r, \mu) d^3 r. \tag{3.98}$$

The electron potential turns out $V_e(R) = -\frac{Ze}{R}$. The nuclear potential is at $r = R$ is $V_n(R) = \frac{Ze}{R}$. The total potential vanishes on the ion sphere boundaries

$$V(R) = V_n(R) + V_e(R) = 0. \tag{3.99}$$

3. Line Shift due to Plasma Environment

The Fermi-Dirac electron momentum distribution in a plasma with a local electric micro-fieldgiven by V_r is given by

$$f_e(r,p)dp = \frac{1}{\pi^2\hbar^3} \frac{p^2 dp}{1 + e^{[p^2/2m - eV(r) - \mu]/k_BT}} \tag{3.100}$$

Integrating over the momenta in Fermi-Dirac distribution we get the electron density

$$n_e(r) = \int dp f_e(r,p) \tag{3.101}$$

$$= \frac{(2mk_BT_e)^{3/2}}{2\pi^2\hbar^3} \int_0^\infty \frac{x^{1/2}dx}{1 + \exp(x-y)} \tag{3.102}$$

$$= \frac{2}{\lambda^3} F_{1/2}\left(\frac{eV(r)+\mu}{k_BT_e}\right) \tag{3.103}$$

with $x = \frac{p^2}{2mk_BT_e}$ and $y = \frac{eV(r)+\mu}{k_BT_e}$.

$$n_{ef}(r) = n_{e,f} = \frac{Z_f}{4\pi R_i^3/3} \tag{3.104}$$

$$V_{e,f} = -4\pi e n_{e,f}\left(\frac{1}{r}\int_0^r r'^2 dr' + \int_r^{R_i} r' dr'\right) \tag{3.105}$$

$$= -\frac{3eZ_f}{R_i^3}\left[\frac{1}{r}\left(\frac{r'^3}{3}\Big|_0^r + \frac{r'^2}{2}\Big|_r^{R_i}\right)\right] = \frac{-3eZ_f}{2R_i}\left[1 - \frac{1}{3}\left(\frac{r}{R_i}\right)^2\right] \tag{3.106}$$

$$= -\frac{eZ_f}{2R}\left(3 - \frac{r^2}{R^2}\right) \tag{3.107}$$

with the Wigner-Seitz radius R which is the boundary of the ion sphere.

The total Hamiltonian $H = H^0 + H'$ consists of the unperturbed Hamiltonian H^0 and the perturbation H' describes the plasma effect defined by

$$H' = -e[\phi(r) - \phi(r, n_e = 0)]. \tag{3.108}$$

Due to the screening of the free electrons surrounding the nucleus and the bound electrons the energy levels and hence the emission energies are shifted. Assuming φ_i is the wave function of the initial and φ_f describes the final level of the electron transition (2p → 1s), the spectral line shift can be calculated in first order perturbation theory as

$$\Delta E^{(1)} = <\varphi_i|H'|\varphi_i> - <\varphi_f|H'|\varphi_f>. \tag{3.109}$$

Here again we applied the Bunge wave functions given in section 2.2. As a result we obtain line shifts in dependence on both the plasma temperature k_BT and the average free electron density n_e. Keeping the total density fixed at the bulk value, we can relate k_BT and n_e according to the plasma composition as discussed in chapter 4.
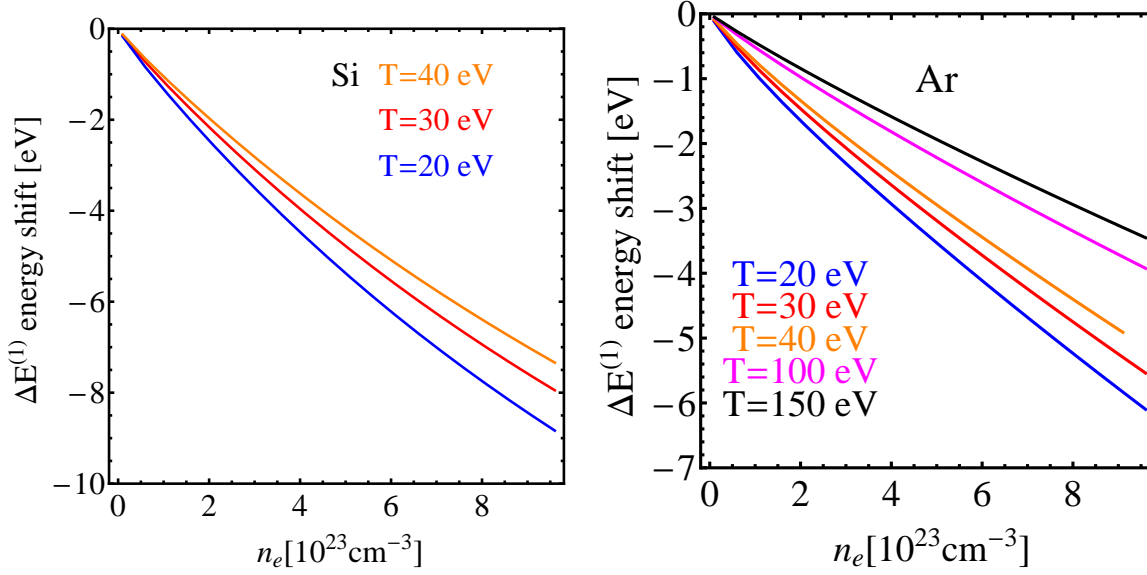
(a) Si isolated line shift in dependence of free electron density for the temperatures $T = 40$ eV (orange curve), $T = 30$ eV (red curve) and $T = 20$ eV (blue curve).

(b) Ar isolated line shift in dependence of free electron density for the temperatures $T = 150$ eV (black curve), $T = 100$ eV (pink curve), $T = 40$ eV (orange curve) and $T = 20$ eV (blue curve). For low temperatures the red shift is large.

Figure 3.7.: Red shift of K_α energies due to the plasma effect in dependence of average free electron density n_e and plasma temperature $k_B T$. Negative shift of emission energies due to the plasma effect.

Fig. 3.7 shows the Si and Ar spectral line shift in dependence of the free electron density for three different temperatures. The shift is negative, which means the emission energies are reduced due to the plasma environment. This effect is referred to as red plasma polarization shift and can be explained as follows: First, the free electrons screen the nucleus resulting in lower values of binding energies. As the bound state energies are negative, the energy levels are shifted to higher energies. Second, as the 1s level is localized closer to higher energies to the nucleus than 2p, it is more affected by the screening of the nucleus and thus experiences the larger shift. Finally, as the emission energy is given by the difference of the two involved levels the spectral line is red shifted to lower energies. The red shift increases with rising free electron density as the screening of the nucleus rises as well. However, the redshift decreases with rising plasma temperature. This is due to the fact that the self-consistently determined free electron density within the ion sphere is not constant but radially dependent. A screening cloud of free electrons is formed around the nucleus and the density dilutes for larger radii. However, the higher the temperature the more spatially extended ('smeared out') is this screening cloud and the less is the actual free electron density close to the nucleus, resulting in a lower red shift.

3.4. Random Phase Approximation and Montroll Ward Approximation

The quantum statistical approach to screening RPA (random phase approximation) [6] is the lowest order summand of the polarization function $\Pi(\mathbf{q}, iz_\mu)$ shown in Fig. 3.8.

$$\Pi(\mathbf{q}, iz_\mu) = -\frac{\Omega}{\beta}(2s+1)(-1) \int \frac{d^3p}{(2\pi)^3} \sum_{z_\lambda} \left(\frac{1}{iz_{\lambda-\epsilon_p}} \cdot \frac{1}{iz_\lambda - iz_\mu - \epsilon_{p-q}} \right). \qquad (3.110)$$
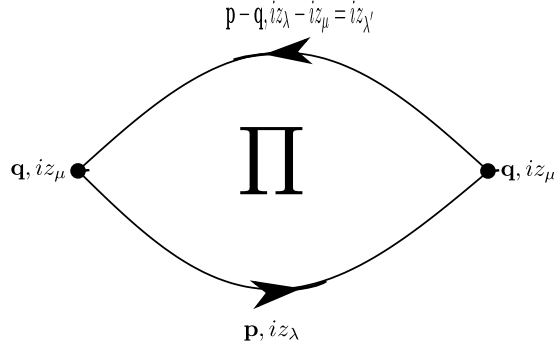

Figure 3.8.: Random phase approximation for the polarization function.

The single-particle energy is equal to kinetic energy in addition to the corresponding self-energy

$$E(\mathbf{p}) = \frac{p^2}{2m} + \Delta(\mathbf{p}). \qquad (3.111)$$

The screening equation is given from the single particle propagator to the self-energy and the polarization function $\Pi(\mathbf{q}, iz_\mu)$ is included all of irreducible diagrams. The screening potential is defined by

$$V_{ab}^s(\mathbf{q}, iz_\mu) = V_{ab}(\mathbf{q}) + \sum_{cd} V_{ac}(\mathbf{q})\Pi_{cd}(\mathbf{q}, iz_\mu)V_{db}^s(\mathbf{q}, iz_\mu). \qquad (3.112)$$

In the special case that Π is diagonal in the particle species. We have $\Pi_{cd}(q, iz_\mu) = \Pi_{cc}(q, iz_\mu)\delta_{cd}$. For the longitudinal dielectric function result is $\epsilon(q, iz_\mu) = 1 - \sum_c V_{cc}(q)\Pi_{cc}(q, iz_\mu)$. The screening potential can be reduced to

$$V_{ab}^s(\mathbf{q}, iz_\mu) = \frac{V_{ab}(q)}{\epsilon(q, iz_\mu)}. \qquad (3.113)$$

The frequency of the polarization function corresponds to even Matsubara frequencies and the polarization function has bosonic character. The polarization function is $\Pi(\mathbf{q}, iz_\mu)$. We consider the dielectric function only with in RPA approximation and take
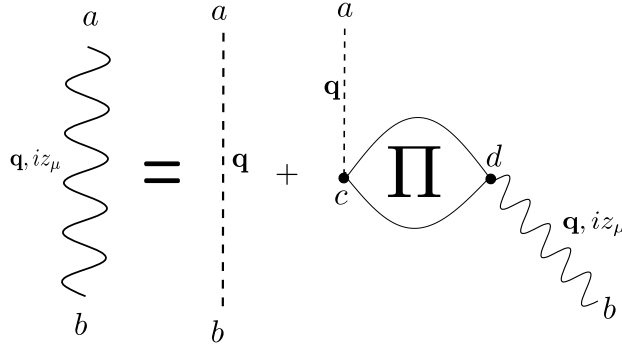
Figure 3.9.: Screening equation $V_{ab}^s(\mathbf{q}, iz_\mu)$.

$iz_\mu \to \hbar(\omega + i0)$ [6]. The RPA dielectric function is given by

$$\epsilon^{RPA}(q, \hbar\omega) = 1 - \sum_c V_{cc}(q)\Pi_{cc}^{RPA}(q, \hbar(\omega + i0)) \tag{3.114}$$

$$= 1 - \sum_c V_{cc}(q)(2s_c + 1)\Omega \int \frac{d^3p}{(2\pi)^3} \frac{f(\epsilon_{c,p-q}) - f(\epsilon_{c,p})}{\hbar(\omega + i0) + \epsilon_{c,p-q} - \epsilon_{c,p}}. \tag{3.115}$$

In the low density plasmas the Debye screening follows. In the case $T \to 0$ in the strongly degenerate plasmas can be obtained by the Thomas-Fermi approximation.

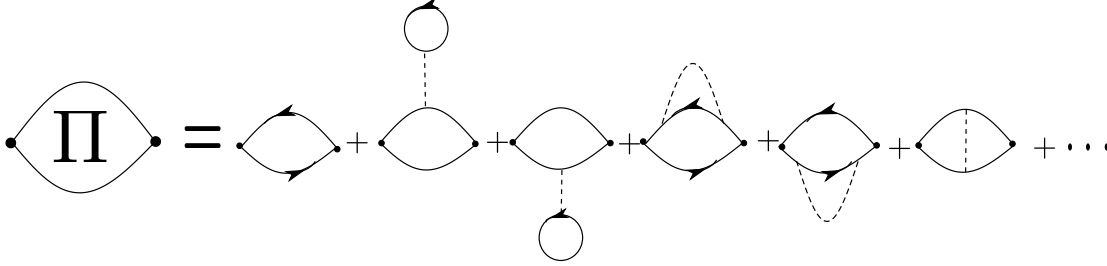We need this term for later Montroll Ward approximation.

Figure 3.10.: Screening equation $\Pi(\mathbf{q}, iz_\mu)$.

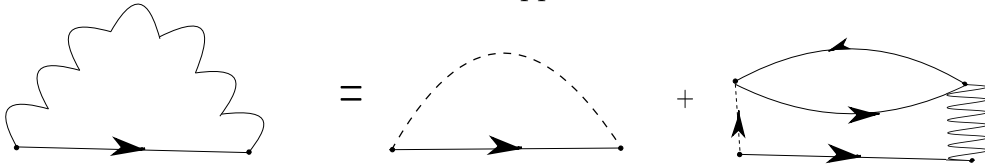Montroll-Ward approximation

Figure 3.11.: Montroll-Ward approximation.

The real part of the dielectric function is given by

$$\mathrm{Re}\,\epsilon(\mathbf{q}, \omega) = 1 + \sum_{a, s_a^z} \frac{4\pi\hbar^2 e_a^2}{q^2} \mathcal{P} \int \frac{d\mathbf{p}}{(2\pi\hbar)^3} \frac{f_a(\mathbf{p} + \mathbf{q}) - f_a(\mathbf{p})}{\hbar\omega + E_a(\mathbf{p}) - E_a(\mathbf{p} + \mathbf{q})}. \tag{3.116}$$

3. Line Shift due to Plasma Environment

Integral over angular part,

$$\text{Re}\epsilon(\mathbf{q}\omega, \mathbf{R}t) = 1 - 2\pi \sum_{a,s_a^z} m_a \frac{4\pi\hbar^2 e_a^2}{q^2} \mathcal{P} \int_{-\infty}^{\infty} \frac{dp}{(2\pi\hbar)^3} p f_a(\mathbf{p}, \mathbf{R}t) \frac{1}{2q} \tag{3.117}$$

$$\left\{ \ln\left(\frac{pa_B}{\hbar} - \frac{qa_B}{2\hbar} - \frac{m_a \omega a_B}{q} \right) + \ln\left(\frac{pa_B}{\hbar} - \frac{qa_B}{2\hbar} + \frac{m_a \omega a_B}{q} \right). \right\} \tag{3.118}$$

[18] The real part of the self energy can be decomposed into a Hartree-Fock self energy term and the real part of the Montroll-Ward self energy,

$$\text{Re}\Sigma_a(\mathbf{p}, \omega) = \Sigma_a^{\text{HF}}(\mathbf{p}) + \text{Re}\Sigma_a^{\text{MW}}(\mathbf{p}, \omega). \tag{3.119}$$

The pressure equation can be written with Hartree term, Hartree-Fock term and Montroll-Ward term

$$p - p_0 = p^{\text{H}} + p^{\text{HF}} + p^{\text{MW}}. \tag{3.120}$$

The ideal pressure is $p_0 = \sum_a \frac{2s_a+1}{\beta\Lambda_a^3} I_{3/2}(\beta\mu_a)$. The pressure of Hartree-Fock term is

$$p^{\text{HF}}(\{\mu_a\}) = \sum_a \frac{2s_a + 1}{\Lambda_a^4} e_a^2 \int_{-\infty}^{\beta\mu_a} dx I_{-1/2}^2(x). \tag{3.121}$$

The μ_a is chemical potential. The pressure of Montroll-Ward term combined with the RPA dielectric function is

$$p^{\text{MW}} = \pm \int \frac{d\lambda}{\lambda} \frac{d\mathbf{p}}{(2\pi)^3} \frac{d\omega}{2\pi} n_B(\omega)\{\text{Im}\epsilon^{-1}(\mathbf{p}\omega) + \text{Im}\epsilon(\mathbf{p}\omega)\} \tag{3.122}$$

$$= -\int \frac{d\mathbf{p}}{(2\pi)^3} \int_0^\omega \frac{d\omega}{2\pi} \coth\frac{\beta\hbar\omega}{2} \cdot \left[\arctan\frac{\text{Im}\epsilon(\mathbf{p}\omega)}{\text{Re}\epsilon(\mathbf{p}\omega)} - \text{Im}\epsilon(\mathbf{p}\omega). \right]. \tag{3.123}$$

See [18], so that

$$p = p^0 + p^{\text{HF}} + p^{\text{MW}} \tag{3.124}$$

$$= \sum_a \frac{2s_a + 1}{\beta\Lambda_a^3} I_{3/2}(\beta\mu_a) + \sum_a \frac{2s_a + 1}{\Lambda_a^4} e_a^2 e_a^2 \int_{-\infty}^{\beta\mu_a} dx I_{-1/2}^2 \tag{3.125}$$

$$- \int \frac{d\mathbf{p}}{(2\pi)^3} \int_0^\omega \frac{d\omega}{2\pi} \coth\frac{\beta\hbar\omega}{2} \cdot \left[\arctan\frac{\text{Im}\epsilon(\mathbf{p}\omega)}{\text{Re}\epsilon(\mathbf{p}\omega)} - \text{Im}\epsilon(\mathbf{p}\omega). \right]. \tag{3.126}$$

The density function is $n_a = \frac{\partial p}{\partial \mu_a}$. Derivation the equation of pressure gives

$$n_a = \ln \frac{2s_a + 1}{\Lambda_a^3} I_{1/2}(\beta\mu_a) + \frac{2s_a + 1}{\Lambda_a^4} \beta e_a^2 I_{-1/2}^2(\beta\mu_a) + \frac{\partial}{\partial \mu_a} p^{\text{MW}}. \tag{3.127}$$

In the low density limit, the pressure can be approximated to

$$\beta p^{\text{MW}} = \frac{\kappa^3}{12\pi} - \frac{1}{4}\pi^{3/2} \sum_{ab} z_a z_b \lambda_{ab}^3 \zeta_{ab}^2. \tag{3.128}$$

The $\zeta_{ab} = -\beta\frac{e_a e_b}{\lambda_{ab}} = -\frac{e_a e_b}{\hbar}\sqrt{\frac{2m_{ab}}{kT}}$ is Born parameter. The total pressure expansion in fugacity form can be written [18]

$$\beta p(z_c) = \sum_a z_a + \frac{\kappa^3}{12\pi} + 2\pi \sum_{ab} z_a z_b \lambda_{ab}^3 \left\{ -\frac{\delta_{ab}}{2s_a+1}\left(\frac{\sqrt{\pi}}{4} + \frac{\zeta_{ab}}{2}\right) - \frac{\sqrt{\pi}}{8}\zeta_{ab}^2. \right\} \tag{3.129}$$

The density is given by

$$n_a(z) = z_a + \frac{\kappa^3}{8\pi} + 2\pi \sum_b z_a z_b \lambda_{ab} 13 \left\{ -\frac{\sqrt{\pi}}{8}\zeta_{ab}^2 - \frac{\delta_{ab}}{2s_a+1}\left(\frac{\sqrt{\pi}}{4} + \frac{\zeta_{ab}}{2}\right). \right\} \tag{3.130}$$

The chemical potential is given by

$$\mu_a = \mu_a^{\mathrm{id}} - \frac{\kappa e^2}{2} - 2\pi \sum_b n_b \lambda_{ab}^3 \left\{ -\sqrt{\pi}\frac{\zeta_{ab}^2}{8} - \frac{\delta_{ab}}{2s_a+1}\left(\frac{\sqrt{\pi}}{4} + \frac{\zeta_{ab}}{2}\right) \right\} \tag{3.131}$$

$$= \ln\frac{n_e \lambda_e^3}{2} - \frac{e^2}{2}\sqrt{\frac{n_e e^2}{\epsilon_0 k_{\mathrm{B}}T}} + \frac{\sqrt{2\pi^2}n_e \lambda_e e^4}{8(k_{\mathrm{B}}T)^2} - \frac{n_e \lambda_e^3}{8\sqrt{2}} + \frac{n_e \lambda_e^2 e^2}{4k_{\mathrm{B}T}} \tag{3.132}$$

[18].

The electron-electron quasi-particle shift of Montroll-Ward approximation can be written as

$$\Delta_e^{\mathrm{MW}} = \Delta_e^{\mathrm{DH}} + \frac{\sqrt{2\pi^2}n_e \lambda_e e^4}{8(k_{\mathrm{B}}T)^2} - \frac{n_e \lambda_e^3}{8\sqrt{2}} + \frac{n_e \lambda_e^2 e^2}{4k_{\mathrm{B}}T}. \tag{3.133}$$
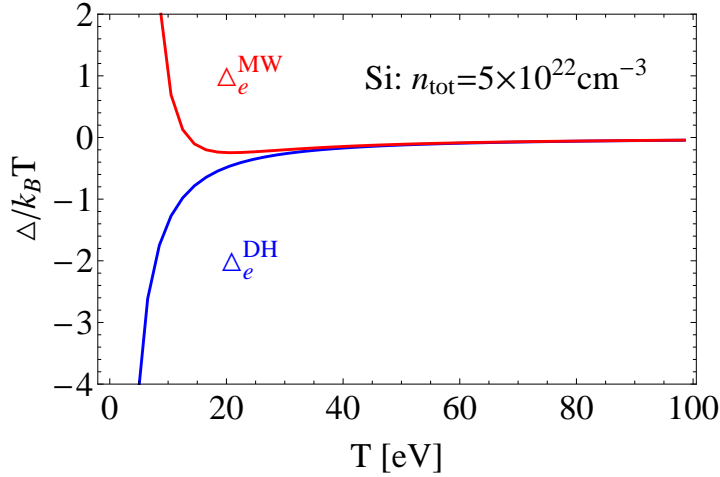

Figure 3.12.: Montroll-Ward (red curve) and Debye Hückel (blue curve) self energy for different temperatures on electron electron interaction shift in the plasma environment. At temperatures above 30 eV both curves have the same behavior.

Fig. 3.12 shows the self energy with respect to the temperature in Debye-Hückel (DH) and Montroll-Ward (MW) approximation. At the higher temperature both curves show the same behavior. But it is seen, that the dynamical terms in the Montroll-Ward approximation gives corrections to the Debye-Hückel theory for lower temperatures. However, coming close to the degeneracy limit $\Theta = \frac{k_B T}{E_{\text{Fermi}}} \approx 1$ both approximations fail. Taking degeneracy into account a more thorough ansatz has to be made applying Fermi distributions and integrals.

4. Plasma Composition

In the classical non-degenerate case, the contribution of the discrete energy spectrum of the excited ions to the partition function is given by

$\sigma_e(T) = \sum_i g_i e^{-E_i/T}$ with statistical factor g_i and energy of state of ionization E_i. For the continuous energy we have in the non-degenerate case for the canonical partition function of N electrons the partition function contribution of the continuous energy spectrum

$$\sigma_e = \frac{1}{N!} \left[2 \int dV \iiint \exp\left[-\frac{1}{2m_e k_B T}(p_x^2 + p_y^2 + p_z^2) \right] \frac{dp_x dp_y dp_z}{(2\pi\hbar)^3} \right]^N$$
$$= 2^N V^N \left(\frac{m_e k_B T}{2\pi\hbar^2} \right)^{3N/2} \tag{4.1}$$
$$= 2^N \frac{1}{N!} \left(\frac{V}{\lambda^3} \right)^N .$$

In Eq. (4.1) the mass of electron is m_e, N is the number of electrons, the factor 2 comes from the spin states of the electron, λ is thermal wave length, V is the volume of the system and the single particle energy is $E_i = \frac{1}{2m_e}(p_x^2 + p_y^2 + p_z^2)$.

In the classical non-degenerate case, the total energy of ions consists of the kinetic energy E_k and the potential energies E_b. The total energy is $E = E_k + E_b$. The contribution of the kinetic energy partition function is

$$\sigma_{i,k} = \frac{1}{N!} \left[\int dV \iiint \exp\left[-\frac{1}{2m_i k_B T}(p_x^2 + p_y^2 + p_z^2) \right] \frac{dp_x dp_y dp_z}{(2\pi\hbar)^3} \right]^N$$
$$= \frac{1}{N!} V^N \left(\frac{m_i k_B T}{2\pi\hbar^2} \right)^{3N/2} . \tag{4.2}$$

The contribution of potential energy E_b to the partition function due to the binding energy of the ionic state.

$$\sigma_i = \sum_n \exp\left(-\frac{E_{i,n}}{k_B T} \right) . \tag{4.3}$$

In Eq. (4.3), the bound state has the mass of ion m_i. The total partition function is given by

$$\sigma_i(T) = \sigma_{i,k} \cdot \sigma_{i,b}$$
$$= \frac{1}{N!} V^N \left(\frac{m_i k_B T}{2\pi\hbar^2} \right)^{3N/2} \sum_n \exp\left(-\frac{E_{i,n}}{k_B T} \right) . \tag{4.4}$$

The Wigner-Seitz radius R is defined by $R = \left(\frac{3}{4\pi n_e}\right)^{1/3}$. The ion sphere has the radius R when one electron charge is considered for each ion corresponding to ion-electron potential in the plasma. The energy of electron-ion quasi-particle shift is given by [27]

$$\Delta_e^{ei} = -\frac{Z_{ion}e^2}{4\pi\epsilon_0 R} = -\frac{e^2}{\epsilon_0}\left(\frac{Z_{ion}}{4\pi}\right)^{2/3}\left(\frac{n_e}{3}\right)^{1/3}. \tag{4.5}$$

The partition function of electron-ion contributes as

$$\sigma_e^{in}(m) = 2^m exp\left[\frac{1}{k_B T}\left(\frac{e^2}{\epsilon_0}\left(\frac{Z_{ion}}{4\pi}\right)^{2/3}\left(\frac{n_e}{3}\right)^{1/3}\right)\right] \tag{4.6}$$

The effective Z_{ion} is defined by sum of all number of ionisiation steps.

$$(Z_{ion})^{2/3} = \sum_{x=1}^{m}(x)^{2/3}$$

with the m: number of ionisiation steps then the internal partition function can be written as

$$\sigma_e^{in}(m) = 2^m exp\left[\frac{1}{k_B T}\frac{e^2}{(4\pi)^{2/3}\epsilon_0}\left(\frac{n_e}{3}\right)^{1/3}\sum_{x=1}^{m}x^{2/3}\right]. \tag{4.7}$$

The electron-electron quasi-particle energy shift due to the Montroll-Ward term in addition to the ideal particle term $\mu_e^{id} = \frac{n_e\Lambda_e^3}{2}$ and the Debye term $\Delta_e^{DH} = -\frac{e^2}{2}\sqrt{\frac{n_e e^2}{\epsilon_0 k_B T}}$ in the partition function (3.133), see also [27].

The total partition function follows as

$$\sigma_e^{in}(m) = 2^m \exp\left[-\frac{\Delta_e^{MW}}{k_B T}\right]^m \exp\left[\frac{1}{k_B T}\frac{e^2}{(4\pi)^{2/3}\epsilon_0}\left(\frac{n_e}{3}\right)^{1/3}\sum_{x=1}^{m}x^{2/3}\right]. \tag{4.8}$$

4.1. Internal Partition Function

The internal partition function describes the statistical weight of the respective particles of plasma depending on the individual temperature. In general the composition of the plasma was calculated by the degree of ionization of the internal partition function using coupled Saha equation within a partially ifig:gonized plasma in local thermal equilibrium. Continuum lowering of ionization was included in self energy contribution to the chemical potentials and the renormalized Planck Larkin expression [40]. We apply the basic approximation of the Saha equation of hydrogen plasma [18] to the M-shell ions (Si and Ar) in our model. In the chemical picture we have a mixture of particles: atoms A^0 of Ar or Si, all different m-fold charge states of ions A^m and electrons e. In chemical equilibrium the chemical potentials satisfy $\mu_{A^m} = \mu_{A^{m+1}} + \mu_e$. The chemical potential for each component c is $\mu_c = k_B T \ln \frac{n_c \Lambda_c^3}{\sigma_c^{in}}$. Using the free electron statistical

factor $g_e = 2$ and the thermal wavelength of the $m + 1$ ionization stage assuming the same on the m stage, with $\Lambda_{A^{m+1}} = \Lambda_{A^m}$ we derive

$$\frac{n_{A^{m+1}} n_e}{n_{A^m}} = \frac{2}{\Lambda_e^3} \frac{\sigma_{A^{m+1}}^{in}}{\sigma_{A^m}^{in}}. \tag{4.9}$$

Equation (4.9) can be written via the coupled Saha equation with

$$n_{A^m} = \left[\frac{2}{n_e \Lambda_e^3}\right]^m \frac{\sigma_{A^m}^{in}}{\sigma_{A^0}^{in}} n_{A^0}. \tag{4.10}$$

We calculate beginning from the solid bulk density in the plasma environment with different temperatures,

$$n_{solid} = \sum_0^z n_{A^m}. \tag{4.11}$$

Now we consider the internal partition function of the hydrogen atom by the all possible bound states in the quantum statistical system [18].

$$\sigma_H^{in,bound} = \sum_{nl}(2l + 1) \exp\left[-\frac{E_{nl}}{k_B T}\right]. \tag{4.12}$$

The symbol of principal quantum number is n and the symbol of angular quantum number is l with $l \leq n - 1$. The binding energies of bound atom E_{nl} could be vanish with the pressure of ionization due to the plasma screening effect. A more detailed approach may be given according to the Beth-Uhlenbeck formula that describes the internal partition function with binding energies and continuum contribution.

$$\sigma^{in} = \sum_{nl}(2l + 1) \exp\left[-\frac{E_{nl}}{k_B T}\right] + \int dE_p \exp\left[-\frac{E_p}{k_B T}\right] \sum_l (2l + 1)\frac{1}{\pi}\frac{d\delta_l(E_p)}{dE_p}. \tag{4.13}$$

The scattering phase shifts $\delta_l(E_p)$ depend on the energy $E_p = \frac{p^2}{2m}$ of kinetic energy of free electrons. The first term of right side of Eq. (4.13) describes bound effect of atom that disappear at $E_{nl} \to 0$ and the second term describes scattering states of continuum states. The first term in the bound quantum states and second term effect describes contribution of continuum quantum states. Using a Taylor expansion we get $\exp\left[-\frac{E_{nl}}{k_B T}\right] = 1 - \frac{E_{nl}}{k_B T} \pm \cdots$ solving the case $E_{nl} \to 0$ useful the residual higher order term $\exp\left[-\frac{E_{nl}}{k_B T}\right] - 1 + \frac{E_{nl}}{k_B T}$. Ignoring the scattering term we rewrite Eq. (4.13)

$$\sigma^{in,PL} = \sum_{nl}(2l + 1)\left(\exp\left[-\frac{E_{nl}}{k_B T}\right] - 1 + \frac{E_{nl}}{k_B T}\right). \tag{4.14}$$

Eq. (4.14) is the famous Planck Larkin internal partition function proposed by Planck, Brillouin, Vedenov and Larkin in 1957 [18]. Between the mth ionization stage of ion with energy $E_0^{A^m}$ to the $m + 1$ ionization stage of the ion energy $E_0^{A^{m+1}}$ we have some

possible excited states $\Delta E_i^{A^m}$ (e.q. 3p, 3d, 4s) of the valence electron. The ionization energy of the m stage of the ion is $E_i^{A^m} = E_0^{A^{m+1}} + \Delta E_i^{A^m}$ and then is exploited to $\sum_i \exp\left[-\frac{E_i^{A^m}}{k_B T}\right] = \exp\left[-\frac{E_0^{A^{m+1}}}{k_B T}\right] \sum_i \exp\left[-\frac{\Delta E_i^{A^m}}{k_B T}\right]$. The internal Planck Larkin equation (4.14) can be written

$$\sigma_{A^m}^{in,PL} = g_{A^m} \exp\left[-\frac{E_0^{A^{m+1}}}{k_B T}\right] \sum_i \left(\exp\left[-\frac{\Delta E_i^{A^m}}{k_B T}\right] - 1 + \frac{\Delta E_i^{A^m}}{k_B T}\right) \tag{4.15}$$

$$= \sum_i g_{A^m} \exp\left[-\frac{E_0^{A^{m+1}}}{k_B T}\right] \left(\exp\left[\frac{\Delta E_i^m}{k_B T}\right] - 1 - \frac{E_i^m}{k_B T}\right). \tag{4.16}$$

g_{A^m} is the statistical factor of the mth excitation stage of the ion stage and each different state m of g_{A^m} calculates by LS coupling of the open shell ions. LS coupling can use not just each state of ions but also for each excited state of ions in the 3p, 3d or 4s state of the M shell. The Saha equation (4.10) can be described

$$\frac{n_{A^{m+1}} n_e}{n_{A^m}} = \frac{2}{\Lambda_e^3} \frac{g_{A^{m+1}}}{g_{A^m}} \exp\left[-\frac{\Delta E_i^m}{k_B T}\right]. \tag{4.17}$$

The E_{ion}^m was calculated by *ab initio* code Gaussian 03 with Aug-cc-pVTZ basis set of Ar and 3-21G* basis set of Si. The chemical *ab initio* Gaussian does not consider the fine structure components for the eigen energies of K_α. In 2009, A. Sengebusch was applying the internal partition function of Ti and Cl [40].

Fig. 4.1 shows the Si plasma composition from the temperature 20 eV to 100 eV using the coupled Saha self-consistent calculation in local thermal equilibrium. Going to Fig. 4.1a shows as function of the temperature of the plasma contributions from Si-like to B-like ions. We consider the total probability equal to 1 at each temperature with different compositions. Going to Fig. 4.1b shows the free electron density as function of the temperature. Higher temperature has a higher free electron density in the plasma.

Fig. 4.2 shows the Ar plasma composition for temperatures 10 eV to 170 eV. Going to Fig. 4.2a shows as function of the temperature of the plasma the contributions from Ar-like to B-like ions with total probability equal to 1. In Fig. 4.2a when the temperature is bigger than 50 eV L shell ionization (from Ne) occurrence. Increasing temperature has more free electron densities. This also means the temperature less than 50 eV is the stronger effect on K_α for an important plasma diagnostics process. From temperature 60 eV to 80 eV we have a bigger weight of plasma composition for Ar^{10+}, 70 eV to 100 eV is for Ar^{11+}, 110 eV to 130 eV is for Ar^{12+}, 130 eV to 150 eV is for Ar^{13+} and 150 eV to 170 eV is for Ar^{14+}. In Fig. 4.2b shows Ar free electron density n_e depending on temperature calculated from Ar bulk density. In the range of 10 eV to 50 eV we have stronger contributions to the composition from M shell electrons (Ar-Like to Na-Like).

4.2. FLYCHK

The FLYCHK code considers the local thermodynamic equilibrium model with Boltzmann statistics and Saha ionization distribution. The FLYCHK code has calculated the
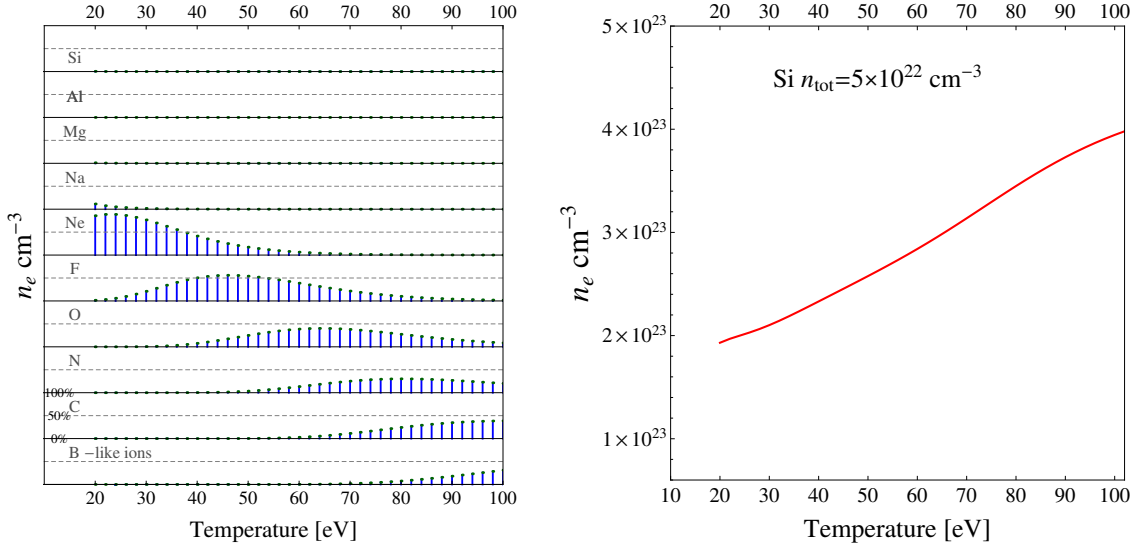
(a) Composition Ionization of Si at solid atom density of silicon is $5.0 \cdot 10^{22}$ cm^{-3} as function of T. We use the Saha equation and the Planck Larkin partition function iterated the stages (from Si-like to B-like) of the internal partition function. In M-shell electrons (Si, Al, Mg, Na) at temperature 20 eV to 100 eV have small contribution. Each temperature with different compositions has the total probability 1.

(b) Si comparing the plasma composition in Fig. (a) shows the free electron density n_e depending on temperature from $T = 20$ eV , $n_e = 2.0 \cdot 10^{23}$ cm^{-3} to $T = 100$ eV, $n_e = 4.0 \cdot 10^{23}$ cm^{-3}. Corresponding the increasing temperature has more increasing free electron densities.

Figure 4.1.: Si self-consistent calculation assuming local thermal equilibrium conditions showing rising ionization with rising temperature.

ionization distributions of plasmas. For the calculation of plasma spectroscopy the FLYCHK is a suited computer code and the users need just give some simple parameters [41]. Some advantages of FLYCHK are simple and fast. For running code does not need any atomic data input because the data are stored internally. This code focuses on K-shell spectra for low Z ions from $Z=2$ to $Z=26$. We use the argon charge state distribution for non-local thermodynamic equilibrium (NLTE) also called collisional-radiative (CR) model calculation at NIST [42]. CR model are calculated by solving multi-level ionization self-consistent with the Saha equation in a radiation field. The radiation transport equation of CR brings in non-local contributions to population distribution calculations. CR modeling can be used to diagnose laser-produced plasmas in X-rays spectroscopy. Plasmas produced by high-power lasers in some eV to keV with electron densities as high as the range of 10^{21}cm^{-3} to 10^{25}cm^{-3} [42]. The advantages of FLYCHK makes it possible to analyze complex plasma processes quickly in K_α spectroscopic measurements and help us to understand the plasma states with fixed electron density N_e. In Fig. 4.3a the Si plasma composition is shown with different charge states corresponding to different temperature using FLYCHK. The temperature at 30 eV for $N_e = 10^{23}$cm^{-3} (green line) is suitable to compare with our plasma composition, see Fig. 4.1b. In Fig.
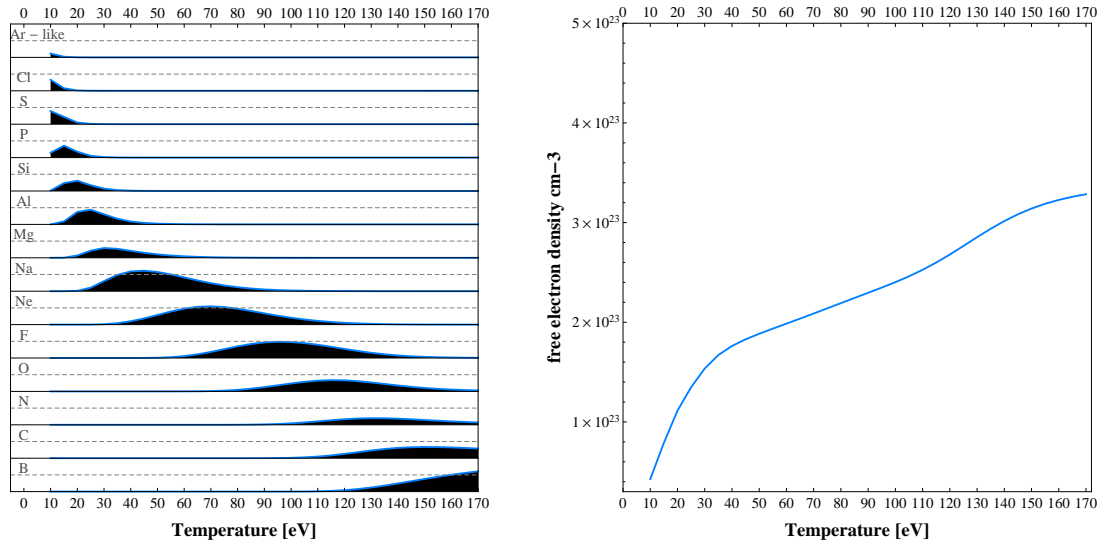
(a) Ar solid density of isolated silicon is $2.63 \cdot 10^{22}$ cm^{-3} using Saha equation and Planck Larkin equation iterated the stages (from Ar-like to B-Like) of internal partition function calculating the range of temperature from 10 eV to 170 eV.

(b) Ar comparing the plasma composition in Fig (a) shows the free electron density n_e depending on temperature. Corresponding the increasing temperature has more increasing free electron densities. Increasing temperature from 10 eV to 30 eV have sharply free electron density n_e increasing corresponding the ionization states (Ar-Like to Na-like) in M shell and go to the (Ne- like to B-like) L-shell have more smoothly free electron density n_e increasing.

Figure 4.2.: Ar self-consistent calculation assuming local thermal equilibrium conditions determined rising ionization with rising temperature.

4.3b the blue line describes the free electron density 10^{22}cm^{-3} and the red line describes the electron density is 10^{23} cm^{-3} with different temperature and corresponding to the charge states of plasma. The red line has higher free electron density than the blue line. We can see the higher temperature going to smaller charge state than the blue line. The FLYCHK uses the non-local thermodynamic equilibrium and our model uses local thermodynamic equilibrium with the coupled Saha equation with the Planck Larkin equation for continuing ionization energy of charge state.

In Fig. 4.3b we compare our plasma composition on the different charge states comparing with FLYCHK. We see here our result in the lower temperature (< 50 eV) to give the behavior like FLYCHK a free electron density 10^{22} cm^{-3} and in the higher temperature (50 eV $< T <$ 170 eV) the behavior close to the FLYCHK the free electron density 10^{23} cm^{-3}. The result is quite good, because in our model the free electron density is a parameter depending on temperature for fixed solid electron density.
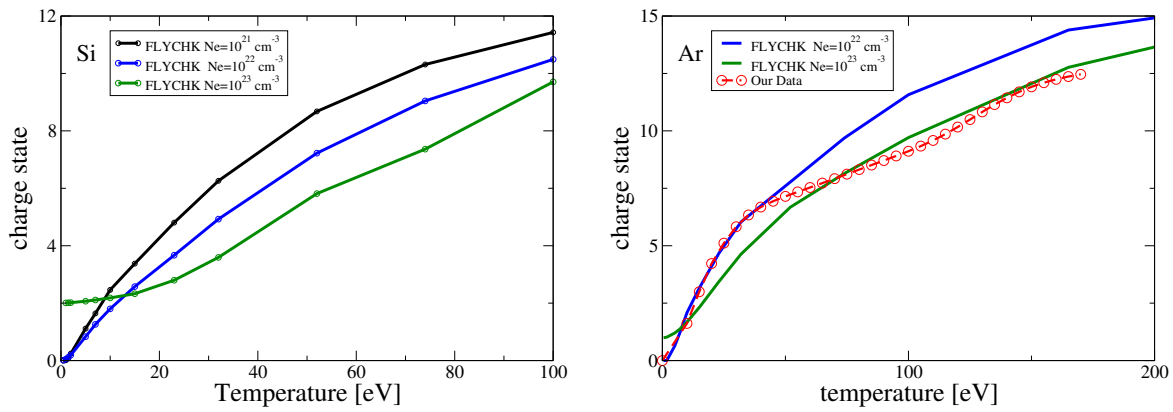
(a) Si plasma composition of charge state with different temperatures from 1 eV to 100 eV calculation by FLYCHK. The black curve is $N_e = \cdot 10^{21}$cm^{-3}. The blue curve is $N_e = \cdot 10^{22}$cm^{-3}. And green curve is $N_e = \cdot 10^{23}$cm^{-3}.

(b) Ar $n_{\text{tot}} = 2.636\cdot 10^{22}$cm^{-3} in our data (red curve). Compare composition of charge state with FLYCHK plasma the composition with different temperatures from 10 eV to 170 eV in blue curve $N_e = 10^{22}$cm^{-3} and green curve $N_e = 10^{23}$cm^{-3}.

Figure 4.3.: Si and Ar ionization distribution with temperature calculation by FLYCHK. Using the charge state distribution for non-local thermodynamic equilibrium calculation at NIST.

5. Synthetic Spectra

We use the self-consistent Roothann-Hartree-Fock approximation of Si and Ar wave function for the unperturbed emitter, see section 2.2 and section 2.2. The total Hamiltonian $H = H^0 + H'$ consists of the unperturbed Hamiltonian H^0 and the perturbation H' which describes the plasma effect. Assuming φ_i is the wave function of the initial and φ_f of the final level of the electron transition (2p $\rightarrow$ 1s), the spectral line shift can be calculated with Bunge wave functions. The line shifts are dependent on both the plasma temperature $k_B T$ and the average free electron density n_e, see section 3.3.2. The total internal partition function is given by Eq. (4.8). We consider the renormalized Planck Larkin Eq. (4.15). Then we use coupled Saha equation with Planck-Larkin equation to get Eq. (4.17). To construct synthetic spectra from the so far determined shifted emission energies every line (as well as its fine structure components) is assigned a Lorentz profile with natural line width γ and maximum intensity I_{max} will discuss in section 5.1. The central line position E_0 is assumed to be the position of the $p_{3/2}$ component of the transition. To take into account fine structure splitting, we add the $p_{1/2}$ components semi-emprically. Finally, the Lorentzians are summed up and convoluted with a Gaussian profile of width Γ to take into account instrumental broadening of measurements what will be discussed in section 5.2.

5.1. Radiative Transitions with Einstein Coefficients

Bremsstrahlung is continuous radiation due to acceleration of free electrons. We focus on transitions of bound electrons between two atomic levels. The transitions of bound electrons between the various energy levels of atomic system could emit radiation. Using spectroscopic measurement the energy level structure of atoms can be determined. We will calculate the theoretical energy level structure of atoms for plasma diagnostics taking into account the plasma environment. We consider spontaneous transitions from the state E_i to state E_f. For K_α, see Fig. 1.1 the electron in the upper level (1s one hole) with the initial the initial state configuration energy E_i can decay spontaneously to the lower level E_f (2p one hole) getting the final state configuration energy E_f with the emission of a photon whose frequency is $h \cdot \nu_{if}$. The K_α fluorescence emission was recorded to [45]

$$E_i - E_f = h \cdot \nu_{if}. \tag{5.1}$$

In the thermal equilibrium the ratio of number of atoms $\frac{N_i}{N_f}$ can be described with the upper energy level of density n_i and the lower energy level of density n_f in the

5. Synthetic Spectra

Boltzmann distribution [43]

$$\frac{N_i}{N_f} = \frac{g_i}{g_f} \exp\left[-(E_i - E_f)/T\right] = \frac{g_i}{g_f} \exp(-h \cdot \nu_{if}/T). \tag{5.2}$$

These bound electrons level i and f are not single quantum states but in the degenerate states g_i and g_f. The energy density is in thermal equilibrium given by the blackbody radiation

$$\rho(\nu) = \frac{8\pi h \nu^3}{c^3 \left[\exp(h\nu/T) - 1\right]}. \tag{5.3}$$

The energy transition conservation in an equilibrium of the total rate transition from i to f is equal

$$\left[A_{if} + B_{if}\rho(\nu_{if})\right] N_i = B_{fi}\rho(\nu_{if})N_f. \tag{5.4}$$

The spontaneous transition probability per unit time denoted A_{ij}. The probability of absorption per unit time is given by $B_{fi}\rho(\nu_{if})$ and the probability of emission per unit time could write $B_{if}\rho(\nu_{if})$. These three coefficients A_{if}, B_{fi}, B_{if} are called Einstein coefficients for the bound electrons transition. The relationship between these three Einstein coefficients A_{if}, B_{fi}, B_{if} is given by Eq. (5.4) and $g_f B_{fi} = g_i B_{if}$. The S_{ij} is an atomic dipole moment [43] called in spectroscopy the transition strength with degenerate states m_i and m_f

$$S_{if} = \left| \int \psi_i^* \mathbf{r} \psi_f d^3 r \right|^2 \tag{5.5}$$

$$= \sum_{m_i, m_f} |\langle i, m_i | \mathbf{D} | f, m_f \rangle|^2. \tag{5.6}$$

The $\mathbf{D}$ is the dipole operator. Einstein coefficient of emission is given by

$$B_{if} = \frac{2\pi^2 e^2}{3\epsilon_0 \hbar^2} \left| \int \psi_i^* \mathbf{r} \psi_f d^3 r \right|^2. \tag{5.7}$$

The i is the initial state, and f is the final state. A_{if} is independent from an external radiation field. The spontaneous Emission depends only on the wave functions of transition from E_i to E_f. The average power of emission from state E_i with the N_i atoms are described by

$$\langle P \rangle = N_i \cdot A_{if} \cdot h \cdot \nu_{if}. \tag{5.8}$$

A_{if} is the spontaneous transition probability given by [45]

$$A_{if} = \frac{2e^2 \omega_{if}^3}{3\epsilon_0 c^3 h} \left| \int \psi_i^* \mathbf{r} \psi_f d^3 r \right|^2. \tag{5.9}$$

We conbine the Eq. (5.7) with Eq. (5.9) to get the relation

$$A_{if} = \frac{8\pi h \nu_{if}^3}{c^3} B_{if} \tag{5.10}$$

with $\omega_{if} = 2\pi\nu_{if}$, $\hbar = \frac{h}{2\pi}$. The emission energy E_0 is equal to $h \cdot \nu_{if}$ or $\hbar \cdot \omega_{if}$ with $\omega_{if} = \frac{E_0}{\hbar}$. So the spontaneous transition probability of Einstein coefficient is given by [45]

$$
\begin{aligned}
\langle P \rangle &= N_i \cdot A_{ij} \cdot h \cdot \nu_{if} \\
&= N_i \cdot \frac{2e^2\omega_{if}^3}{3\epsilon_0 c^3 h} \left| \frac{1}{\Omega_0} \int \psi_i^* \mathbf{r} \psi_f d^3 r \right|^2 \cdot h \cdot \nu_{if} \\
&= N_i \cdot \frac{2e^2\omega_{if}^4}{3\epsilon_0 c^3 2\pi} \left| \frac{1}{\Omega_0} \int \psi_i^* \mathbf{r} \psi_f d^3 r \right|^2 \\
&= N_i \cdot \frac{2e^2 E_0^4}{3\epsilon_0 c^3 \hbar^4 2\pi} \left| \frac{1}{\Omega_0} \int \psi_i^* \mathbf{r} \psi_f d^3 r \right|^2 \\
&= N_i E_0 A_{if}.
\end{aligned}
$$

The single Lorentz profile is assigned to a single emission line given by

$$
f(E, E_0, \gamma/2, I_{max}) = \frac{I_{max}(\gamma/2)^2}{(E - E_0)^2 + (\gamma/2)^2}. \tag{5.11}
$$

In the center of the Lorentz profile is the emission energy E_0. It can dependent on plasma shift. The height of the profile is found by I_{max} corresponding emitters in intensity maximum and $\gamma/2$ is the half-width in Lorentzian function. The maximum intensity is mainly given by the emitter abundance in the plasma. We determine all intensities relative to a reference state according to [27, 45],

$$
\frac{I_{max}}{I_{ref}} = \frac{N_i E_0 A}{N_{ref} E_0^{ref} A_{ref}} \simeq \frac{n_i}{n_{ref}} \left(\frac{E_0}{E_0^{ref}} \right)^4. \tag{5.12}
$$

n_i is the density of particles. We set a reference transition I_{ref} to relative the maximum intensity of the Lorentz profile I_{max}. The central position is determined by the position of each $p_{3/2}$ component of spectral lines. We use fine structure splitting and get $p_{1/2}$ component on each spectral line. The fine structure splitting of silicon is 0.591 eV. The maximum intensity considers to corresponding to the component $p_{3/2}$ with a statistical weight 2J +1, and the other states in the outer and inner open shells consider also with a statistical weight 2J +1 to get their intensity. The statistical weight 2J+1 satisfied the singlet-triplet-factor for each component on $p_{3/2}$ and $p_{1/2}$. The singlet-triplet-factor influence the height of the intensity of each peak.

5.2. Line Broadening

The emission spectral lines emitted by bound-bound transitions show line broadening which is important for the plasma diagnostics. Lorentzian linewidth γ and instrumental Gaussian width Γ have to be considered. The Lorentzian linewidth γ is also called natural

5. Synthetic Spectra

line broadening. Now let us explain the natural line broadening from the quantum states of an atom. In the quantum states have discrete energies of different energy states. The atomic system have interaction with electromagnetic fields due to small spread in energy. The lifetime τ of the atom in an upper state is finite due to spontaneous transitions to lower quantum states. The effective energy spread in the quantum state is given by [43]

$$\Delta E \simeq \frac{h}{2\pi\tau}. \tag{5.13}$$

In Eq. (5.13) the lifetime τ is getting by the sum of all spontaneous transitions $\frac{2}{\tau} = \sum_f A_{if}$. The frequency is equal to $\Delta\nu = \frac{1}{2\pi\tau}$. The shape of the broadened line is the shape of the energy broadening in the Lorentz profile. The Lorentzian line shape of natural broadening could be rewritten by [43]

$$I(\nu) = I(\nu_0)\frac{1}{1 + [(\nu - \nu_0)2\pi\tau]^2}. \tag{5.14}$$

In Eq. (5.14) the natural broadening we use the experiment natural broadening in our calculation and the full width at half maximum is called FWHM. The lifetime is defined by $\Delta\nu_{1/2} = \frac{1}{\pi\tau}$. FWHM arising from the Doppler shift of parameter frequency ν is defined by [43],[44].

$$\Delta\nu_{1/2} = 2\nu_0(v_{ta}/c)(2\ln 2)^{1/2}. \tag{5.15}$$

The factor 2 is from the definition of life time τ included to provide a standard form of the line profile. Doppler shift describes the thermal particle motion

$$\Delta\nu = \nu - \nu_0 = \frac{\nu_0 v}{c}. \tag{5.16}$$

In Eq. (5.16) shows c is light velocity and v is the particle velocity. The Maxwellian velocity distribution is described by

$$I(\nu) = I(\nu_0)\exp\left[\frac{-(\nu - \nu_0)^2 c^2}{2v_{ta}^2\nu_0^2}\right]. \tag{5.17}$$

In Eq. (5.17) has the relationship from temperature $k_B T_a$ and atomic mass m_a on an emitting atom $v_{ta}^2 = \frac{k_B T_a}{m_a}$ and in Eq. (5.17) of right side shows the Gaussian line profile.

We added all of the individual spectral lines of Lorentz profile and convoluted with a Gaussian instrument function to satisfy the resolution of spectrometer in the experiment.

$$I(E) = \int_{-\infty}^{\infty} dz I(E + z)\frac{1}{\sqrt{2\pi\Gamma^2}}\exp\left[-\frac{z^2}{2\Gamma^2}\right]. \tag{5.18}$$

Using Eq. (5.18) we calculate the silicon spectra shown in section 5.3 and argon spectra seeing section 5.4.

(a) Theoretical Si $K_\alpha L^0$ emission energies (shifted by plasma) and resulting spectrum.

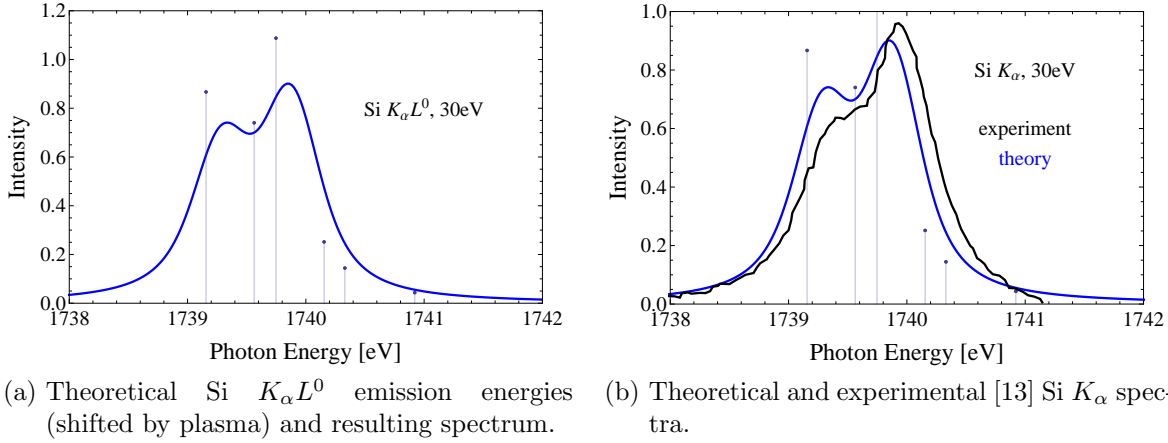(b) Theoretical and experimental [13] Si K_α spectra.

Figure 5.1.: Si spectrum considering the ground state and satellite emission lines from excited state of 4s and excited state of 3d, fine structure splitting is taken into account for statistical factors of different excited states, see Tab. 2.1.

5.3. Silicon Spectra

We calculated synthetic silicon K_α spectra at a plasma temperature of 30 eV and the Si atom bulk density $n_{tot} = 5 \cdot 10^{22}$ cm^{-3}. The Gaussian width was fixed from instrumental profile $\Gamma_G = 0.13$ eV [12] and the Lorentzian distribution linewidth was fixed $\gamma = 0.43$ eV [12] in our calculation.

We considered different L-shell satellites for two different M-shell configurations: $K_\alpha L^N M^0$ and $K_\alpha L^N M^4$ for $N = 0, ..., 4$, respectively. The experimental results for K_α spectra of Si, SiO_2 have shown that the environment affects all K_α emission lines and their different satellite lines [15, 13, 16]. In Fig. 5.1a shows the 6 single K_α emission lines including ground state, 3d excited states and 4s excited states with fine structure. We see the strongest peak coming from the ground state of Si^{13+}. The emission energy of K_α of ground state has a higher intensity than excited states. In Fig. 5.1b we compare this spectrum with experimental data from [13]. Comparing the line shapes we obtained a good agreement of theoretical and experimental data. Both spectra show a double peak structure due the fine splitting components. Fine structure $P_{3/2}$ and $P_{1/2}$ influence the intensity and peak position. Si spectra (T =30 eV) has a red shift comparing with cold Si K_α experiment (T $\sim$ 1 eV).

Let us now investigate $K_\alpha L^0 M^0$ 4 electrons are in the outer shell (M-shell), see Tab. A.6. $K_\alpha L^N M^4$ has no electrons in the outer shell (M-shell), see Tab. A.7. The M-shell is fully ionized. Each additional L-shell hole leads to a rather large line shift to higher energies since core screening is reduced massively.

The $K_\alpha L^N M^0$ and $K_\alpha L^N M^4$ spectrum are shown in the Fig. 5.2a and Fig. 5.2b. Going to Fig. 5.2a $K_\alpha L^N M^0$ with holes (N =0,1,2,3,4) in the full vacancies M shell in the logarithmic scaling. The intensity is strongest in $K_\alpha L^0$ decreases with holes in the L shell. With increasing number of holes reduces the intensity and the peak shifts to the right side because the blue shift effect is stronger in the plasma. Because depending
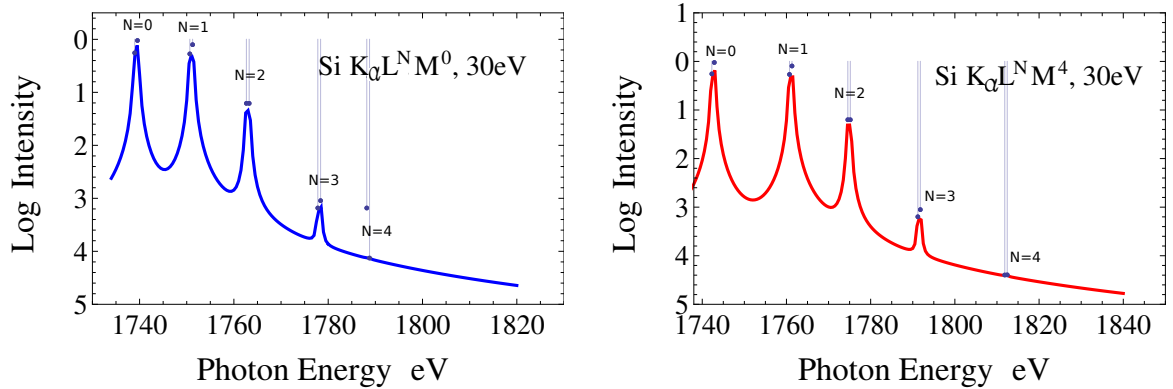
(a) Si $K_\alpha L^N M^0$ ($N = 0,1,2,3,4$) with full vacancies on M shell and x holes in the L shell at temperature 30 eV. The peak of emission energy in 1740 eV is $K_\alpha L^0 M^0$, the peak of emission energy in 1755 eV is $K_\alpha L^1 M^0$, ... and the peak of emission energy in 1780 eV is $K_\alpha L^4 M^0$. Through increasing holes in the L shell shift the peak to the right side of increasing K_α emission energy.

(b) Si $K_\alpha L^N M^4$ ($N = 0,1,2,3,4$) with 4 occupied electrons in the shell and x holes in the L shell at temperature 30 eV. The peak of emission energy in 1743 eV is $K_\alpha L^0 M^4$, the peak of emission energy in 1760 eV is $K_\alpha L^1 M^0$, ... and the peak of emission energy in 1812 eV is $K_\alpha L^4 M^0$. Through increasing holes in the L shell shift the peak to the right side of increasing K_α emission energy.

Figure 5.2.: Si spectrum with satellite emission lines.

the law of mass action $K_\alpha L^0 M^4$ has a stronger contribution than $K_\alpha L^1 M^4$ and so on in $K_\alpha L^N$ satellites. At a fixed density of free electrons for the red shift decreases with increasing temperature. The Fig. 5.3 shows a spectrum with all $K_\alpha L^N M^4$ and $K_\alpha L^N M^0$ component spectrum in logarithmic scale with different holes in L shells in the 30 eV temperature. Compared with the experimental results from [13] where the plasma is generated by intense heavy ion beams, we calculated a spectrum that qualitatively resamples the satellite lines created by the different dynamic collision processes in the target. To also obtain quantitative results the various plasma conditions created along the heavy ion path and integrated in the experimental spectrum have to be considered in the calculation.

5.4. Argon Spectra

Argon has atomic number 18, 8 outer electrons are in the M shell and solid density $2.63 \cdot 10^{22}$ cm^{-3}. Argon plasma was produced with irradiating individual argon droplets of 20 μm diameters with the laser pulse energy of 2.5J [9]. The spectrometer covered the range of the Ar K-shell emission from 2950 eV to 3100 eV, see in Fig. 1.9. In the Ar spectra experiment for the charge states 1+ to 9+ is about 20-30 eV apart and the charge states 10+ ... 14+ is about 20-30 eV apart. The spectrometer covered the Ar K-shell emission range and hydrogen-like argon [9].

In 2012, P. Neumayer *et al.* [9] have measured the PHELIX Laser power 2.5 J through in an argon droplet of 20 μm diameter recording in X-rays spectra emitted lines at the
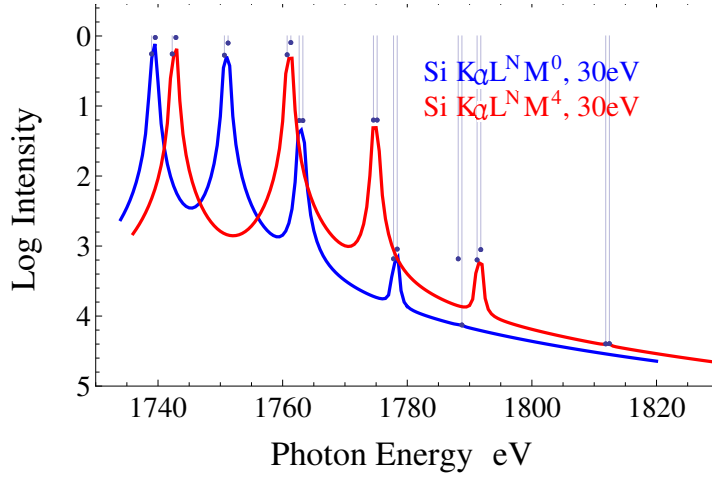
Figure 5.3.: Comparing theoretical Si $K_\alpha L^0 M^4$ (red line) with $K_\alpha L^0 M^0$ (blue line) emission energies (shifted by plasma) at the temperature of 30 eV. $K_\alpha L^0 M^4$ (red line) have more large emission energies than $K_\alpha L^0 M^0$ (blue line) emission energies because $K_\alpha L^0 M^0$ have more strong plasma screening effect.

GSI Helmholtz Center, see Fig. 1.9 and they were using the theoretical code FLYCHK fitting the series of K_α emission spectral lines [9] . The Lorentzians are summed up and convoluted with a Gaussian profile of width Γ to take into account instrumental broadening of measurements. The experimental Ar spectra were convoluted with instrument function (FWHM 7 eV) and the temperature of spectral fitting up to 160 eV [9]. We use Ar instrumental Gaussian width $\Gamma = 7$ eV in Gaussian profile convoluted the Lorentz profile with Lorentzian linewidth $\gamma = 1$ eV including the emission energies of excited states (3s, 3p, 3d, and 4s). Our K_α series emission spectrum lines from temperature 10 eV to 170 eV in Fig. 5.4. We saw the Ar spectra in 10 eV having main contributions in the ion charge state $Ar^{1+\cdots9+}$ corresponding the same configuration of initial state $1s^1 2s^2 2p^6$ and less contributions in the ion charge state from 10^+ of the initial state $1s^1 2s^2 2p^5$, 11^+ of the initial state $1s^1 2s^2 2p^4$, 12^+ of the initial state $1s^1 2s^2 2p^4$,12^+ of the initial state $1s^1 2s^2 2p^3$, 13^+ of the initial state $1s^1 2s^2 2p^2$ and 14^+ of the initial state $1s^1 2s^2 2p^1$. Temperature 10 eV, 20 eV, 30 eV ,40eV and 50eV contribute strongly to K_α peak of $Ar^{1+\cdots9+}$ in the range of emission energy 2950 eV to 2975 eV. Seeing Fig. 4.3b can correspond to the Ar plasma charge states in the different temperature. Ar spectra of temperature 60 eV has beginning large contribution in Ar^{10+} and 80 eV has beginning large contribution in Ar^{11+} and Ar^{12+} the two peaks are very close. Ar spectra of temperature 110 eV has beginning contribution in Ar^{13+} and Ar^{14+}. At the higher temperature 150 eV, 160 eV and 170 eV have a more larger contribution at Ar^{14+}. Focus on the temperature 110 eV shows the K_α peak $Ar^{1+\cdots9+}$ the energy range from 2950 eV to 2970 eV, Ar^{10+} from 2980 eV to 3000 eV, Ar^{11+} from 3000 eV to 3020 eV, Ar^{12+} from 3015 eV to 3030 eV, Ar^{13+} from 3040 eV to 3060 eV and Ar^{14+} from 3070 eV to 3090 eV. At temperature 10 eV shows the peak around the 2958 eV good fitting cold plasma with low density K_α because the red shift on plasma screening is very weak. In Fig. 5.4

we could not separate the fine structure splitting of Ar that K_α is 2.01 eV of K_{α_1} and K_{α_2}.

5.5. Optimal Temperature Distributions to Reproduce Experimental Spectra of Ar

We use the statistical χ^2 testing [53] comparing our argon theoretical spectra with experiment spectra. The chi-square statistic is computed by the sum of the observed values (theoretical values) minus the expected values (experimental values) squared divided by the absolute expected values (experimental values) writing as

$$\chi^2 = \sum_E \frac{(I_{theo}(E) - I_{exp}(E))^2}{|I_{exp}(E)|}. \tag{5.19}$$

The Eq. (5.19) shows $\chi^2 = 0$ meaning each theoretical intensity of energy equal to the experimental intensity of energy $I_{theo}(E) = I_{exp}(E)$ and the theoretical values are totally fully fitting experiment values. Increasing the χ^2 values means more discrepancy of theoretical intensity and experimental intensity. The theoretical spectra from Fig. 5.4 are normalized. We read the experiment spectra data from [9] and normalize the experiment spectra. In Fig. 5.5a combines the normalized theoretical spectra (blue curve) with the Ar weights of the spectra from 10 eV to 160 eV from Fig. 5.5b and experimental spectra (red curve) getting $\chi^2 = 0.51$. The $Ar^{1+\cdots9+}$ has a larger theoretical FWHM than experimental FWHM. We calculate the constant weights temperature distribution theoretical spectra from Fig. 5.4 then we compare our the experimental spectra with experimental spectra in Fig. 5.6a getting $\chi^2 = 1.2$. Fig. 5.6b we use the weights of temperature distribution (using FLYCHK) from [9] theoretical spectra from Fig. 5.4 then we compare our experimental spectra with spectra getting $\chi^2 = 1.58$. Comparing the χ^2 from Fig. 5.5a, Fig. 5.6a and Fig. 5.6b we know the weights of temperatures is well in Fig. 5.5b then normal weights. And the weight of temperature distribution (using FLYCHK) from [9] is not the best suitable in our theoretical spectra. For good fitting the $Ar^{1+\cdots9+}$ we take the Lorentzian linewidth $\gamma = 1$ eV convoluted small instrumental Gaussian width $\Gamma = 3$ eV. The Fig. 5.7a we calculate Ar spectra with the Ar weights of the spectra from 10 eV to 160 eV from Fig. 5.7b besser fitting with $\chi^2 = 0.34$ then instrumental Gaussian width $\Gamma = 7$ eV at K_α of $Ar^{1+\cdots9+}$ with experiment curve. We compare the Ar^{12+}, Ar^{13+} and Ar^{14+} with experiment getting the theoretical peaks shift in the right side of experiment peaks, see Fig. 4.3b the charge state of Ar^{13+} and Ar^{14+} corresponding to high temperature (more than 150 eV). The Fig. 5.7b weight distribution has a stronger contribution on the temperature 20 eV, 30 eV, 150 eV and 160 eV. But the weight distribution in [9] has a stronger contribution on the temperature 50 eV, 60 eV, 150 eV and 160 eV. The Fig. 5.8a we calculate the same weight on the spectra temperature distribution getting $\chi^2 = 0.54$. The Fig. 5.8b we calculate the weight from [9] on the spectral temperature distribution getting $\chi^2 = 0.61$ and showing the $Ar^{1+\cdots9+}$ is shifted to the right side of the spectral spectrum the Ar^{10+} Ar^{11+}, Ar^{10+} with

Ar^{11+} having large intensity than experiment. We calculate the different temperature distribution of weights helping understand the experiment process. The Fig. 5.9 we compare these three different spectra and we find the Ar^{10+} Ar^{11+}, Ar^{12+} , Ar^{13+} and Ar^{14+} the peak position not different but $Ar^{1+\cdots9+}$ the peak position is very different.

In Fig. 5.10 Ar spectra of temperature with instrumental Gaussian width Γ is 3 eV and Lorentzian linewidth γ is 1 eV. Comparing with the $K_\alpha^{1+\cdots9+}$ getting chi-square is 0.055. The Fig. 5.10 we calculate the K_α on the temperature 30 eV our theoretical peak shifting right to experimental peak. We calculate the different temperatures 25 eV, 27 eV, 28 eV and 30 eV to find the well experiment peak at the specific temperature, see Fig. 5.11.

We apply a superposition of our spectra for different temperatures to model the experimental results obtained by Neumayer *et al.* [9]. To obtain the best fit the weight of the different spectra is determined within a variational approach using the method of least squares. Results for the best fit and the corresponding temperature distribution are shown in Fig. 5.12 and Fig. 5.13, respectively.

The superimposed spectrum shows a good agreement especially for the M-shell satellites. Since the position of the main peak is rather sensitive to temperature we chose not only a 10 eV grid but inserted some intermediate temperatures between 20 eV and 30 eV. At a first glimpse the agreement with the L-shell satellites is less satisfying. The peaks are at correct positions but the widths seem to small. We attribute this to our approximation of the natural line widths. We use only one value for γ which implies the same lifetime for all considered states. But especially highly ionized and excited states experience shorter lifetimes and hence show a larger natural width. Accordingly the L-shell emission lines would blur and give a better fit of the energy spectrum above 2980 eV.
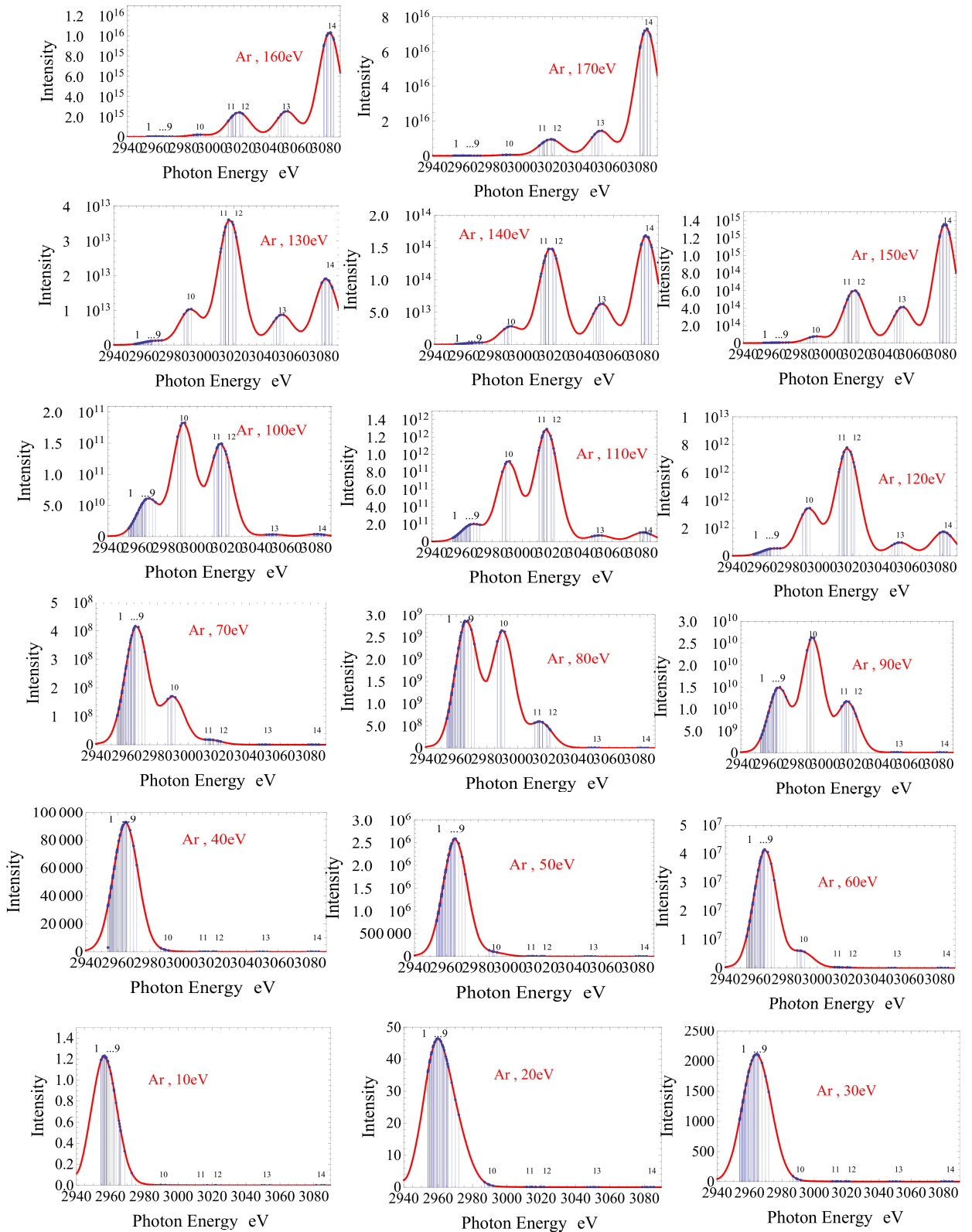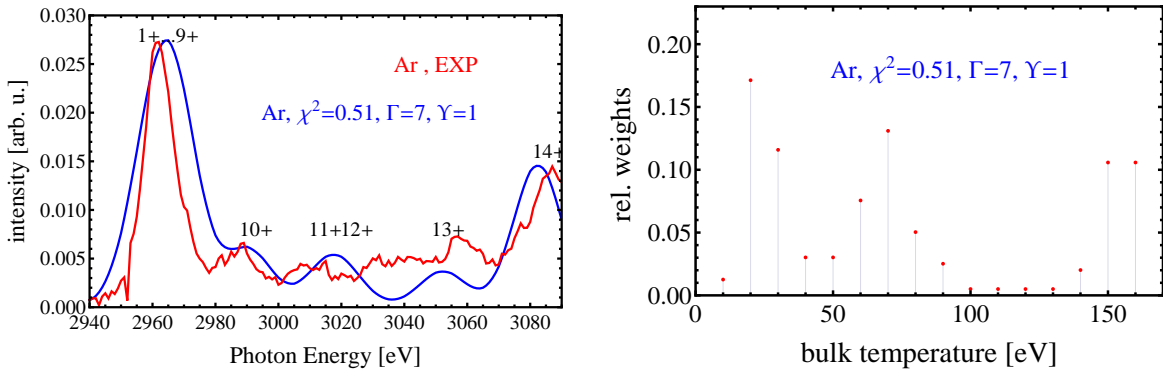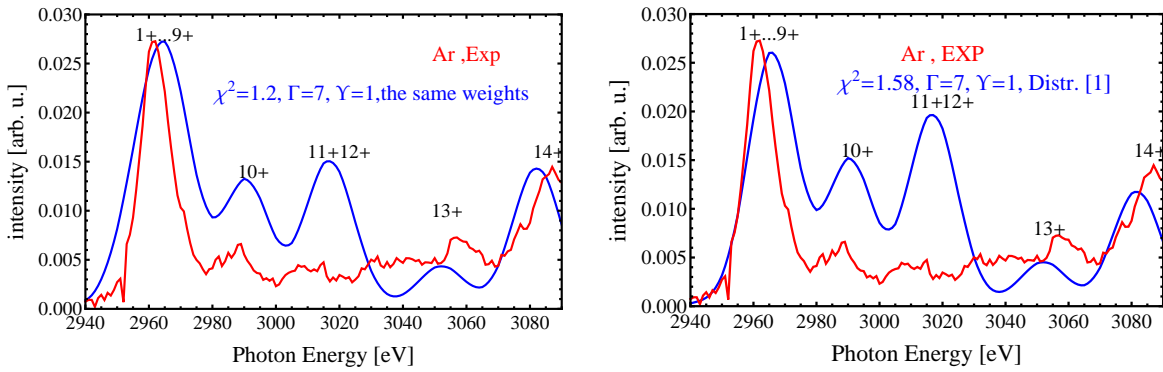
Figure 5.4.: Ar instrumental Gaussian width Γ is 7 eV and Lorentzian linewidth γ is 1 eV from temperature T=10 eV to T=170 eV emission energies with different charge states.

(a) Ar spectra with KL transitions of different charge states. Instrumental Gaussian width Γ is 7 eV and Lorentzian linewidth γ is 1 eV. Using chi-square test compare spectra (blue curve) with experimental values (red curve).

(b) Ar Weights of spectra from (a) blue curve at different temperatures from 10 eV to 160 eV.

Figure 5.5.: (b) is the weights to obtain the (a) Ar spectra comparing experiment curve chi-square is 0.51.

(a) Ar spectra with KL transitions of different charge states. Instrumental Gaussian width Γ is 7 eV and Lorentzian linewidth γ is 1 eV with the same weights of temperatures (from 10 eV to 160 eV). Using chi-square test compare spectra (blue curve) with experimental values (red curve).

(b) Ar spectra with KL transitions of different charge states. Instrumental Gaussian width Γ is 7 eV and Lorentzian linewidth γ is 1 eV. with the weight distribution of temperatures (from 10 eV to 160 eV) [9]. Using chi-square test compare spectra (blue curve) with experimental values (red curve).

Figure 5.6.: Using the same weights to obtain the (a) Ar spectra comparing experiment curve chi-square is 1.2. Using the weights [9] to obtain the (b) Ar spectra comparing experiment curve chi-square is 1.58.

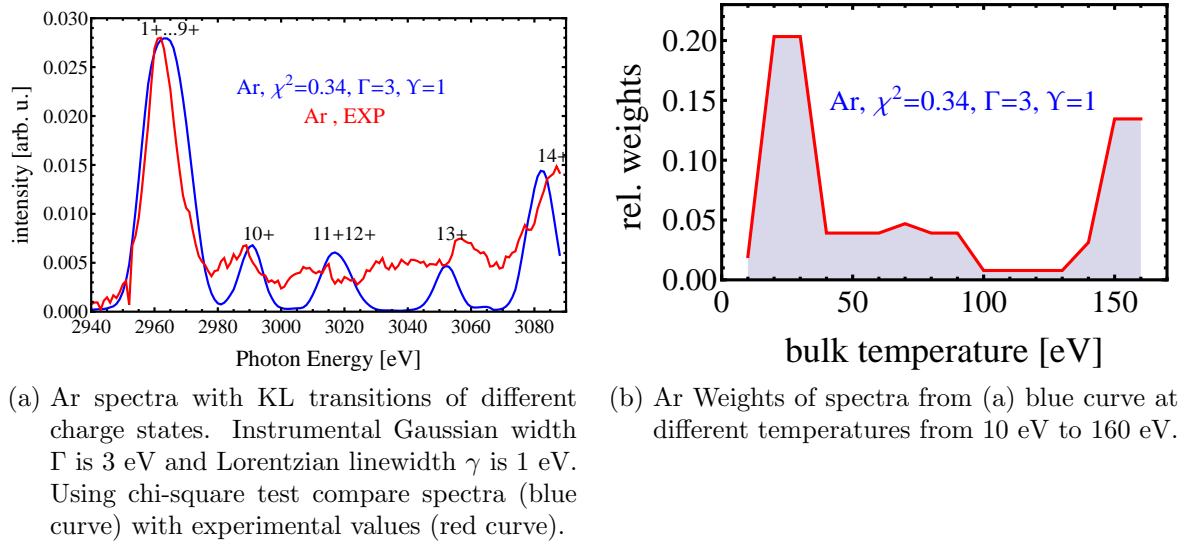(a) Ar spectra with KL transitions of different charge states. Instrumental Gaussian width Γ is 3 eV and Lorentzian linewidth γ is 1 eV. Using chi-square test compare spectra (blue curve) with experimental values (red curve).

(b) Ar Weights of spectra from (a) blue curve at different temperatures from 10 eV to 160 eV.

Figure 5.7.: (b) is the weights to obtain the (a) Ar spectra comparing experiment curve chi-square is 0.34.

(a) Ar spectra with KL transitions of different charge states. Instrumental Gaussian width Γ is 3 eV and Lorentzian linewidth γ is 1 eV with the same weights of temperatures (from 10 eV to 160 eV). Using chi-square test compare spectra (blue curve) with experimental values (red curve).

(b) Ar spectra with KL transitions of different charge states. Instrumental Gaussian width Γ is 3 eV and Lorentzian linewidth γ is 1 eV. with the weight distribution of temperatures (from 10 eV to 160 eV) [9]. Using chi-square test compare spectra (blue curve) with experimental values (red curve).
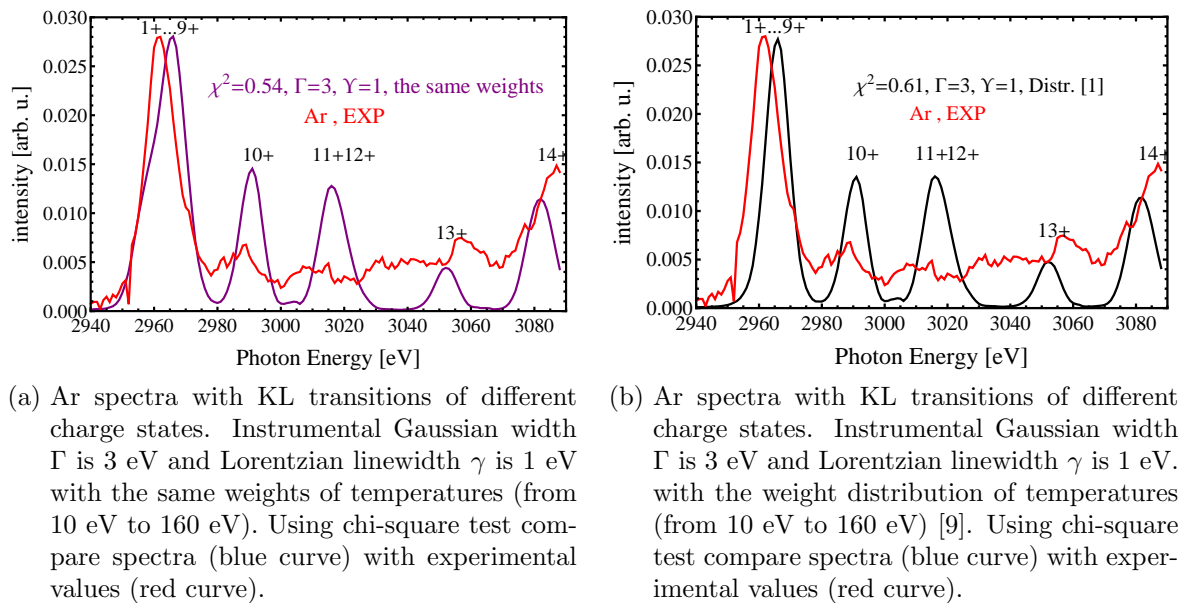
Figure 5.8.: Using the same weights to obtain the (a) Ar spectra comparing experiment curve chi-square is 0.54. Using the weights [9] to obtain the (b) Ar spectra comparing experiment curve chi-square is 0.61.
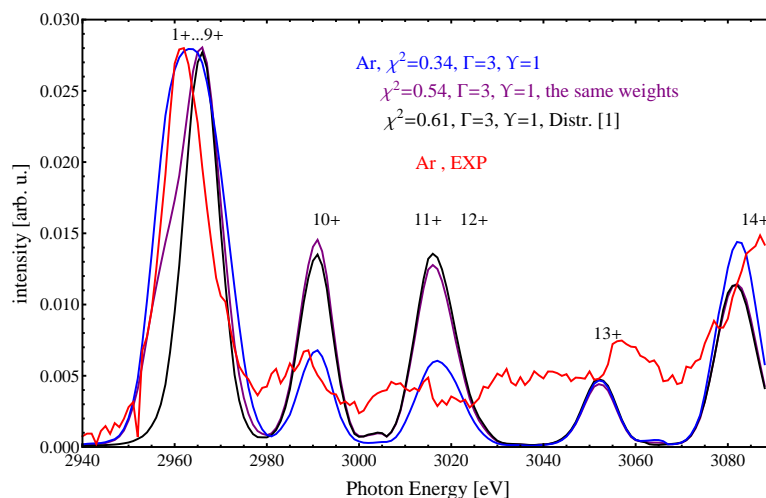
Figure 5.9.: Comparing with all of the different weight distribution with experimental values. Ar spectra with KL transitions of different charge states. Instrumental Gaussian width Γ is 3 eV and Lorentzian linewidth γ is 1 eV with the same weights of temperatures (from 10 eV to 160 eV).
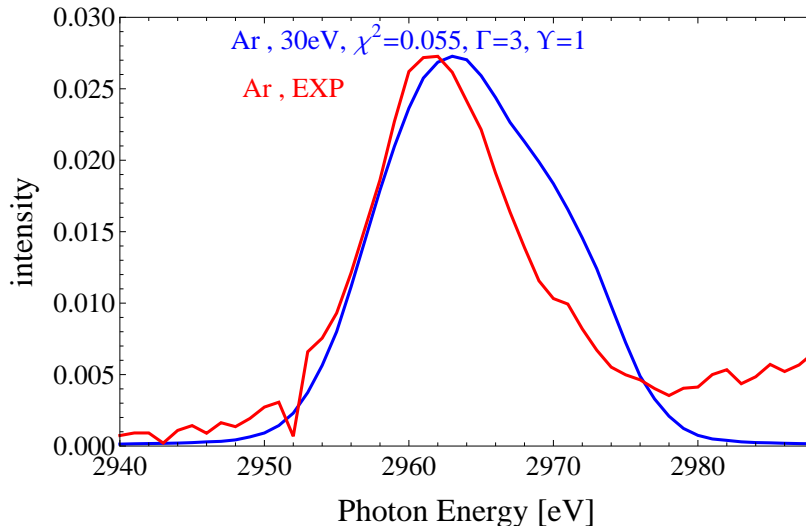
Figure 5.10.: Ar spectra of temperature with instrumental Gaussian width Γ is 3 eV and Lorentzian linewidth γ is 1 eV. Comparing with the $K_\alpha^{1+\cdots9+}$ getting chi-square is 0.055
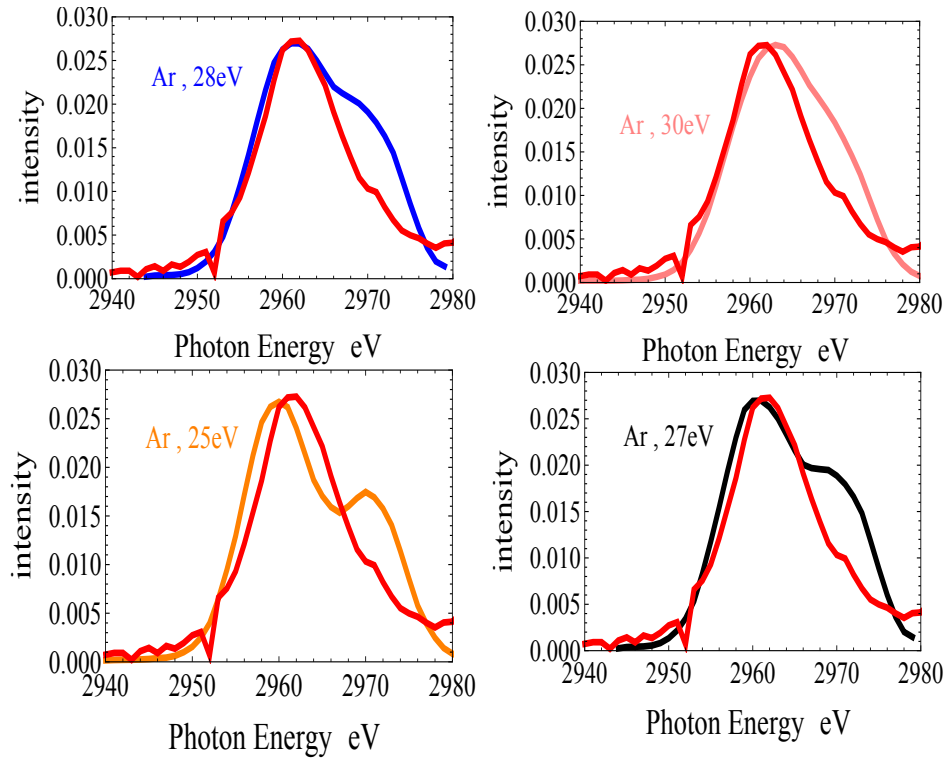
Figure 5.11.: Ar spectra of temperature with instrumental Gaussian width Γ is 3 eV and Lorentzian linewidth γ is 1 eV on the temperature 25 eV, 27 eV, 28 eV and 30 eV.

Figure 5.12.: Best fit of superposition of theoretical spectra and space-time-integrated measurements of Neumayer *et al.* [9].

Figure 5.13.: Temperature distribution which gives the best fit of theoretical and experimental spectra. The relative weights are determined via the method of least squares.

6. Conclusions

K_α X-ray emissions strongly depend on the ion configuration and emitter environment. Red energy shifts are caused by plasma environment. They are stronger with higher free electron density and increasing temperature. Blue ene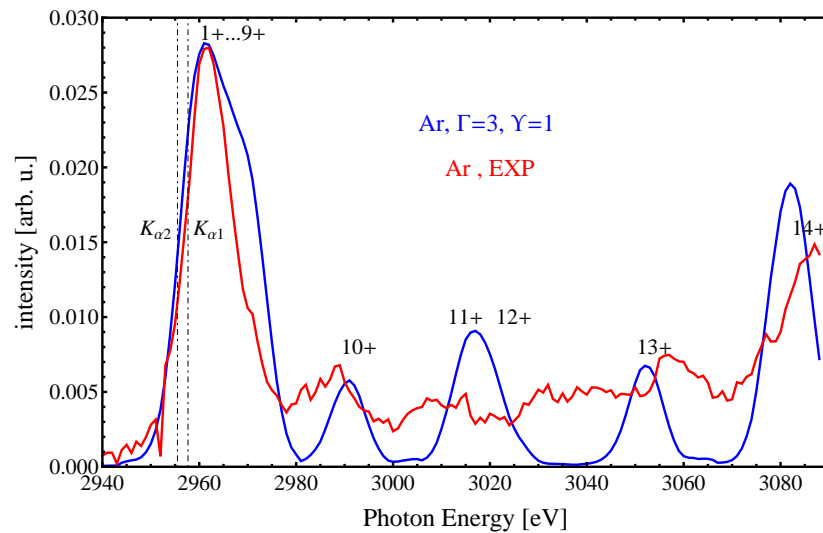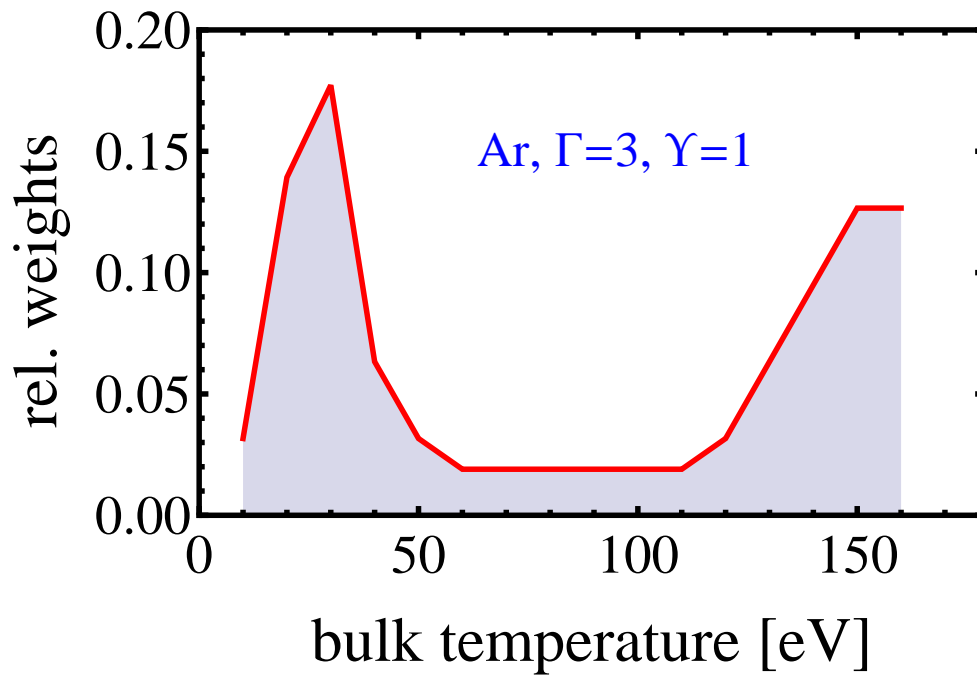rgy shifts are due to different emitter configurations. In the high temperature plasma has the same screening effect on Debye Hückel and Montroll-Ward model, because the higher order self energy in the Montroll-Ward has less contribution in the higher temperatures. Assume the quantum dipole transition is one point in the classical case for calculating high temperature plasma. Using Plank-Larkin renormalization to the bound state systems of ions of Si for the k-th ionization stage we solved the continuum problem (Mott effect) in the classical case. For the different temperature Si K_α or satellite lines we discuss the plasma effect depending on temperature.

Red energy shifts in Ar are depending on the free electron density and temperature , see Fig. 5.4 showing T=10 eV has smaller red shift than T=170 eV corresponding experiment [9] peak position. Wave functions as well as energy values were calculated using the ab initio G03 code Aug-cc-pVTZ basis set, see Fig. 2.9. The plasma effect was considered within a perturbative approach by the Ion Sphere model and we use the Planck-Larkin sum of bound states at continuous ionization. We presented synthetic spectra that are able to resemble emissions from various L-and M-shell configurations. We compare our plasma composition with FLYCHK, see Fig. 4.3b. Fig. 4.1 and Fig. 4.2 show the plasma composition depending on temperature. Fig. 5.4 shows our spectral lines with temperature from 10 eV to 170 eV getting the fitting with experiment [9] in Fig. 5.10.

In section 5.5 we use the statistical χ^2 testing [53] comparing our argon theoretical spectra with experiment spectra to fit test experimental data and theoretical data.

The Lorentzians are summed up and convoluted with a Gaussian profile of width Γ to take into account instrumental broadening of measurements. The experimental Ar spectra were convoluted with instrument function (FWHM 7 eV) and the temperature of spectral fitting up to 160 eV [9]. We use Ar instrumental Gaussian width $\Gamma = 7$ eV in Gaussian profile convoluted the Lorentz profile with Lorentzian linewidth $\gamma = 1$ eV including the emission energies of excited states (3s, 3p, 3d, and 4s). Our K_α series emission spectrum lines from temperature 10 eV to 170 eV in Fig. 5.4. The temperature distribution we obtain is similar to the theoretical results of Neumayer *et al.*[9]: a two-peaked curve with the first focus at lower temperatures of some 10 eV, the second focus at more than 100 eV higher temperatures and a less pronounced region in between. However, there is a significant difference between the distribution of Neumayer *et al.* and the results shown here: our first focus lies at about 20 eV lower plasma temperature. This difference is due to the different results of the composition calculations. The Fig.

5.12 results for undisturbed peak positions are rather the same, showing blue shifted emission energies as described above. But as we obtain higher degrees of ionization at lower temperatures, we also see the blue shift of emission energies at lower temperatures and hence we obtain a temperature of about 25 eV instead of 50 eV to fit the main peak of the measured spectrum. Neumayer *et al.* discussed several mechanisms like resistive heating or radiative heating that might help to explain the absence of temperatures below 50 eV. However, our results suggest that these influences might not be as substantial as the authors assumed. Further, the broadening of the lines is different in both approaches. Using our parameter values for the broadening of all lines in general gives a too large width for the main peak (Ar^+ to Ar^{9+}) and a too small width for the higher lying peaks. A more detailed discussion of the width would improve the agreement between theory and experimental data. In particular, the low minima between the theoretical peaks will be possibly smeared out. A quantum statistical approach to the line width would be desirable. This kind off approaches are well elaborated for H-like systems but need further development for mid-Z materials.

The inclusion of plasma effects, especially shifts and the merging of bound states with the continuum, is important to discuss the composition of the plasma and the density of free electrons. We have shown that such effects have significant influence on the inferred temperature distribution. In the present work we did not attempt to describe the origin of the inferred temperature profile. For this purpose kinetic codes and hydrodynamic simulations are inevitable. In general, K-alpha spectroscopy is an interesting means of plasma diagnostic and gives a rough profile of the temperature distribution which can be made even more precisely in future calculations. We will consider also higher densities of the plasma, the effects of dynamical collisions with the plasma electrons and the fluctuations of the ionic microfield on the line shifts and widths have to be considered.

Acknowledgements

A. Appendix

A.1. Atomic Units [a.u.] and Some Constants

Electron mass : $m_e = 1$
Elementary charge : $e = 1$
Reduced Planck's constant : $\hbar = h/2\pi = 1$
Coulomb's constant : $c = 1/(4\pi\epsilon_0) = 1$
Bohr radius: $a_0 = 5.29177249 \times 10^{-9}$ cm
Hartree energy: $E_h = 27.2113961$ eV
Electric constant: $\epsilon_0 = 1/(4\pi)$

A.2. Gaussian Basis Functions for Si

orbital	Function	orbital	Function	orbital	Function
1S	$\sum_{i=1}^{3} d_{1s,i} e^{-\alpha_{1,i} r^2}$	3PX	$\sum_{i=1}^{2} d_{3p,i} x e^{-\alpha_{3,i} r^2}$	4PZ	$d_{4p} z e^{-\alpha_4 r^2}$
2S	$\sum_{i=1}^{3} d_{2s,i} e^{-\alpha_{2,i} r^2}$	3PY	$\sum_{i=1}^{2} d_{3p,i} y e^{-\alpha_{3,i} r^2}$	5XX	$d_{5d} x^2 e^{-\alpha_5 r^2}$
2PX	$\sum_{i=1}^{3} d_{2p,i} x e^{-\alpha_{2,i} r^2}$	3PZ	$\sum_{i=1}^{2} d_{3p,i} z e^{-\alpha_{3,i} r^2}$	5YY	$d_{5d} y^2 e^{-\alpha_5 r^2}$
2PY	$\sum_{i=1}^{3} d_{2p,i} y e^{-\alpha_{2,i} r^2}$	4S	$d_{4s} e^{-\alpha_4 r^2}$	5ZZ	$d_{5d} z^2 e^{-\alpha_5 r^2}$
2PZ	$\sum_{i=1}^{3} d_{2p,i} z e^{-\alpha_{2,i} r^2}$	4PX	$d_{4p} x e^{-\alpha_4 r^2}$	5XY	$d_{5d} xy e^{-\alpha_5 r^2}$
3S	$\sum_{i=1}^{2} d_{3s,i} e^{-\alpha_{3,i} r^2}$	4PY	$d_{4p} y e^{-\alpha_4 r^2}$	5XZ	$d_{5d} xz e^{-\alpha_5 r^2}$
				5YZ	$d_{5d} yz e^{-\alpha_5 r^2}$

Table A.1.: 3-21G* Basis Functions for Si.

A. Appendix

i	$\alpha_{1,i}$	$d_{1s,i}$	$\alpha_{2,i}$	$d_{2s,i}$
1	0.9106550D+03	0.6608223959D-01	0.3667160000D+02	-0.1045110359D+00
2	0.1373360D+03	0.3862286469D+00	0.8317290000D+01	0.1074100369D+00
3	0.2976010D+02	0.6723793854D+00	0.2216450000D+01	0.9514463269D+00
i	$d_{2p,i}$	$\alpha_{3,i}$	$d_{3s,i}$	$d_{3p.i}$
1	0.1133550147D+00	0.1079130000D+01	-0.3761078795D+00	0.6710299112D-01
2	0.4575780593D+00	0.3024220000D+00	0.1251649599D+01	0.9568828734D+00
3	0.6074270787D+00			
i	$\alpha_{4,i}$	$d_{4s,i}$	$d_{4p,i}$	$\alpha_{5,i}$
1	0.9333920000D-01	0.1000000000D+01	0.1000000000D+01	0.4500000000D+00
i	$d_{5d,i}$			
1	0.1000000000D+01			

Table A.2.: 3-21G* Basis Functions for Si α and d parameters.

a.o. -68.38198	-6.13038	-4.23246	-4.23246	-4.22298
-0.61378	-0.29721	-0.29721		
a.v. -0.00079	0.40910	0.48446	0.48446	0.51608
0.76469	0.76469	0.78291	0.78291	0.79023
2.56061				
b.o. -68.37305	-6.11987	-4.21881	-4.20513	-4.20513
-0.45658				
b.v. 0.03117	0.07314	0.07314	0.44928	0.52977
0.56696	0.56696	0.83751	0.84796	0.84796
0.88425	0.88425	2.58575		

Table A.3.: 3-21G* beta eigenvalues (occupied orbits and virtual orbits).

a.o.	-68.89543	-6.17381	-4.28959	-4.28959	-4.27877
	-0.61618	-0.29263	-0.29263		
a.v.	-0.01454	0.06490	0.07066	0.07066	0.08130
	0.14772	0.14772	0.15018	0.15018	0.15085
	0.43771	0.43771	0.43998	0.43998	0.44773
	0.44773	0.45123	0.45926	0.46197	0.48562
	0.48579	0.48579	0.48878	0.48878	0.49472
	0.49472	1.27501	1.27745	1.27745	1.28519
	1.28519	1.42418	1.42597	1.42597	1.43135
	1.43135	1.44033	1.44033	2.49289	2.49289
	2.49701	2.53851			
b.o.	-68.88471	-6.16129	-4.27314	-4.25828	-4.25828
	-0.46156				
b.v.	0.01197	0.03411	0.03411	0.07596	0.09259
	0.11367	0.11367	0.16327	0.16623	0.16623
	0.17646	0.17646	0.47454	0.48342	0.49689
	0.49689	0.49689	0.49689	0.49819	0.49920
	0.50733	0.50733	0.50997	0.50997	0.52066
	0.52066	0.52261	0.52261	1.29865	1.30737
	1.30737	1.33527	1.33527	1.45040	1.45503
	1.45503	1.46904	1.46904	1.49305	1.49305
	2.50805	2.53917	2.53917	2.56279	

Table A.4.: 8 alpha occupied eigenvalues (a.o.) and 42 alpha virtual eigenvalues (a.v.) and 6 beta occupied eigenvalues (b.o.)and 44 beta virtual eigenvalues (b.v.) in Aug-cc-PVTZ.

A.3. Coulomb Potential

The many particles system is described by Hamiltonian,

$$H = \sum_{i=1}^{N} \frac{p_i^2}{2m} + \sum_{i<j} V(\mathbf{r_i} - \mathbf{r_j}). \tag{A.1}$$

The coulomb interaction potential

$$V(\mathbf{q}) = \frac{1}{\Omega} \int d^3 r\, e^{i\mathbf{qr}} V(\mathbf{r}). \tag{A.2}$$

$$V(\mathbf{q}, i\omega_\lambda)$$

$$\dashrightarrow$$

We consider the coulomb interaction at local in time and the interaction has no dispersive with spin conserving in coordinate space. k is wave number and σ is spin.

$$V(12, 1'2') = V(\mathbf{k_1 k_2}, \mathbf{k_{1'} k_{2'}}) \delta_{\sigma_1 \sigma_{1'}} \delta_{\sigma_2 \sigma_{2'}}. \tag{A.3}$$

Using Fourier transform $\langle r|k \rangle = \frac{1}{\sqrt{\Omega}} e^{i\mathbf{kr}}$ and ortho-normality relation $\langle \mathbf{r_1 r_2}|\mathbf{r_{1'} r_{2'}} \rangle = \delta^3(\mathbf{r_1} - \mathbf{r_{1'}})\delta^3(\mathbf{r_2} - \mathbf{r_{2'}})$. The coulomb potential $V(\mathbf{k_1 k_2}, \mathbf{k_{1'} k_{2'}}) = \langle k_{1'} k_{2'}|k_1 k_2 \rangle$ can expand

$$V(\mathbf{k_1 k_2}, \mathbf{k_{1'} k_{2'}}) = \sum_{\mathbf{r_{1'}}} \sum_{\mathbf{r_{2'}}} \sum_{\mathbf{r_1}} \sum_{\mathbf{r_2}} \langle k_{1'}|\mathbf{r_{1'}} \rangle \langle k_{2'}|\mathbf{r_{2'}} \rangle \langle \mathbf{r_1' r_2'}|V|\mathbf{r_1 r_2} \rangle \langle \mathbf{r_1}|k_1 \rangle \langle \mathbf{r_2}|k_2 \rangle. \tag{A.4}$$

$$V(\mathbf{k_1 k_2}, \mathbf{k_{1'} k_{2'}}) = \left(\frac{1}{\Omega}\right)^2 \int d^3 \mathbf{r_1} \int d^3 \mathbf{r_2} \int d^3 \mathbf{r_{1'}} \int d^3 \mathbf{r_{2'}}\, e^{-i\mathbf{k_{1'} r_{1'}}} e^{-i\mathbf{k_{2'} r_{2'}}}$$
$$\cdot \frac{e_1 e_2}{4\pi\epsilon_0 |\mathbf{r_1} - \mathbf{r_2}|} \delta^3(\mathbf{r_1} - \mathbf{r_{1'}})\delta^3(\mathbf{r_2} - \mathbf{r_{2'}}) e^{i\mathbf{k_1 r_1}} e^{i\mathbf{k_2 r_2}}.$$

$$V(\mathbf{k_1 k_2}, \mathbf{k_{1'} k_{2'}}) = \left(\frac{1}{\Omega}\right)^2 \int d^3 \mathbf{r_1} \int d^3 \mathbf{r_2}\, e^{-i\mathbf{k_{1'} r_1}} e^{-i\mathbf{k_{2'} r_2}} \frac{e_1 e_2}{4\pi\epsilon_0 |\mathbf{r_1} - \mathbf{r_2}|} e^{i\mathbf{k_1 r_1}} e^{i\mathbf{k_2 r_2}} \tag{A.5}$$

$$= \left(\frac{1}{\Omega}\right)^2 \int d^3 \mathbf{r_1} \int d^3 \mathbf{r_2}\, e^{i(\mathbf{k_1} - \mathbf{k_{1'}})\mathbf{r_1}} e^{i(\mathbf{k_2} - \mathbf{k_{2'}})\mathbf{r_2}} \frac{e_1 e_2}{4\pi\epsilon_0 |\mathbf{r_1} - \mathbf{r_2}|}. \tag{A.6}$$

In homogeneity space consider coulomb potential depends on the relative vector between the interacting particles. Let relative coordinate is $\mathbf{r_{rel}} = \rho = \mathbf{r_1} - \mathbf{r_2}$.

$$V = \left(\frac{1}{\Omega}\right)^2 \int d^3(\mathbf{r_1} - \mathbf{r_2}) e^{i(\mathbf{k_1} - \mathbf{k_{1'}})(\mathbf{r_1} - \mathbf{r_2})} \frac{e_1 e_2}{4\pi\epsilon_0 |\mathbf{r_1} - \mathbf{r_2}|} \int d^3 \mathbf{r_2} e^{i(\mathbf{k_1} - \mathbf{k_{1'}} + \mathbf{k_2} - \mathbf{k_{2'}})\mathbf{r_2}}. \tag{A.7}$$

Using $\widetilde{\delta}(\mathbf{k}) = \frac{1}{2\pi}\int_{-\infty}^{\infty} dxe^{i\mathbf{k}\cdot\mathbf{x}}$ to get

$$\widetilde{\delta}(\mathbf{k_1} - \mathbf{k_{1'}} + \mathbf{k_2} - \mathbf{k_{2'}}) = \left(\frac{1}{2\pi}\right)^3 \int_{-\infty}^{\infty} d^3\mathbf{r_2} e^{i(\mathbf{k_1}-\mathbf{k_{1'}}+\mathbf{k_2}-\mathbf{k_{2'}})r_2} \tag{A.8}$$

from discontinuing space to continuing space $\sum \to \int d^3\mathbf{r_2} = \frac{8\pi^3}{\Omega}$.

So $\int d^3\mathbf{r_2}e^{i(\mathbf{k_1}-\mathbf{k_{1'}}+\mathbf{k_2}-\mathbf{k_{2'}})r_2} = \Omega\delta(\mathbf{k_1} - \mathbf{k_{1'}} + \mathbf{k_2} - \mathbf{k_{2'}})$. We can use a spherical coordinate system to solve the first part $\int d^3\mathbf{r_2}e^{i(\mathbf{k_1}-\mathbf{k_{1'}}+\mathbf{k_2}-\mathbf{k_{2'}})r_2}$.

$$(1) = \left(\frac{1}{\Omega}\right)^2 \int_{-\infty}^{\infty} d^3\rho e^{i(\mathbf{k_1}-\mathbf{k_{1'}})\cdot\rho}\frac{e_1e_2}{4\pi\epsilon_0\rho}\Omega\delta(\mathbf{k_1} - \mathbf{k_{1'}} + \mathbf{k_2} - \mathbf{k_{2'}}) \tag{A.9}$$

$$= \frac{1}{\Omega}\int_0^{2\pi}\int_0^{\pi}\int_0^{\infty} \rho^2\sin\theta d\theta d\phi e^{i(\mathbf{k_1}-\mathbf{k_{1'}})\rho\cos\theta}\frac{e_1e_2}{4\pi\epsilon_0\rho}\delta(\mathbf{k_1} - \mathbf{k_{1'}} + \mathbf{k_2} - \mathbf{k_{2'}})d\rho \tag{A.10}$$

$$= \frac{e_1e_2}{4\pi\epsilon_0\Omega}2\pi\int_0^{\pi}\int_0^{\infty} \rho\sin\theta d\theta e^{i(\mathbf{k_1}-\mathbf{k_{1'}})\rho\cos\theta}\delta(\mathbf{k_1} - \mathbf{k_{1'}} + \mathbf{k_2} - \mathbf{k_{2'}})d\rho. \tag{A.11}$$

The partial differential equation sets $\cos\theta = z$, $dz = d\cos\theta = -\sin\theta d\theta$ to get

$$V(\mathbf{k_1k_2}, \mathbf{k_{1'}k_{2'}}) = \frac{e_1e_2}{2\epsilon_0\Omega}\int_0^{\infty}\int_0^{\pi} \rho\sin\theta d\theta e^{i(\mathbf{k_1}-\mathbf{k_{1'}})\rho\cos\theta}\delta(\mathbf{k_1} - \mathbf{k_{1'}} + \mathbf{k_2} - \mathbf{k_{2'}})d\rho \tag{A.12}$$

$$= \frac{e_1e_2}{2\epsilon_0\Omega}\int_0^{\infty}\int_{-1}^{1} \rho dze^{i(\mathbf{k_1}-\mathbf{k_{1'}})\rho z}\delta(\mathbf{k_1} - \mathbf{k_{1'}} + \mathbf{k_2} - \mathbf{k_{2'}})d\rho \tag{A.13}$$

The part $\int_{-1}^{1} dze^{i(\mathbf{k_1}-\mathbf{k_{1'}})\rho\mathbf{z}} = \frac{e^{i(\mathbf{k_1}-\mathbf{k_{1'}})\rho z}}{i(\mathbf{k_1}-\mathbf{k_{1'}})}\Big|_{-1}^{1} = \frac{e^{i(\mathbf{k_1}-\mathbf{k_{1'}})\rho}-e^{-i(\mathbf{k_1}-\mathbf{k_{1'}})\rho}}{i(\mathbf{k_1}-\mathbf{k_{1'}})\rho}$. So

$$V(\mathbf{k_1k_2}, \mathbf{k_{1'}k_{2'}}) = \frac{e_1e_2}{2\epsilon_0\Omega}\int_0^{\infty} \frac{e^{i(\mathbf{k_1}-\mathbf{k_{1'}})\rho} - e^{-i(\mathbf{k_1}-\mathbf{k_{1'}})\rho}}{i(\mathbf{k_1}-\mathbf{k_{1'}})}\delta(\mathbf{k_1} - \mathbf{k_{1'}} + \mathbf{k_2} - \mathbf{k_{2'}})d\rho \tag{A.14}$$

$$= \frac{e_1e_2\delta(\mathbf{k_1} - \mathbf{k_{1'}} + \mathbf{k_2} - \mathbf{k_{2'}})}{2\epsilon_0\Omega i(\mathbf{k_1}-\mathbf{k_2})}\int_0^{\infty} e^{i(\mathbf{k_1}-\mathbf{k_{1'}})\rho} - e^{-i(\mathbf{k_1}-\mathbf{k_{1'}})\rho}d\rho. \tag{A.15}$$

Using $\sin(z) = \frac{e^{iz}-e^{-iz}}{2i}$ and $z = (\mathbf{k_1}-\mathbf{k_{1'}})\rho$. The term $\int_0^{\infty} e^{i(\mathbf{k_1}-\mathbf{k_{1'}})\rho} - e^{-i(\mathbf{k_1}-\mathbf{k_{1'}})\rho}d\rho$ reduces to $\int_0^{\infty} 2i\sin(\mathbf{k_1} - \mathbf{k_{1'}})d\rho = \frac{2i}{(\mathbf{k_1}-\mathbf{k_{1'}})}\cos(\mathbf{k_1} - \mathbf{k_{1'}})\rho\Big|_0^{\infty} = \frac{2i}{(\mathbf{k_1}-\mathbf{k_{1'}})}$. The coulomb potential is equal to

$$V_{k_1k_2;k_1'k_2'} = \frac{e_1e_2}{\epsilon_0\Omega(\mathbf{k_1} - \mathbf{k_{1'}})^2}\delta(\mathbf{k_1} - \mathbf{k_{1'}} + \mathbf{k_2} - \mathbf{k_{2'}})\delta_{\sigma_1\sigma_1'}\delta_{\sigma_2\sigma_2'}. \tag{A.16}$$

The coulomb interaction collective dynamical screening behavior in the plasmas and later Debye was invented a screened potential called Debye potential .

The incoming wave number k_i and outgoing wave number k_i' and their spin σ_i, σ_i' . We consider a local density $(r_1 = r_1', r_2 = r_2')$ with a relative distance $|\mathbf{r_2} - \mathbf{r_1}|$. The spin,

species and momentum $q = k_1 - k_1'$ are conserving interaction. The interaction propagator $V(1, 2; 1'2')$, with the vertices $\Gamma(11')$ and $\Gamma(22')$. $\Gamma(11') = \sum_q e_1 \delta_{\sigma_1 \sigma_{1'}} \delta_{c_1 c_{1'}} \delta_{p_1 + q, p_1'}$, and $\Gamma(22') = \sum_q e_2 \delta_{\sigma_2 \sigma_{2'}} \delta_{c_2 c_{2'}} \delta_{p_2 + q, p_2'}$.

$$V(12, 1'2') = \sum_q \Gamma(11') V(q) \Gamma(22') = e_{11'} \frac{1}{\Omega \varepsilon_0 q^2} e_{22'}. \tag{A.17}$$

The Eq. (A.17) is the Coulomb interaction in a plasma description of strongly coupled plasmas.

A.4. Debye Potential

In this subsection, we will consider the Debye potential in the plasma screening environment. A test particle charge e has a velocity v_0 induced to the charge density $\rho_0(\mathbf{r}, t) = e\delta(\mathbf{r} - \mathbf{v_0}t)$ This test particle with charge e will polarize into plasma and induced a charge density $\rho^{\mathrm{ind}}(\mathbf{r}, t) = \sum_c \rho_c^{\mathrm{ind}}(\mathbf{r}, t)$ [18]. These induced charge could be charges, free electrons and bound electrons describing in index c. The Poisson equation was combined the test particle part and induced part,

$$\nabla^2 \phi^{\mathrm{eff}}(\mathbf{r}, t) = -4\pi \left\{ e\delta(\mathbf{r} - \mathbf{v_0}t) + \sum_c \rho_c^{\mathrm{ind}}(\mathbf{r}, t) \right\}. \tag{A.18}$$

the effective screening potential could be writte

$$\phi^{\mathrm{eff}(\mathbf{k}, \omega)} = \frac{\phi^{\mathrm{test}}(\mathbf{k}, \omega)}{\epsilon(\mathbf{k}, \omega)}. \tag{A.19}$$

In Eq. (A.4), ϵ is the dielectric function in the plasma.

The Debye potential at spatial space is given by

$$V(\mathbf{r_1 r_2}, \mathbf{r_{1'} r_{2'}}) = \frac{e_1 e_2}{4\pi \epsilon_0 |\mathbf{r_1} - \mathbf{r_2}|} e^{-\kappa |\mathbf{r_1} - \mathbf{r_2}|} \delta(\mathbf{r_1} - \mathbf{r_{1'}}) \delta(\mathbf{r_2} - \mathbf{r_{2'}}) \tag{A.20}$$

$\kappa = \frac{1}{r_D}$ is Debye screening length.

At a non-degenerate plasma the mean kinetic energy is proportional to $k_B T$. At very high temperature has no bound electrons and the plasma becomes ideal plasma

A.5. 3-21G* Binding energy and K_α Emission energy for different charge states of Si (in eV)

(eV)	Si^{14}	Si^{13}	Si^{12}	Si^{11}	Si^{10}	Si^9
	-7820.34	-7812.57	-7796.75	-7765.06	-7720.66	-7554.43
Si^8	Si^7	Si^6	Si^5	Si^4	Si^3	Si^2
-7347.36	-7098.09	-6792.04	-6442.39	-6048.83	-5582.95	-5069.67

Table A.5.: Binding energy for different charge states of Si (in eV).

Initial Conf.	$1s^12s^22p^63s^23p^2$	$1s^12s^22p^53s^23p^2$	
Final Conf.	$1s^22s^22p^53s^23p^2$	$1s^22s^22p^43s^23p^2$	
Energy $K_{\alpha 1}$	1739.6	1751.2	
Energy $K_{\alpha 2}$	1739.0	1750.7	
Initial Conf.	$1s^12s^22p^43s^23p^2$	$1s^12s^22p^33s^23p^2$	$1s^12s^22p^23s^23p^2$
Final Conf.	$1s^22s^22p^33s^23p^2$	$1s^22s^22p^23s^23p^2$	$1s^22s^22p^13s^23p^2$
Energy $K_{\alpha 1}$	1763.2	1778.4	1788.8
Energy $K_{\alpha 2}$	1762.7	1777.8	1788.2

Table A.6.: Emission energies for different configuration of emitter with occupied electrons M shell M0 (in eV).

Initial Conf.	$1s^12s^22p^6$	$1s^12s^22p^5$	$1s^12s^22p^4$	$1s^12s^22p^3$	$1s^12s^22p^2$
Final Conf.	$1s^22s^22p^5$	$1s^22s^22p^4$	$1s^22s^22p^3$	$1s^22s^22p^2$	$1s^22s^22p^1$
Energy $K_{\alpha 1}$	1742.9	1761.3	1775.2	1791.8	1812.4
Energy $K_{\alpha 2}$	1742.3	1760.7	1774.6	1791.2	1811.8

Table A.7.: Emission energies for different configuration of emitter with empty M shell M4 (in eV).

A.6. Landau Damping

Using the Dirac identity $\frac{1}{\omega \pm i\epsilon} = \mp i\pi\delta(\omega) + \frac{P}{\omega}$ in the $\{\epsilon^{RPA}(q, \hbar(\omega + i0))\}$. The discontinuity due to a pole at $\hbar\omega = \epsilon_{c,p} - \epsilon_{c,p-q}$. To get imaginary part $\text{Im}\{\epsilon^{RPA}(q, \hbar(\omega + i0))\}$,

$$\text{Im}\{\epsilon^{RPA}(q, \hbar(\omega + i0))\}. \tag{A.21}$$

$$= \sum_c \pi \frac{e_c^2}{\epsilon_0 q^2} (2s_c + 1) \int \frac{d^3p}{(2\pi)^3} \left[f(\epsilon_{c,p-q}) - f(\epsilon_{c,p}) \right] \cdot \delta(\hbar\omega + \epsilon_{c,p-q} - \epsilon_{c,p}). \tag{A.22}$$

$$= \sum_c \pi \frac{e_c^2}{\epsilon_0 q^2} (2) \cdot \left[\int \frac{d^3p}{(2\pi)^3} f(\epsilon_{c,p-q}) \delta(\hbar\omega + \epsilon_{c,p-q} - \epsilon_{c,p}) - \int \frac{d^3p}{(2\pi)^3} f(\epsilon_{c,p}) \delta(\hbar\omega + \epsilon_{c,p-q} - \epsilon_{c,p}) \right]. \tag{A.23}$$

Setusing $p' = p - q$ and rename $p = p'$

$$= \sum_c \pi \frac{e_c^2}{\epsilon_0 q^2} (2) \cdot \int \frac{d^3p}{(2\pi)^3} f(\epsilon_{c,p}) \left[\delta(\hbar\omega + \epsilon_{c,p} - \epsilon_{c,p+q}) - \delta(\hbar\omega + \epsilon_{c,p-q} - \epsilon_{c,p}) \right]. \tag{A.24}$$

Using $\delta(ax) = \frac{1}{|a|}\delta(x)$, $\epsilon_{c,p} = \frac{\hbar^2 p^2}{2m_c}$, $\epsilon_{c,p\pm q} = \frac{\hbar^2 (\mathbf{p}\pm\mathbf{q})^2}{2m_c}$ to resolve the δ term.

$$\delta(\hbar\omega + \epsilon_{c,p-q} - \epsilon_{c,p}) = \delta\left(\hbar\omega + \frac{\hbar^2 (p^2 - 2pq\cos\theta + q^2)}{2m_c} - \frac{\hbar^2 p^2}{2m_c} \right) \tag{A.25}$$

$$= \delta\left(\frac{m_c \hbar\omega}{m_c} - \frac{\hbar^2 pq\cos\theta}{m_c} + \frac{\hbar^2 q^2}{2m_c} \right) \tag{A.26}$$

$$= \frac{m}{\hbar^2} \delta\left(\frac{m_c \omega}{\hbar} - pq\cos\theta + \frac{q^2}{2} \right) \tag{A.27}$$

$$= \frac{m}{\hbar^2 pq} \delta\left(-\cos\theta + \frac{m_c \omega}{\hbar pq} + \frac{q}{2p} \right). \tag{A.28}$$

We defined $\delta(\hbar\omega + \epsilon_{c,p-q} - \epsilon_{c,p}) = \frac{m_c}{\hbar^2 pq} \delta\left(\cos\theta - \frac{m_c \omega}{\hbar pq} - \frac{q}{2p} \right) \equiv \frac{m_c}{\hbar^2 pq} \delta_1$ and $\delta(\hbar\omega + \epsilon_{c,p} - \epsilon_{c,p+q}) = \frac{m_c}{\hbar^2 pq} \delta\left(\cos\theta - \frac{m_c \omega}{\hbar pq} + \frac{q}{2p} \right) \equiv \frac{m_c}{\hbar^2 pq} \delta_2$. The form $\text{Im}\{\epsilon^{RPA}(q, \hbar(\omega + i0))\}$ reduced to

$$= \sum_c \pi \frac{e_c^2}{\epsilon_0 q^2} 2\pi \frac{(2s_c + 1)}{(2\pi)^3} \int_0^\infty dp \int_{-1}^1 d\cos\theta p^2 f(\epsilon_c, p) \frac{m_c}{\hbar^2 pq} [\delta_2 - \delta_1]. \tag{A.29}$$

Because $\cos\theta \in [-1; 1]$ and the two δ functions only contribute if $\left| \frac{m_c \omega}{\hbar pq} \pm \frac{q}{2p} \right| \leq 1 \Rightarrow \left| \frac{m_c \omega}{\hbar q} \pm \right.$

A. Appendix

$\frac{q}{2}| \leq p$. They just change the limits in the two integrations [6]: $\mathtt{Im}\{\epsilon^{RPA}(q, \hbar(\omega + i0))\}$

$$= \sum_c 2\pi^2 \frac{e_c^2 m_c}{\epsilon_0 \hbar^2 q^3} \frac{(2s_c + 1)}{(2\pi)^3} \left[\int_{|\frac{m_c\omega}{\hbar q} - \frac{q}{2}|}^{\infty} dp\, p f(\epsilon_{c,p}) - \int_{|\frac{m_c\omega}{\hbar q} + \frac{q}{2}|}^{\infty} dp\, p f(\epsilon_{c,p}) \right] \quad (A.30)$$

$$= \sum_c (2\pi)^2 \frac{e_c^2 m_c}{\epsilon_0 \hbar^2 q^3} \int_{|\frac{m_c\omega}{\hbar q} - \frac{q}{2}|}^{|\frac{m_c\omega}{\hbar q} + \frac{q}{2}|} dp \frac{p}{1 + e^{\beta\left(\frac{\hbar^2 p^2}{2m_c} - \mu_c\right)}} \quad (A.31)$$

$$= \sum_c \frac{e_c^2 m_c^2}{4\pi\epsilon_0 \beta \hbar^4 q^3} (2s_c + 1) \ln \left| \frac{1 + e^{-\beta\left(\frac{\hbar^2}{2m_c}\left(\frac{m_c\omega}{\hbar q} - \frac{q}{2}\right)^2 - \mu_c\right)}}{1 + e^{-\beta\left(\frac{\hbar^2}{2m_c}\left(\frac{m_c\omega}{\hbar q} + \frac{q}{2}\right)^2 - \mu_c\right)}} \right|. \quad (A.32)$$

bf 1 , α_1	11pg;d_{1s}	bf 2, α_2	11 pg;d_{2s}
0.2549000000D+06	0.6259454587D-04	0.2549000000D+06	0.4011785433D-06
0.3819000000D+05	0.4862070436D-03	0.3819000000D+05	0.3058719263D-05
0.8690000000D+04	0.2548609738D-02	0.8690000000D+04	0.1502997647D-04
0.2462000000D+04	0.1060105144D-01	0.2462000000D+04	0.4502390871D-04
0.8048000000D+03	0.3692994503D-01	0.2913000000D+03	-0.1266002594D-02
0.2913000000D+03	0.1076356905D+00	0.1136000000D+03	-0.1006734813D-01
0.1136000000D+03	0.2483387413D+00	0.4675000000D+02	-0.4737784997D-01
0.4675000000D+02	0.3917442532D+00	0.1982000000D+02	-0.9744253676D-01
0.1982000000D+02	0.3030081137D+00	0.7708000000D+01	0.9449527074D-01
0.7708000000D+01	0.5545673652D-01	0.3340000000D+01	0.5426692785D+00
0.3340000000D+01	-0.7135272198D-02	0.1402000000D+01	0.4752526204D+00
bf 3 ,α_3	11 pg; d_{3s}	bf 4, α_4	1 pg;d_{4s}
0.2549000000D+06	-0.9639289733D-08	0.4387000000D+00	0.1000000000D+01
0.3819000000D+05	-0.6815112801D-07	bf 5, α_5	1 gp;d_{5s}
0.8690000000D+04	-0.5430989250D-07	0.7944000000D-01	0.1000000000D+01
0.2462000000D+04	-0.2225080935D-05	bf 6-8, α_6	6 gp; d_{6p}
0.2913000000D+03	-0.3675111577D-04	0.4815000000D+03	0.2085549471D-02
0.1136000000D+03	0.1916046946D-04	0.1139000000D+03	0.1667619837D-01
0.1982000000D+02	0.2219009176D-02	0.3623000000D+02	0.7753893526D-01
0.7708000000D+01	-0.3738426098D-02	0.1334000000D+02	0.2313987378D+00
0.3340000000D+01	-0.6219870833D-01	0.5252000000D+01	0.4239367733D+00
0.1402000000D+01	-0.3088697837D+00	0.2120000000D+01	0.4277947460D+00
0.2070000000D+00	0.1139437590D+01		
bf 9-11α_7	6 pg;d_{7p}	bf 12-14, α_8	1 pg; d_{8p}
0.4815000000D+03	0.1088933479D-04	0.8561000000D+00	0.1000000000D+01
0.1139000000D+03	-0.1312701062D-03	bf 15-17, α_9	1 gp; d_{9p}
0.1334000000D+02	-0.6072647947D-02	0.7889000000D-01	0.1000000000D+01
0.5252000000D+01	-0.3540085610D-02	bf 18-22, α_{10}	1 gp; d_{10d}
0.2120000000D+01	-0.5109971270D-01	0.1590000000D+00	0.1000000000D+01
0.2528000000D+00	0.1014431383D+01		
bf 23-27, α_{11}	1 pg; d_{11d}	bf 28-34, α_{12}	1 pg; d_{12f}
0.4810000000D+00	0.1000000000D+01	0.3360000000D+00	0.1000000000D+01
bf 35, α_{13}	1 pg;d_{13s}	bf 36-38,α_{14}	1 pg;d_{14p}
0.3300000000D-01	0.1000000000D+01	0.2370000000D-01	0.1000000000D+01
bf 39-43, α_{15}	1 pg; d_{15d}	bf44-50, α_{16}	1 pg; d_{16f}
0.5560000000D-01	0.1000000000D+01	0.1250000000D+00	0.1000000000D+01

Table A.8.: Aug-cc-pVTZ (5D, 7F) standard basis function for Si.

Bibliography

[1] A. Haase, *et al*, *Röntgen Centennial X-rays in Natural and Life Sciences*, (World Scientific Publishing Co. Pte. Ltd.) (1997).

[2] The Nobel Prize in Physics 1915, http://www.nobelprize.org/nobel_prizes/physics/laureates/1915/

[3] David Salzmann, *Atomic Physics in Hot Plasmas*, (Oxford University Press) (1998).

[4] J. Wesson, *et. al*, *Tokamaks 4 Edition*, (Oxford University Press) (2011).

[5] Eoropean Fusion Development Agreement (EFDA) , http://www.efda.org/fusion/

[6] Gerd, Röpke and Mathias Winkel, *Quantum Theory and Many-Particle Systems*, (Rostock University) (2009).

[7] A. Sengebusch, *et. al*, J. Phys. A **42**, 214061 (2009).

[8] U. Zastrau, *et. al*, Phys. Rev. E **81**, 026406 (2010).

[9] P. Neumayer, *et. al*, *Evidence for ultra-fast heating in intense-laser irradiated reduced-mass targets*,Phys. of Plasmas **19**, 122708 (2012).

[10] U. Zastrau, *et. al*, *High-resolution radial Ka spectra obtained from a multi-keV electron distribution in solid-density titanium foils generated by relativistic laser-matter interaction*, High Energy Density Pysics **7**, Issue 2, 47-53 (2011).

[11] D. Castella, *et. al*, *L-shell ionization in near-central collisions of heavy ions with low-Z atoms*, Phys. Rev. A **61**, 052711 (2000).

[12] G. Graeffe, *et. al*, *Si Ka x-ray emission spectra of Si, SiC, SiO2, and Si3N4*, J. Phys. B: Atom.Molec. Phys., **10**, 16 (1977).

[13] Zhenlin Liu, *et. al*, *Correlation between chemical shift of Si Ka lines and the effective charge on the Si atom and its application in the Fe-Si binary system*, Phys. Rev. B **69**, 035106 (2004).

[14] O. N. Rosmej, *et. al*, *Charge state and stopping dynamics of fast heavy ions in dense matter*, Phys. Rev. A **72**, 052901 (2005).

Bibliography

[15] J. Rzadkiewicz, *et. al*, *Studies of the Ka X-ray spectra of low-density SiO2 aerogel induced by Ca projectiles for different penetration depths*, High Energy Density Physics **3**, 233-236 (2007).

[16] J. Rzadkiewicz, *et. al*, *Interpretation of the Si Ka x-ray spectra accompanying the stopping of swift Ca ions in low density SiO2 aerogel*, Phys. Rev. A **82**, 012703 (2010).

[17] Ichirou Fukumoto, *et al*, High-Power Particle Beams, 2000 13th International Conference on , 1028-1031 (2000).

[18] D. Kremp, Kräft, *et al*, *Quantum Statistics of Nonideal Plasmas*, (Springer, Berlin) (2005).

[19] M. P. Bachynski, *et. al*, Antenna Noise Temperature in Plasma Environment , 1846-1867 (1961).

[20] http://www.nist.gov/physlab/data/xraytrans/index.cfm.

[21] Peter Atkins, *et al*, *Quantenmechanik*, (Springer, Berlin) (1998).

[22] Franz Schwabl, *Molecular Quantum Mechanics 4 Edition*, (Oxford University Press Inc., New York) (2005).

[23] J. J. Sakurai, *et al*, *Modern Quantum Mechanics Revised Edition*, (Addison-Wesley Publishing Company, Inc.) (1994).

[24] R. Shankar, *et al*, *Principles of Quantum Mechanics 2 Edition*, (Plenum Press, New York) (1994).

[25] http://nlte.nist.gov/FLY/.

[26] F. Schwabel, *Statistical Mechanics*, (Springer, Berlin) (2002).

[27] A. Sengebusch, *Linienprofile von Röntgenübergänge komplexer Atome in dichten Plasmen*, (PhD Thesis Rostock), [urn:nbn:de:gbv:28-diss2011-0018-2] (2010).

[28] C. F. Bunge, *et. al*, Atomic Data and Nuclear Data Tables **53**, 113-162 (1993).

[29] Carlos F. Bunge, *et. al*, *Hartree-Fock and Roothaan-Hartree-Fock energies for the ground states of He through Xe*, Phys. Rev. A **46**, 7 (1992).

[30] C. C. J. Roothaan, *et. al*, *New developments in molecular orbital theory*, Reviews of modern physics **23**, 2 (1951).

[31] H.B. Schlegel, *et. al*, *Transformation Between Cartesian and Pure Spherical Harmonic Gaussians*, International Journal of Quantum Chemistry, **54**, 83-87 (1994).

[32] W. J. Pietro, *et. al*, *Self-Consistent Molecular Orbital Methods. 24. Supplemented Small Split-Valence Basis Sets for Second-Row Elements*, J. Am. Chem . Soc., **104**, 19 (1982).

[33] Basis Sets,
http://www.gaussian.com/g_tech/g_ur/m_basis_sets.htm

[34] David E. Woon, *et. al*, *Gaussian basis sets for use in correlated molecular calculations. III. The atoms aluminum through argon*, J. Chem. Phys. **98**, 1358 (1993).

[35] P. Palmeri, P. Quinet,*et al.*, Astrophys. J. Suppl., **177**, 408-416 (2008).

[36] R. D. Cowan, *The Theory Of Atomic Structure And Spectra*, (University of California Press) (1981).

[37] http://aphysics2.lanl.gov/cgi-bin/ION/runlanl08e.pl.

[38] David C. Brydges, Commun. math. Phys. **58**, 313-350 (1978).

[39] S. Günter, *Optische Eigenschaften dichter Plasmen*, (Habilitationsschrift Rostock), (1995).

[40] A. Sengebusch, *et. al*, Contrib. Plasma Phys. **49**, No.10, 748-754 (2009).

[41] http://nlte.nist.gov/FLY/Doc/Manual_FLYCHK_Nov08.pdf

[42] https://www-amdis.iaea.org/FLYCHK/ZBAR/csd018.php

[43] I. H. Hutchinson, *Principles of plasma diagnostics*, (Cambridge University Press) (1987).

[44] Robert D. Cowan, *The theory of atomic structure and spectra*, (Cambridge University Press) (1981).

[45] W. Demtröder *Experimentalphysik 3*, (Atome,Moleküle und Festkörper), ISBN 3-540-66790-3 2. Auflage (Springer) (2000).

[46] K.Nishikawa and M. Wakatani, *atoms and plasmas*, (Springer-Verlag Press) (1994).

[47] R. D. Cowan, *The theory of atomic structure and spectra*, (University of California Press) (1981).

[48] N. Konjevic, *et. al*, J. Phys. Chem. Ref. Data **31**, 819 (2002).

[49] A. Sreckovic, *et. al*, Physics Scripta **57**, 225-227 (1998).

[50] J. Puric, *et. al*, Z. Physik **267**, 71-75 (1974).

[51] Yves Vitel and Maurice Skowronek, J. Phys. B: At. Mol. Phys. **20**, 6477-6491 (1987).

Bibliography

[52] P. Palmeri, P. Quinet *et al.*, The Astrophys Journal Supplement Series, **177**, 408-416 (2008).

[53] Priscilla E. Greenwood and Mikhail S. Nikulin, *A Guide to Chi-Squared Testing*, (John Wiley & Sons, Inc.) (1996).

Selbständigkeitserklärung:

Ich erkläre,
dass die eingereichte Dissertationsschrift selbständig und ohne fremde Hilfe verfasst,
andere als die von mir angegebenen Quellen und Hilfsmittel nicht benutzt.

Oulu, 14 January 2015, Yi-Ling Chen